U.PORTO

FEUP FACULDADE DE ENGENHARIA
UNIVERSIDADE DO PORTO

U.PORTO

INSTITUTO DE CIÊNCIAS
BIOMÉDICAS ABEL SALAZAR
UNIVERSIDADE DO PORTO

Myelination in a dish
A novel tissue engineered platform to study oligodendrocyte differentiation and myelination

Master Dissertation

Integrated Master in Bioengineering

Specialization in Molecular Biotechnology

Author:
Helena Isabel Soares de Paiva Ferreira

Supervisor:
Prof. Ana Paula Pêgo

Co-Supervisor:
Eva Maia Carvalho

Porto, September 2019









Myelination in a dish
A novel tissue engineered platform to study oligodendrocyte differentiation and myelination

Helena Isabel Soares de Paiva Ferreira

Dissertation submitted to Faculdade de Engenharia da Universidade do Porto and to Instituto de Ciências Biomédicas Abel Salazar to obtain the degree of
Masters in Bioengineering

Final version

Porto, September 2019

Institutional Acknowledgments

The work presented in this dissertation was financially supported by:

- Project NORTE-01-0145-FEDER-000008 and NORTE-01-0145-FEDER-000012, supported by Norte Portugal Regional Operational Programme (NORTE 2020), under the PORTUGAL 2020 Partnership Agreement, through the European Regional Development Fund (ERDF) and FEDER - Fundo Europeu de Desenvolvimento Regional funds through the COMPETE 2020 - Operacional Programme for Competitiveness and Internationalisation (POCI), Portugal 2020;
- Portuguese funds through FCT/MCTES in the framework of the project "Institute for Research and Innovation in Health Sciences" (POCI-01-0145-FEDER-007274);
- National Funds through FCT – Fundação para a Ciência e a Tecnologia (UTAP-EXPL/NTec/0057/2017).

"*Nothing in life is to be feared, it is only to be understood. Now is the time to understand more, so that we may fear less.*"

Marie Curie

Acknowledgements

O Mestrado Integrado em Bioengenharia proporcionou-me cinco anos de crescimento pessoal e profissional. A gratificação que hoje sinto deve-se muito às pessoas com quem tive a oportunidade de interagir e aprender - e a quem aqui deixo um enorme obrigada.

Em primeiro lugar, à professora Ana Paula, pela oportunidade concedida para desenvolver o meu trabalho de tese no nBTT e pelo o acompanhamento prestado. Foi um privilégio aprender e trabalhar consigo. Obrigada por motivar os alunos de Bioengenharia (em particular do ramo de Biotecnologia Molecular) e mostrar que há lugar para nós tanto na academia como na indústria - quando por vezes não nos apercebemos de tal.

À Eva Carvalho, por ter sido a minha guia nos últimos meses e me dar a conhecer o mundo da glia – os oligodendrócitos são, de facto, células muito bonitas. Por todos os conselhos, críticas, paciência e motivação, fico-te imensamente grata. Sei que não poderia ter tido coorientadora mais dedicada. Participar no projeto Mechano foi uma excelente experiência para a minha formação profissional e uma porta para um campo científico que surpreendentemente me interessou muito. Obrigada ainda ao Miguel Morais pela ajuda prestada no trabalho laboratorial.

A todos os membros do nBTT, pelo generoso acolhimento e ajuda sempre que necessária. Um obrigada em particular à Sofia Santos pela disponibilidade para ser minha tutora no curso de “Laboratory Animal Science”.

Ao André Maia, do serviço BioSciences Screening, pela ajuda no desenvolvimento dos protocolos de análise de imagem utilizados nesta dissertação e disponibilidade para esclarecimento de dúvidas. Agradeço ainda à Dalida Pedro, pela assistência no critical point drying e culturas celulares, e à María Lázaro, do serviço Bioimaging, pela ajuda com o microscópio confocal.

À professora Inês Gonçalves, do grupo BioEngineered Surfaces, pela ajuda dada com a formulação de PDMS e as propriedades mecânicas.

Não conseguiria terminar o mestrado sem o precioso apoio de familiares e amigos ao longo destes anos, pelo que também a eles dirijo os meus mais profundos agradecimentos.

À Mariana Dias, Cristiana e Marina, as minhas biomédicas e companheiras, um especial obrigada pela paciência, gargalhadas e momentos memoráveis. Ao Paulo Maia, Patrícia, Margarida, Carolina, Mariana Coelho, Anabela e Daniela, pelo apoio e animação que me trouxeram. Foram cinco anos de partilha de vivências intensas que me marcaram profundamente e me enchem o coração – e venham muitos mais! A todos os colegas de Biotecnologia que, como eu, realizaram tese no i3S, agradeço pela companhia nas pausas e toda a ajuda.

Ao Nuno, pelo apoio incondicional, infindável paciência e imenso carinho. Muito obrigada por não me deixares ir abaixo e me acompanhares nesta jornada.

Aos meus pais, Célia e Vicente, a quem tudo devo. Serei sempre grata pelos sacrifícios que fazem pela nossa família e lições que me transmitem. Obrigada pelo exemplo exímio de determinação, humildade e esperança. Tudo o que sou e conquisto faz parte de vós e é vossa conquista também.

Abstract

Myelination enables saltatory conduction of action potentials along axons. In the central nervous system, this process is initiated by oligodendrocyte precursor cells (OPCs), which differentiate into oligodendrocytes (OLs). Destruction of myelin internodes, OL apoptosis and consequent axonal degeneration are hallmarks of primary demyelinating diseases, such as multiple sclerosis – for which there are currently no effective therapies.

OPCs and OLs are proven mechanosensitive cells, so physical and mechanical cues play a role in OL biology and, presumably, in the (de)myelination process. However, the lack of platforms with biologically relevant features has hampered the study of these mechanobiology processes – which may be important for the development of efficient therapies against demyelinating diseases. Our working hypothesis is that physical and mechanical cues similar to those provided *in vivo* lead to an OLs' response that is closer to the biological situation.

Here, a new system to study the influence of substrate stiffness and stimulus of axon surrogates on OPCs/OLs is proposed. Briefly, this platform consists of an array of poly(dimethylsiloxane) (PDMS) micropillars with low substrate stiffness, biologically relevant diameters (1-5 μm) to act as axon surrogates, as well as being technically amenable for adaptation into a high-throughput system. This micropillars-based platform can be used to observe oligodendroglial cells' response to physical and mechanical stimuli in an environment that more closely mimics the *in vivo* milieu, in comparison to previously published models.

In this work, it was possible to produce micropillars with a new formulation of PDMS (prepolymer mixed with Dow Corning Medical Fluid), corresponding to a significant advance in the fabrication of structures with a great aspect ratio and reduced stiffness. It was also shown that OPCs not only adhere and differentiate, but also extend processes that wrap around micropillars, forming myelin-like sheaths. Furthermore, image analysis protocols using open-source software were developed for automated analysis of widefield fluorescence images, in the context of high-content screening. The obtained results suggest that softer PDMS substrates promote OPC morphological differentiation, and that thicker micropillars (4 and 5 μm) appear to promote more extensive differentiation and wrapping in comparison to thinner micropillars.

In conclusion, we present evidence that supports that mechanical signals should be considered in the design of new therapies to treat demyelinating conditions. Consequently, the proposed *in vitro* model design and automated output analysis explored in this work constitute a technical advance in the development of high-throughput platforms for screening of therapeutic targets and strategies against multiple sclerosis.

Keywords: myelin, oligodendrocyte, oligodendrocyte precursor cell, axon surrogates, mechanobiology, physical/mechanical cues, poly(dimethylsiloxane), high-throughput platform

Sumário

A mielinização é um processo que permite a condução saltatória de potenciais de ação ao longo de axónios. No sistema nervoso central, este processo é iniciado por células percursoras de oligodendrócitos (OPCs), as quais se diferenciam em oligodendrócitos (OLs). A destruição dos internódulos de mielina, apoptose de OLs e consequente degeneração axonal são as principais características de doenças desmielinizantes primárias, como a esclerose múltipla – para as quais atualmente não existem terapias eficazes.

OPCs e OLs são células mecanosensitivas, pelo que fatores físicos e mecânicos exercem efeito na biologia dos OLs e, presumivelmente, nos processos de (des)mielinização. Todavia, a falta de plataformas com características relevantes em termos biológicos dificulta o estudo destes processos mecanobiológicos - o que poderá ser importante para o desenvolvimento de terapias eficazes para as doenças desmielinizantes. A hipótese aqui proposta é que estímulos físicos e mecânicos semelhantes aos existentes *in vivo* suscitam uma resposta nos OLs que é também mais próxima do que se verifica no cenário biológico.

Neste trabalho, propõe-se um novo sistema para o estudo quer da influência da rigidez do substrato, quer do estímulo da presença do axónio. A plataforma proposta consiste num *array* de micropilares de poli(dimetilsiloxano) (PDMS) com uma baixa rigidez, diâmetros biologicamente relevantes (1-5 μm) para mimetizar axónios, sendo tecnicamente vantajosa para a adaptação a um sistema *high-throughput*. Esta plataforma micropilares pode ser usada para observar a resposta de células oligodendrogliais a estímulos físicos e mecânicos, num meio que mimetiza mais fielmente o meio *in vivo*, em comparação com modelos publicados anteriormente.

Neste trabalho, foi possível produzir micropilares com uma nova formulação de PDMS (pré-polímero misturado com *Dow Corning Medical Fluid*), correspondendo a um avanço significativo na fabricação de estruturas com um elevado fator de forma e uma rigidez reduzida. Demonstrou-se ainda que as OPCs não só aderem e diferenciam, como também projetam processos que envolvem os micropilares, formando bainhas de mielina. Adicionalmente, foram desenvolvidos protocolos de análise de imagem com software de acesso livre para a análise automática de imagens de microscopia fluorescência, no contexto de *high-content screening*. Os resultados obtidos sugerem que os substratos de PDMS de menor rigidez promovem a diferenciação morfológica de OPCs. Por outro lado, pilares de maiores diâmetros (4 e 5 μm) parecem promover a diferenciação e o envolvimento de micropilares em comparação com menores diâmetros.

Em suma, apresentam-se aqui evidências de que os estímulos mecânicos devem ser equacionados no *design* de novas terapias para doenças desmielinizantes. Consequentemente, o *design* proposto deste modelo *in vitro* e a análise automática de dados neste trabalho constituem um avanço técnico no desenvolvimento de plataformas *high-throughput* para triagem de novos alvos terapêuticos e estratégias para a esclerose múltipla.

Palavras-chave: mielina, oligodendrócito, célula progenitora de oligodendrócito, mímicos de axónios, mecanobiologia, fatores físicos/mecânicos, poil(dimetilsiloxano), plataforma *high-throughput*

Contents

Acknowledgements **v**

Abstract **vii**

Chapter 1 Introduction **1**
1.1 Myelination and demyelination in the central nervous system 4
1.1.1 Development of the oligodendroglial cell lineage and cellular mechanisms of myelination 4
1.1.2 Demyelination in multiple sclerosis and remyelination mechanisms 7
1.2 Mechanobiology in (de)myelination 11
1.2.1 Alterations in brain's mechanical properites in (de)myelination . 11
1.2.2 Mechanotransduction and cytoskeletal behaviour of oligodendroglial cells 12
1.3 Models to study the influence of mechanical forces in (de)myelination 14
1.3.1 *In vitro* models of the influence of substrate/matrix stiffness . . 15
1.3.2 *In vitro* models of the influence of axoglial contact 15
1.4 Development of a high-throughput micropillars-based platform for *in vitro* recapitulation of oligodendrocyte differentiation and myelination . 20

Chapter 2 Motivation and Objectives **25**

Chapter 3 Materials and Methods **27**
3.1 Fabrication of micropillars' platforms 27
3.1.1 Fabrication of PDMS micropillars' platforms 27
3.1.2 Critical point drying 27
3.1.3 Plasma treatment and coating of PDMS micropillars 28
3.2 Characterization of PDMS platforms 29
3.2.1 Rheology 29
3.2.2 Scanning electron microscopy 29
3.3 Animals 30
3.4 Cell culture 30
3.4.1 Brain dissections and collection of cortices 30
3.4.2 Mixed glial cultures 31
3.4.3 OPCs isolation and differentiation 32
3.5 Immunocytochemistry 35
3.6 Reverse transcriptase quantitative PCR 36
3.7 Inverted fluorescence microscopy and confocal microscopy 38
3.8 Image segmentation and analysis 38
3.9 Live imaging of OPC cultures 38
3.10 Statistical analysis 39

Chapter 4 Results **41**
4.1 Exploration of PDMS formulations for the production of micropillars and evaluation of mechanical properties 41

4.1.1 PDMS micropillars have the projected shape and dimensions, but are stiffer than brain parenchyma and axons 41
4.1.2 Addition of dimethicone reduces PDMS stiffness by up to 70% 45
4.1.3 Micropillars produced with 2:1 PDMS-to-dimethicone ratio have similar shape and dimensions than those of control PDMS . . 47
4.2 Optimization of cell seeding density on PDMS platforms 50
4.3 Evaluation of purity of OPC cultures 52
4.3.1 GFAP-, IBA1- and βIII tubulin-positive cells are present in OPC cultures, decreasing OPC purity 53
4.4 Effect of micropillar diameter and substrate stiffness on OPC differentiation and myelination 57
4.4.1 OPCs cultured on softer substrates and flat surfaces seems to differentiate more up to differentiation day 1 64
4.4.2 Lower substrate stiffness and micropillars with larger diameters seem to promote OPC differentiation and myelination . . . 67
4.5 Live imaging of OPC differentiation and micropillars' wrapping 72

Chapter 5 Discussion **75**

Chapter 6 Conclusions and Future Perspectives **81**

Bibliography **83**

Appendix A Introductory Course in Laboratory Animal Science **93**

Appendix B RT-qPCR - Supplementary Information **97**

Appendix C Evaluation of the purity of OPC cultures – Image analysis process **101**
C.1 Identification and quantification of GFAP$^+$ cells using CellProfiler and CellProfiler Analyst 101
C.2 Identification and quantification of IBA-1$^+$ and βIII tubulin$^+$ cells using CellProfiler and CellProfiler Analyst 104

Appendix D Evaluation of OL differentiation stage – Image analysis process **107**
D.1 Image segmentation using ilastik 107
D.2 Image analysis using CellProfiler 108
D.3 Analysis of results using Microsoft Excel 111

Appendix E Evaluation of micropillars' wrapping – Image analysis process **115**
E.1 Image segmentation using ilastik 115
E.2 Image analysis using CellProfiler 115
E.3 Analysis of results using Microsoft Excel 121

Appendix F Evaluation of the purity of OPC cultures – Quantitative data **123**

Appendix G Effect of physical cues on OPC differentiation and myelination - Comparison between timepoints **125**

List of Figures

1.1 Saltatory conduction of action potential in a myelinated and demyelinated axon . . . 1
1.2 Global prevalence of MS in 2013. . . . 3
1.3 Oligodendroglial cell lineage . . . 4
1.4 Myelination in the CNS . . . 6
1.5 Structure of a myelin internode . . . 6
1.6 Remyelination and hypotheses for failure of the process . . . 9
1.7 Actin assembly and disassembly during myelin wrapping . . . 13
1.8 Schematic representation of micropillars and microfibers . . . 17
1.9 Young's modulus of materials used for oligodendrocyte culture and reference values of stiffness for brain parenchyma and axon . . . 18
1.10 Culture of OPCs in microfibers or micropillars with various properties . 20
1.11 Design of PDMS micropillars' platform . . . 21
1.12 Schematic representation of quadrants in micropillars' platforms . . . 22

3.1 PDMS fabrication process . . . 27
3.2 PDMS surface modifications with plasma treatment . . . 28
3.3 Experimental procedure of MGCs. . . . 32
3.4 Experimental procedure of OPC cultures . . . 34
3.5 Timeline for MGCs and OPC cultures . . . 34

4.1 Representative SEM images of PDMS micropillars . . . 42
4.2 Representative graph of an amplitude sweep test and Determination of LVR . . . 44
4.3 Representative graph of a frequency sweep test . . . 45
4.4 Comparison of E from control PDMS, 3:1 and 2:1 PDMS-to-dimethicone ratio formulations . . . 46
4.5 Representative SEM images of soft PDMS micropillars . . . 48
4.6 Representative images of OPC morphology for seeding densities of 556, 1250 and 1667 cells/mm^2, at diff. days 2 and 5 . . . 51
4.7 Representative images of OPC morphology for seeding density of 556 cells/mm^2 on 1-4 µm micropillars, at diff. day 5 . . . 51
4.8 Flowchart of the image analysis process for evaluation of OPC cultures purity . . . 53
4.9 Representative images of GFAP$^+$ cells in OPC cultures on control PDMS micropillars at diff. days 1 and 5 . . . 54
4.10 Quantification of GFAP$^+$ cells in OPC cultures on control PDMS platforms at diff. days 1 and 5 . . . 54
4.11 Representative images of IBA1$^+$ and βIII tubulin$^+$ cells in OPC cultures on control PDMS micropillars at diff. days 1 and 5 . . . 55
4.12 Quantification of IBA1$^+$ cells in OPC cultures on control PDMS platforms at diff. days 1 and 5 . . . 55

4.13 Quantification of βIII tubulin$^+$ cells in OPC cultures on control PDMS platforms at diff. days 1 and 5 56
4.14 Estimation of OPC purity for cultures on PDMS platforms and TCPS wells at diff. days 1 and 5 57
4.15 Representative images of acquired channels in INCell Analyzer 2000 for OPC cultures in PDMS platforms at diff. day 5 59
4.16 Representative examples of oligodendroglial cells in differentiation stages I-IV 60
4.17 Flowchart of the image analysis process for evaluation of OLs differentiation stage ("Collar Occupancy" pipeline) 61
4.18 Flowchart of the image analysis process for evaluation of OL myelin area and micropillars' wrapping ("Myelinated micropillars" pipeline) . . 63
4.19 Representative images of OPC cultures on control and soft PDMS platforms, at diff. day 1 65
4.20 Quantification of differentiation and micropillars' wrapping in OPC cultures on control and soft PDMS platforms at diff. day 1 66
4.21 Representative images of OPC cultures on control and soft PDMS platforms, at diff. day 5 68
4.22 Quantification of differentiation and micropillars' wrapping in OPC cultures on control and soft PDMS platforms at diff. day 5 69
4.23 Quantification of MBP gene expression levels in OPC cultures on control and soft PDMS platforms at diff. day 5 70
4.24 Representative confocal image of mature, myelinating OLs on control PDMS micropillars, at diff. day 5 71
4.25 Representative confocal image of myelin rings wrapping around micropillars 71
4.26 Representative field of live imaging of OPCs seeded on mixed micropillars for two diff. days 72

B.1 Example of an Experion^{TM} analysis for assessment of RNA integrity . 97
B.2 Example of an eletropherogram and virtual gel report obtained from an Experion^{TM} analysis 98
B.3 Amplification curves and standard curves of tested primers 99

C.1 Identification of Nuc and NucExp objects from original DAPI image. . 103
C.2 Confusion matrix of the Random Forest algorithm trained for classification of objects into GFAP-positive and negative classes 104
C.3 Confusion matrix of the Random Forest algorithm trained for classification of objects into IBA1-positive, βIII tubulin-positive or double negative classes 105

D.1 Ilastik segmentation of tubulin channel images 107
D.2 Identification of Collar objects from Nuc and NucExp objects 108
D.3 Identification of Cell network objects from ilastik-segmented tubulin channel images 109
D.4 Identification of Collar mask and Protrusions in Collar 110
D.5 Final overlay of Nuc, Collar and Collar mask objects 111
D.6 Histogram of Olig2 mean intensity values in Nuc objects 112
D.7 Plot of collar area vs. nucleus area for each object 112

E.1 Ilastik segmentation of brightfield, MBP wix1 and MBP wix2 image channel images 116

E.2 Identification of MBPinFocus primary objects from ilastik-segmented MBP wix1 images 117
E.3 Identification of Pillars primary objects from ilastik-segmented bright-field images and creation of PillarsExp secondary objects 118
E.4 Filtering of PillarsExp according to area and form factor and identification of FilterPillars and FinalPillars objects 119
E.5 Identification of MBPpillars primary objects from ilastik-segmented MBP wix2 channel images 120
E.6 Final overlay of MBPinPillars and FinalPillars objects' outlines 121
E.7 Histogram of MBP mean intensity values in NucExp objects 121

G.1 Quantification of differentiation and micropillars' wrapping in OPC cultures on control PDMS platforms at diff. days 1 and 5 126
G.2 Quantification of differentiation and micropillars' wrapping in OPC cultures on soft PDMS platforms at diff. days 1 and 5 127

List of Tables

1.1 Summary of papers exploring *in vitro* models to study the influence of substrate/ECM stiffness or contact with axonal-like structures in oligodendroglial cell development and myelination. 16

3.1 Composition of MGCs' culture medium 31
3.2 Composition of OPC cultures' differentiation medium 33
3.3 Antibody mixes for ICC of neuronal cell types 35
3.4 MBP and YWHAZ primers' sequences 37

4.1 Measurements of diameter at mid-length, base and top of micropillars, length and distance between micropillars for PDMS micropillars 43
4.2 G*, G' and G" determined by amplitude and frequency sweep tests, and E calculated from the correspondent G*, for PDMS 45
4.3 G*, G' and G" determined by amplitude and frequency sweep tests, and E calculated from the correspondent G*, for 3:1 and 2:1 PDMS-to-dimethicone ratio 46
4.4 Measurements of diameter at mid-length, base and top of micropillars, length and distance between micropillars for soft PDMS micropillars . 49
4.5 Cell seeding densities tested on PLL/laminin-coated PDMS platforms 50

B.1 MBP, YWHAZ and 18S primers' sequences 98
B.2 Amplification efficiency obtained from standard curves of tested primers 99

D.1 Parameters used for analysis of the Collar Occupancy pipeline results. 113

E.1 Parameters used for analysis of the Myelinated Micropillas pipeline results. 122

F.1 Quantification of GFAP$^+$, IBA1$^+$ and βIII tubulin$^+$ cells and estimation of OPC purity in OPC cultures on control PDMS platforms at diff. day 1 123
F.2 Quantification of GFAP$^+$, IBA1$^+$ and βIII tubulin$^+$ cells and estimation of OPC purity in OPC cultures on control PDMS platforms at diff. day 5 124

List of Abbreviations

ANOVA	**AN**alysis **O**f **VA**riance
AR	**A**spect **R**atio
BBB	**B**lood-**B**rain **Barrier**
BDNF	**B**rain-**D**erived **N**eurotrophic **F**actor
CNS	**C**entral **N**ervous **S**ystem
CSPG	**C**hondroitin **S**ulfate **P**roteo**G**lycan
EAE	**E**xperimental **A**utoimmune **E**ncephalomyelitis
ECM	**E**xtra**C**ellular **M**atrix
FAK	**F**ocal **A**dhesion **K**inase
FBS	**F**etal **B**ovine **S**erum
FGF	**F**ibroblast **G**rowth **F**actor
GalC	**Gal**actocerebroside
GDNF	**G**lial cell line-**D**erived **N**eurotrophic **F**actor
GFAP	**G**lial **F**ibrillary **A**cid **P**rotein
HA	**H**yaluronic **A**cid
HBSS	**H**ank's **B**alanced **S**alt **S**olution
HDDA	**H**exane**D**iol **D**i**A**crylate
IBA1	**I**onized Calcium-**B**inding **A**dapter Molecule **1**
ICC	**I**mmuno**C**yto**C**hemistry
IFN-γ	**I**nter**F**ero**N** γ
IGF-1	**I**nsulin-like **G**rowth **F**actor **1**
ILK	**I**ntegrin-**L**inked **K**inase
LVR	**L**inear **V**iscoelastic **R**egion
MAG	**M**yelin-**A**ssociated **G**lycoprotein
MBP	**M**yelin **B**asic **P**rotein
MGC	**M**ixed **G**lial **C**ulture
MHC	**M**ajor **H**istocompatibility **C**omplex
MHC-B	**M**yosin **H**eavy **C**hain- **B**
MOG	**M**yelin **O**ligodendrocyte **G**lycoprotein
MRE	**M**agnetic **R**esonance **E**lastography
MS	**M**ultiple **S**clerosis
NDS	**N**ormal **D**onkey **S**erum
NG2	**N**eural/**G**lial antigen **2**
NRG-1	**N**euro**R**e**G**ulin **1**
OL	**OL**igodendrocyte
OPC	**O**ligodendrocyte **P**rogenitor **C**ell
PA	**P**oly(**aA**crilamide)
PDGFRα	**P**latelet-**D**erived **G**rowth **F**actor **R**eceptor α
PDMS	**P**oly(**D**i**M**ethyl**S**iloxane)
pHEMA	**P**oly(2-**D**ydroxyl**E**thyl **M**eth**A**crylate)
PLLA	**P**oly(**L**-**L**actic **A**cid)
PLP	**P**roteo**L**ipid **P**rotein
PS	**P**oly(**S**tyrene)

P/S	**P**eninciline/**S**treptavidine
PSA-NCAM	**P**oly**S**i**A**lylated-**N**eural **C**ell **A**dhesion **M**olecule
RT-qPCR	**R**everse **T**ranscriptase **Q**uantitative **P**olymerase **C**hain **R**eaction
SEM	**S**canning **E**lectron **M**icroscopy
T3	**Tri**iodo**T**hyronine
TCPS	**T**issue **C**ulture **P**oly**S**tyrene
TNF-α	**T**umor **N**ecrosis **F**actor α

List of Symbols

G*	Complex shear modulus
G'	Shear modulus (elastic component)
G"	Shear modulus (viscous component)
E	Young's modulus
ν	Poisson's ratio

Chapter 1

Introduction

Myelination had a tremendous impact on the evolution of vertebrates, particularly concerning motor, sensory and high-order cognitive functions of the central nervous system (CNS). The formation of myelin internodes causes insulation of the correspondent axonal segments, so membrane depolarizations are restricted to nodes of Ranvier (short unmyelinated segments between myelin internodes). Consequently, action potential propagation occurs in a saltatory manner, causing an extraordinary increase in the velocity of nervous impulse propagation with no significant extension of axonal length (Fig. 1.1(A)). Moreover, myelin reduces neuronal energetic costs and provides metabolic support to axons [1].

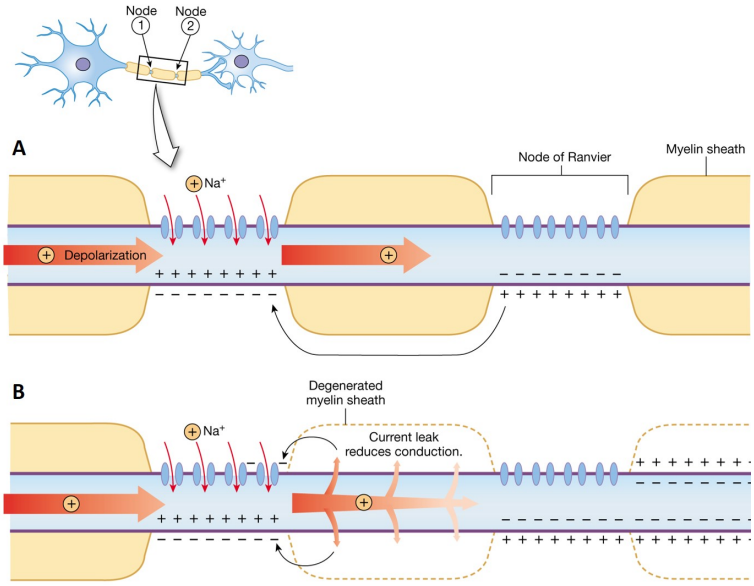


FIGURE 1.1: Saltatory conduction of action potential in a (A) myelinated axon (homeostasis) and (B) demyelinated axon (pathology). Adapted from `https:www.pearson.com/us/`

Oligodendrocytes (OLs) are the responsible cells for myelination in the CNS, but they are also known to support axonal functions through metabolites and neurotrophic factors. Studies show that OLs support neuronal survival by both axoglial contact-mediated and soluble mechanisms, and provide metabolic support as well [2]–[4].

Myelination is the result of a process involving the continuous interaction between oligodendroglial cells, axons and their environment. In fact, OLs are derived from oligodendrocyte progenitor cells (OPCs). The “oligodendroglial cells” designation refers to all stages of this cell line, from OPCs to mature OLs. Oligodendroglial cells have a highly complex and dynamic morphology, which is related to its differentiation

program. OPCs are initially bipolar cells and, when starting morphological differentiation, extend multiple processes. These processes eventually establish contact and wrap axons, forming a highly specialized membrane domain, the myelin [5]. OPC differentiation and myelination are closely related processes, resulting in a mature OL with cytoplasmic extensions wrapping several axons (up to a 1:60 ratio) [1].

Myelin itself corresponds to a "multilayered stack of membranes, tightly attached at their cytosolic and external surfaces", with a specific set of lipids and proteins [6]. Therefore, OLs must synthesize large amounts of cytoplasmic membrane in order to form myelin internodes. Myelin has a high lipid content (73-81% of total dry weight) and a low protein:lipid ratio (1:4 in dry weight), which contributes to its insulation function. The main lipid classes are cholesterol, P-inositol-4,5-diphosphate (PI(4,5)P2) and phosphatidylethanolamine plasmalogen [6].

Loss of myelin is detected in a variety of CNS disorders from traumatic brain injury, spinal cord injury, viral infections, leukodystrophies to inflammatory demyelinating diseases [7], [8].

One must first distinguish primary from secondary demyelination. Secondary myelination is the result of Wallerian degeneration, where myelin damage occurs due to primary axonal loss, e.g. in brain or spinal cord injury [9]. On the other hand, primary demyelination (the concept of interest in this review) is usually the consequence of a direct insult affecting the myelinating cells. Therefore, demyelinating diseases of the CNS comprise a set of conditions where there is destruction of myelin internodes, followed by axonal and neuronal loss. The loss of myelin internodes causes impairment of saltatory conduction and leakage of the electrical signal, therefore decreasing the velocity of nervous signal conduction (Fig. 1.1(B)). In spite of being histologically and pathologically characterized to great extent, these conditions often have an idiopathic etiology, i.e. the clinical origin of the insult is unknown. The main causes for primary demyelination are genetic abnormalities that affect glia and inflammatory damage to myelin and/or OLs [10].

Multiple sclerosis (MS) is not only the most frequent demyelinating disease, but also the most common cause of neurological disability among young adults [11]. According to the National Multiple Sclerosis Society (USA), it is estimated that more than 2.3 million people are affected by this condition worldwide [11]. However, there is great geographical variation in prevalence, from high levels in Europe and North America (110/100,000 inhabitants) to low levels in Africa and Eastern Asia (2/100,000) (Fig. 1.2) [12]. This data suggests a role for environmental factors in MS risk [13]. A recent study estimates the real prevalence cumulated over 10 years may reach up to 309.2/100,000 inhabitants in the USA, considerably higher than previous estimates [14]. Life expectancy of MS patients is reduced by 6-14 years comparing with healthy people of the same age and gender [14]. MS patients are typically diagnosed between ages 15 and 55, i.e. working age adults, adversely affecting their quality of life and causing a significant social and financial burden. Annual total costs in 15 countries from Europe and North America are estimated to be over $41,000 per patient. It is also estimated that the work loss due to MS accounted for €3201 million in Europe, in 2007 [15].

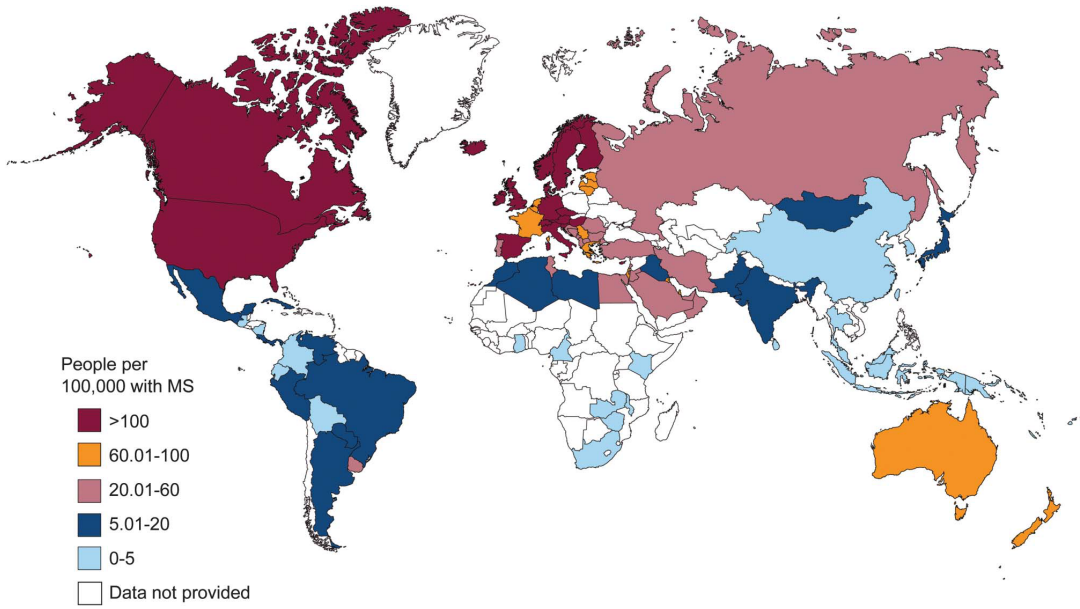


FIGURE 1.2: Global prevalence of MS in 2013. Adapted from [12].

The triggering factors of MS are still a matter of debate and are thought to be a result of the interplay of genetic and environmental elements [8]. The main hypotheses diverge between a primary immune response against myelin/OL-specific antigens or a secondary immune response to a myelin/OL injury [16]. The initial clinical signs of MS are optic neuritis (visual impairment and pain during eye movements), impairment in mobility, hand function, cognition and bowel/bladder function, as well as spasticity, pain and fatigue [17].

The majority of MS patients (85%) initially present a relapsing-remitting disease course, i.e. acute demyelination episodes followed by remyelination stages, with a partial recovery of saltatory conduction and function. Later, they present a secondary progressive neurological decline, with more intense demyelination episodes and ineffective recovery intervals, resulting in chronically demyelinated lesions [18].

Remyelination is the endogenous process of rewrapping axons with new myelin sheaths. It is hypothesized that the underlying mechanisms are similar to the developmental myelination program [19]. Taking into account the typical progression of MS, one could consider that a chronically demyelinated lesion is the result of a continuously unsuccessful myelin regeneration process [10]. Failure of remyelination is linked to axonal degeneration and loss, presumably due to the disruption of axoglial symbiosis, culminating in disease relapsing and progression [20]. Current treatments for MS reduce the number of attacks and decrease disease progression, mainly addressing the immune system. Nonetheless, MS is considered a chronic disease because there are no long-term neuroprotective therapies in the clinic [21].

Understanding de- and remyelination processes, in all their dimensions, is crucial to characterize tissue degeneration that follows CNS disorders of such nature. Ultimately, the identification of therapeutic targets could be useful to promote completion of remyelination.

Going beyond the classical biochemical study approach, increasing evidence supports that mechanosignalling should not be neglected in OPCs differentiation and myelination [22]–[24]. External biophysical cues (e.g. rigidity of substrate) are transduced through surface receptors into intracellular signalling pathways, resulting in the modification of gene expression and/or cytoskeletal responses. This mechanotransduction process is probably related to the activation of the myelination program

and might as well play a role in demyelination. As an emerging field, mechanobiology of (de)myelination relies on *in vitro* models, for a 'user-friendly' manipulation of experimental conditions and assessment of cellular responses with various techniques, building fundamental knowledge. However, the study of mechanobiology has posed some challenges, particularly regarding the recapitulation of the *in vivo* microenvironment. Various systems have been proposed, with associated advantages and limitations, but some key factors have failed to be appropriately mimicked.

Here, an overview of the developmental program of myelination in the CNS is provided, followed by a dissection of the conditions and processes which lead to demyelination, remyelination and its failure. The cytoskeletal components of oligodendroglial cells, as well as mechanotransduction mechanisms involved are briefly explained. Such data is crucial to understand the physical dimension in this context. *In vitro* systems developed and published so far to explore the influence of physical and mechanical cues of these events are reviewed. Finally, the platform proposed in the context of this project is presented and explored.

1.1 Myelination and demyelination in the central nervous system

1.1.1 Development of the oligodendroglial cell lineage and cellular mechanisms of myelination

The formation of myelin during development includes a finely-tuned pathway of OPC proliferation, migration, differentiation and wrapping of appropriate axons. Therefore, myelination is closely related to the OL developmental program, which includes a series of intermediate cellular states from OPCs to mature myelinating OLs. Activation of this program is tightly regulated by transcriptional factors, cytoskeleton modifications, cellular contact and density, growth factors and extracellular matrix (ECM) molecules. It is hypothesized that OLs have an intrinsic program that can promote myelination in the absence of axoglial contact. Nonetheless, this process is modulated by extrinsic signals [25].

OPCs derive from neural stem cells (NSCs) (Fig. 1.3) and are first detected in ventricular germinal zones of the brain and spinal cord, during mid embryonic stages in rodents [26].

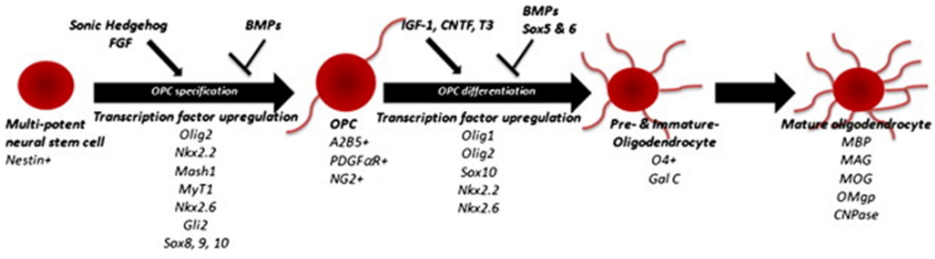


FIGURE 1.3: Oligodendroglial cell lineage: NSCs specification into OPCs and OPC differentiation into pre-myelinating and mature OLs. For each differentiation step, transcription factors, cell markers, promoters and inhibitors are presented [27]. Reprinted from "Cells of the oligodendroglial lineage, myelination, and remyelination", *Biochim Biophys Acta*, vol. 1812, no. 2, V. E. Miron *et al.*, pages 184-193, Copyright 2011, with permission from Elsevier.

These progenitor cells are highly proliferative, motile and have a bipolar morphology [25], [27]. They express the chondroitin sulfate proteoglycan (CSPG) neural/glial antigen 2 (NG2), platelet-derived growth factor receptor α (PDGFRα), glycolipid ganglioside marker D3 and A2B5 at the cell membrane level, which are generally recognized as OPC markers in literature (Fig. 1.3) [27]–[29]. Olig2, in particular, is expressed throughout the entire cell lineage and widely used as an oligodendroglial cell marker [29].

OPCs remain proliferative in their entire lifespan, including development, adult age and remyelination after insult. The most relevant mitogens include PDGF-A, neuroregulin-1 (NRG-1, which can be secreted or axonally-bound) and fibroblast growth factor (FGF) 1/2/18 [30].

OPC migration is also regulated by extracellular signals of various types. PDGF-A and FGF-2 stimulate cell motility. Cell-cell adhesion molecules (e.g. αvβ1 integrins, polysialylated-neural cell adhesion molecule (PSA-NCAM), NG2) and cell-ECM adhesion molecules (e.g. fibronectin, laminin, tenascin-C) guide migration [30].

After proliferation and migration, OPCs become distributed throughout both gray and white matter and account for 5-8% of all cells of the CNS [29].

OPCs differentiate through a pre-myelinating stage until becoming fully mature OLs. These cells dynamically extend and retract motile processes (fillopodia and lamellipodia), surveying the brain parenchyma to find suitable axons. Once the contact is stabilized, there is an association of the tyrosine kinase Fyn with lipid-rich microdomains, local enrichment of phosphoinositides in the membrane, activation of directed mRNA transport, local protein translation and extensive reorganization of the cytoskeleton. These molecular alterations contribute to the polarization of OPCs toward the axon to be myelinated [1].

At this point of differentiation, the cell is in a pre-myelinating stage. Although proliferative, pre-myelinating OLs present multiple processes, in contact with various axons simultaneously, therefore rendering their migratory capacity. Immature OLs are characterized by the expression of a sulfatide recognized by O4 antibody and galactocerebroside (GalC), still not expressing myelin-specific markers (Fig. 1.3) [27].

Terminal differentiation of OPCs and myelination are tightly coupled events. Various models have been proposed to explain axonal wrapping by OPC processes, at the membrane level. However, currently available imaging techniques are not enough to visualize the wrapping process in real time, with enough magnification and resolution. One of the most recent hypotheses proposes that OPC processes wrap around the axon, undergoing radial and lateral expansion. The inner tongue of the OPC process is pushed under the outer tongue and extends laterally at the same time [25]. Evidence suggests that the addition of new membrane to the inner tongue occurs through the coalescence of cholesterol-rich membrane microdomains. When the appropriate number of myelin wraps per axon is generated, compaction of these multiple membrane layers allows the formation of a mature myelin internode [28]. The intracellular surface of the membrane has negatively charged phospholipids, which repel themselves, but attract positively charged molecules such as myelin basic protein (MBP). *Mbp* mRNA is transported through cytoplasmic channels to OL processes and locally translated. By neutralizing the phospholipids, MBP pulls together two membrane bilayers, forming a compact myelin sheath [1]. Cytoplasmic channels close and the myelin internode is finally formed [28]. At this point, it is possible to define a g-ratio, i.e. fraction of circumference of the axon by the circumference of the myelin sheath. Fig. 1.4 presents a schematic view of the myelination process.

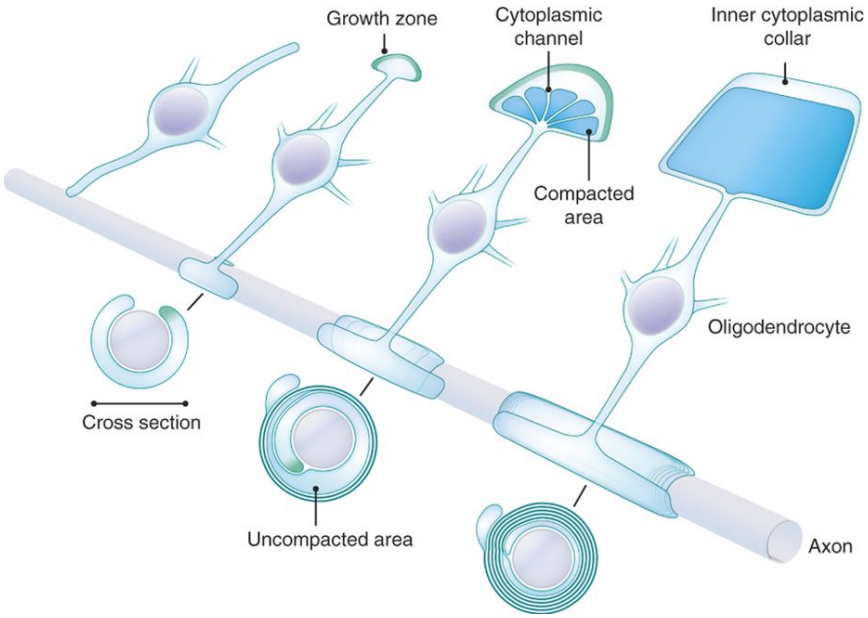


FIGURE 1.4: Myelination in the CNS: OPC's process extension, wrapping around axons and compaction of myelin sheaths [31]. Reprinted by permission from Springer Nature Customer Service Centre GmbH: Springer Nature, *Nature Neuroscience*, "Remodeling myelination: implications for mechanisms of neural plasticity", K. Chang *et al.*, Copyright 2016.

Concomitantly to wrapping, voltage-gated ion channels present in the axonal membrane undergo a clustering process. Sodium channels, which regulate electrical impulse conduction, are aggregated in the myelin-free nodes of Ranvier. On the other hand, potassium channels are concentrated in myelin areas called the juxtaparanodes. Myelin also forms the paranodes, the flanking membrane loops which separate the sodium channels from the potassium ones. Together, the paranode and juxtaparanode form the myelin internode that intercalates two nodes of Ranvier (Fig. 1.5) [27].

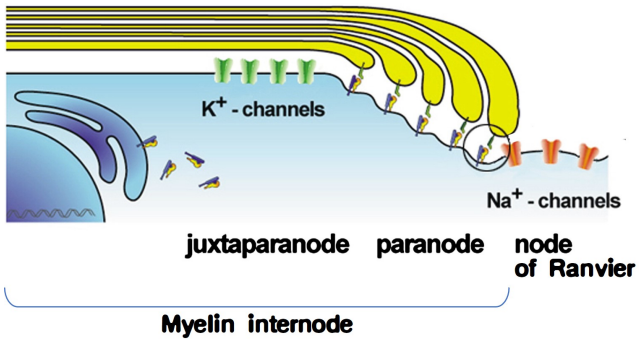


FIGURE 1.5: Structure of a myelin internode (juxtaparanode and paranode), node of Ranvier and distribution of ion channels [32]. Reprinted from "Contactin orchestrates assembly of the septate-like junctions at the paranode in myelinated peripheral nerve", *Neuron*, vol. 30, no. 2, M. E. Boyle *et al.*, pages 385-397, Copyright 2001, with permission from Elsevier.

Transcription factors such as Olig1/2, Sox10, Nkx2.2/2.6, myelin regulatory factor and Smad interacting protein 1 are responsible for activating the expression of myelin-related genes and intervene in a complex regulatory network [1], [27]. PI3K/Akt/mTOR and ERK/MAPK are some of the signaling pathways in OPCs and OLs which might be involved in regulation of myelination [25].

When compact myelin internodes are formed, OLs reach a mature stage. Myelinating OLs are post-mitotic, non-motile, have an extensively branched morphology and can be identified through myelin-related proteins. Particularly, OLs express MBP, myelin-associated glycoprotein (MAG), myelin OL glycoprotein (MOG) and 2',3'-cyclic nucleotide 3'-phosphodiesterase (Fig. 1.3) [27].

It is important to notice that, although terminal differentiation and myelination are related, they do not correspond to the same event. Hence, despite some common regulators, these processes are influenced by different promoters and inhibitors.

Mitogen withdrawal, such as PDGF-A and FGF-2, is enough to promote OPC terminal differentiation. Triiodothyronine (T3), brain-derived neurotrophic factor (BDNF) and insulin-like growth factor 1 (IGF-1) have also been identified as soluble factors that promote terminal differentiation. Some axonally-bound molecules have the same effect, e.g. NRG1 and laminin-2 [30].

Myelination is influenced by axoglial interaction [28]. Segregation of neighboring myelin internodes and internode length are controlled by myelin-associated inhibitors, such as Nogo [1]. Axonal support and electrical activity also influence the thickness and length of internodes [25]. Axons secrete neurotransmitters (e.g. glutamate) and growth factors (e.g. NRG1, BDNF), which bind to the respective receptors in OPCs. These cues activate signaling pathways which induce a rise in OLs cytoplasmic calcium, locally triggering translation of MBP to initiate myelination [33]. Therefore, although axonal support is enough to allow wrapping and formation of myelin-like sheaths, OLs have a "preference" for electrically active axons.

On the contrary, PSA-NCAM, leucine-rich repeat and immunoglobulin domain-containing-1 (LINGO-1), nerve growth factor, G protein-coupled receptor 17 ligand or CSPGs are examples of negative regulators which must be inhibited to allow for both OL terminal differentiation and CNS myelination [1].

OPCs maintain the capacity for motility, migration and differentiation into myelinating OLs in the adult CNS [25]. They give rise to OLs in the adult stage, which participate in myelin remodeling by either replacing non-viable OLs or intercalating among existing myelin sheaths [34]. Maintenance of myelin membrane comprises a continual turnover, correlated with a high level of expression of myelin-related genes long after the completion of the developmental process [27].

1.1.2 Demyelination in multiple sclerosis and remyelination mechanisms

In pathologies such as MS, as previously mentioned, there is destruction of myelin internodes and death of myelinating cells - i.e. primary demyelination.

MS is considered an autoimmune disease, where autoreactive T cells invade the CNS, attacking myelin and OLs. The development of inflammatory lesions is supposed to be an innate immune response, where host myelin/OL-specific antigens are activated and internalized by antigen presenting cells (APCs), such as dendritic cells and microglia, and exposed by their major histocompatibility complex (MHC)-II [35]. This response usually occurs with a transient blood-brain barrier (BBB) disruption, allowing for the infiltration of circulating immune cells, mainly T cells, B cells and macrophages [16], [36]. This leads to an adaptive immune response. CD4+ T

lymphocytes recognize the host antigens presented by the APCs' MHC-II, proliferate and secrete pro-inflammatory and myelinotoxic cytokines, e.g. tumor necrosis factor α (TNF-α) or interferon γ (IFN-γ) [37]. CD8+ T cells are also thought to be involved in the primary demyelinating insult, since OLs express MHC-I under inflammatory and stress conditions. Therefore, myelin/ OL-specific antigens can be exposed by OLs' MHC-I and recognized by CD8+ T cells, which exert a direct cytotoxic effect over myelinating cells [38]. Finally, B cells are also rising as important players in MS pathogenesis, since they produce antibodies against myelin/OL-specific antigens which lead to a humoral response, ultimately causing myelin destruction [39]. There is evidence of production of antibodies against MOG, MBP, proteolipid protein (PLP), MAG, Nogo and NG2 [40]. Axoglial junctions have been identified potential targets of the immune response [16].

It has also been considered a role for viral-mediated autoimmunity in MS pathogenesis. Viruses could cause demyelination by directly injuring OLs and/or triggering an autoimmune response [16]. The Epstein-Bar virus is one of the main examples of viral agents which can increase the MS risk [41].

Concerning the structure of the internode, demyelination typically starts with disruption of the paranodal region and may proceed to disarrangement of the entire internode [27]. There is an altered expression and distribution of internodal proteins, such as neurofascin 155, contactin-associated protein or paranodin [42]. Similarly, the type and organization of ion channels in the demyelinated axon is altered. In particular, there is an adaptive distribution of voltage-gated Na+ channels on previously internodal axolemma, which results in a continuous membrane depolarization and impairment of saltatory conduction of action potentials. Also, there is a pathological increase in intra-axonal Na+ and protease activation, ultimately leading to axonal apoptosis [10], [43].

Alterations during MS pathogenesis are not restricted to cell population, also affecting the ECM organization. In demyelinated areas of MS animal models, infiltration of immune cells is facilitated by a discontinuity of the basal lamina (in the BBB). Perineuronal nets, composed of proteoglycans and tenascin R, are also destroyed. There is deposition of fibrillar collagens, CSPGs and high-molecular-weight hyaluronic acid (HA). Fibrillar collagen may create a barrier that prevents further infiltration of circulating cells. On the other hand, the accumulation of CSPGs at the periphery of demyelinated lesions may also prevent the migration and repopulation by OPCs [44].

In response to severe brain tissue damage, astrocytes and microglia transit to a reactive state, proliferate and may form a glial scar [45]. One should note that demyelination not always results in the formation of a glial scar. Whether the glial scar is inhibitory or beneficial to CNS regeneration is a long-lasting debate in the field. When formed, the glial scar serves as a barrier between healthy tissue and the lesion core, which may contain meningeal fibroblasts, pericytes and infiltrating inflammatory cells, for example. This prevents further inflammatory damage and preserves tissue integrity. On the contrary, the glial phenotype and ECM components also prevent axonal regrowth and remyelination [27], [45].

Demyelinating diseases such as MS cause permanent disability. Such disability is the result of neuronal degeneration and/or persistent blockage of nervous impulse transmission in affected axons [46]. Different hypotheses have been proposed to explain the mechanisms linking demyelination with axonal degeneration - in other words, why demyelinated axons eventually degenerate.

Mechanisms hypothesized for exacerbated apoptosis of demyelinated neurons include: (i) impairment of saltatory conduction and excessive protease activation

[43]; (ii) lack of trophic support from OLs to neurons [3]; (iii) vulnerability caused by lack of myelin sheath protection [10], [46]; (iv) damage of synapses and ischemia caused by microglia-produced inflammatory mediators (e.g. TNF-α, nitric oxide) and (v) attack by infiltrating immune cells (T cells, B cells and macrophages) [46], [47].

Nevertheless, the CNS has a default response to demyelination, which shares features with regenerative processes of other body tissues. Remyelination in the adult CNS was first observed in the cat spinal cord. Shortly after an insult which caused demyelination, axons were embraced by sheet-like glial processes, and around 64 days later, all axons presented a thin myelin sheath [48]. Indeed, remyelination is a process where myelin sheaths are restored to demyelinated axons, recovering saltatory conduction and reducing functional deficits [10].

According to the recapitulation hypothesis, remyelination corresponds to a recapitulation of the developmental program of OPCs for migration, proliferation, differentiation and, finally, formation of myelin sheaths [19]. Indeed, *in vivo* evidences indicate that OPCs, and not mature OLs, are responsible for remyelination in adult CNS lesions [49], [50].

In response to an insult to myelin or OLs, local OPCs undergo a switch from a quiescent state to a regenerative phenotype, reacquiring proliferative, migratory and differentiation capacity. OPC activation can be caused by platelets and macrophages (which infiltrate brain parenchyma due to disruption of BBB), as well as pro-inflammatory cytokines, such as TNF-α, transforming growth factor β, interleukine-1α and IFN-γ [51]. On the other hand, astrocytes and microglia become reactive following a CNS injury, and there is evidence of crosstalk between the different glial cell types, leading to OPC activation and recruitment [52]. After migration, OPCs extend processes towards demyelinated axons, establish contact and wrap them, the myelin sheaths are compacted and a new myelin internode is formed (Fig. 1.6).

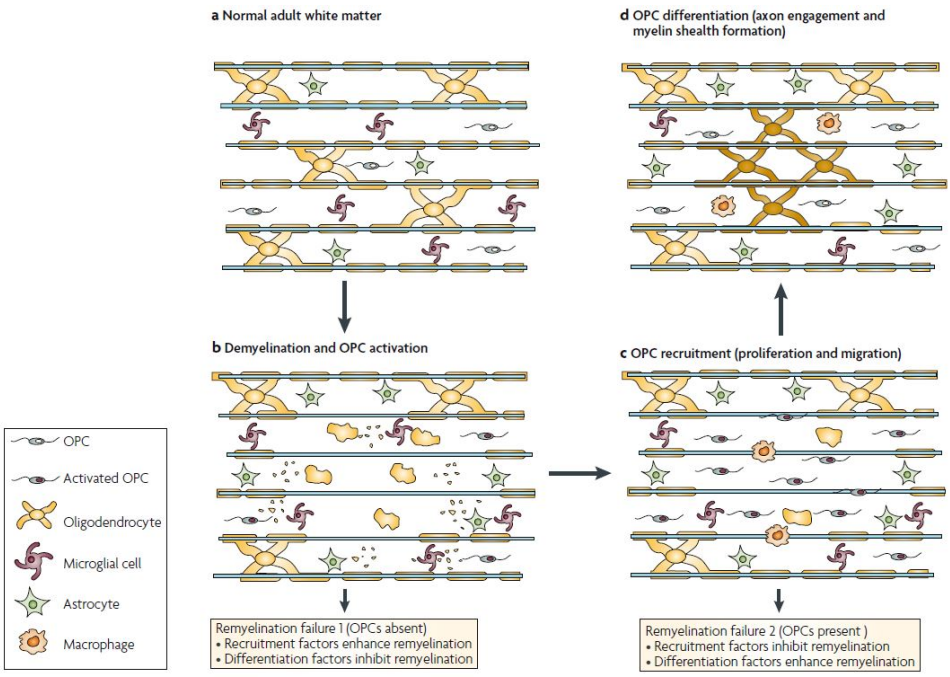


FIGURE 1.6: Remyelination and hypotheses for failure of the process [10]. Reprinted by permission from Springer Nature Customer Service Centre GmbH: Springer Nature, *Nature Reviews Neuroscience*, "Remyelination in the CNS: from biology to therapy", R. J. M. Franklin and C. ffrench-Constant, Copyright 2008.

Although remyelination is supposed to be a rerunning of the OPCs' developmental program, some differences between both processes have been identified. For example, regenerated myelin sheaths are thinner and shorter than the original ones, for a given axonal diameter, i.e. the g-ratio increases [53].

Considering this regeneration capacity, chronic demyelination ultimately corresponds to failure of myelin repair mechanisms. Therefore, understanding the remyelination process and its rate-limiting steps is crucial to determine how chronically demyelinated lesions are formed and develop therapeutic strategies which might support and/or promote this mechanism. Various hypotheses have been put forward to explain failure of myelin regeneration.

Focusing on disease-specific factors, it has been proposed that remyelination itself, after repeated demyelinating insults (e.g. relapsing-remitting MS) could cause a depletion of OPCs in the CNS. Experimental data, however, shows such phenomenon is not significant [54].

Other hypotheses are related to failure of OPC recruitment, differentiation and/or maturation. These are not mutually exclusive and most likely all contribute for the process.

In inflammatory conditions, the recruited OPCs and newly-formed myelin sheaths can be subjected to the same degree of insult as the initial OLs and internodes [10]. Therefore, these conditions can affect OPC survival, proliferation and differentiation. For example, MS patients generate antibodies against NG2, meaning there is probably an adaptive auto-immune response against OPCs, preventing their remyelinating function [55].

There are still, however, OPCs expressing O4, NG2, PLP, Olig2 and Nkx2.2 in MS lesions, suggesting that there are other factors preventing remyelination downstream in the process [56]–[58].

An overexpression of inhibitors of differentiation in the lesion is another plausible explanation. In the demyelination lesion, there is an accumulation of myelin debris (with MOG and MAG) and HA [59]. There is also an upregulation of axonally-expressed inhibitors, particularly Nogo, LINGO-1 and PSA-NCAM [27], [60], [61]. Reactive, hypertrophic astrocytes express Jagged1, a soluble factor which also inhibits differentiation [62]. In short, demyelinated axons are less easily myelinated than healthy axons during development.

Evidence concerning the effect of inflammatory signals in the remyelination process are somehow contradictory. While it is logical that OPCs might be a direct target of the inflammatory conditions, it has also been proposed that these signals are important for OPC activation and recruitment. The dysregulation hypothesis proposes that efficient remyelination depends not only on the presence and absence of promoter and inhibitory cues, respectively, but also on their precise timing of action. In other words, remyelination fails as a result of a temporal discordance between these cues, either because (i) a pro-recruitment environment is not maintained for a sufficient long time, (ii) the premature onset of a pro-differentiation environment arrests recruitment before the lesion is populated by OPCs or (iii) pro-recruitment signals are differentiation inhibitors and remain unresolved by the time OPCs repopulate the lesion (such as with acute inflammation) [63].

Remyelination is also affected by non-disease-related factors such as age, sex or genetic background [64]–[66].

Chemical signaling involved in these processes – developmental myelination, de- and remyelination – has been extensively explored [30], [67], [68]. However, the precise influence of physical and mechanical cues remains to be determined. During demyelination, the ECM composition is greatly altered (as aforementioned),

therefore suggesting that the mechanical properties of brain tissue may also change. Recent research shows that mechanotransduction plays a role in other neurodegenerative pathologies, such as Alzheimer's or Parkinson's disease [69]. Hence, it is possible that mechanosignalling plays a role in demyelinating diseases like MS, as well. A more comprehensive research on the mechanobiology of myelination may be important for the development of efficient therapies against such pathologies.

1.2 Mechanobiology in (de)myelination

Mechanical cues are becoming more popular in the stem cell biology scene, causing a paradigm shift. Indeed, mechanically-directed differentiation has been proved in mesenchymal, hematopoietic, embryonic, adipose-derived and even neural stem cells [70], [71]. Considering that OPCs have been proven to be mechanosensitive cells, it is, therefore, probable that mechanical cues also have an influence on de-, re- and myelination processes [72].

Mechanotransduction consists on the conversion of physical signals and forces (both intra- and extracellular) into chemical processes. The generated chemical signals may be transmitted to the cell nucleus, affecting gene expression. Hence, mechanotransduction comprises processes that mediate biological responses – from cell morphology, adhesion or fate decision – to various types of physical stimuli [73], [74].

Oligodendroglial cells explore the surrounding microenvironment and, depending on the mechanical cues (from cell-ECM and cell-cell interactions) provided, either proliferate, migrate or undergo terminal differentiation. On the other hand, various intracellular forces are also intrinsically generated. The cytoskeleton plays a major role in all these phenomena, establishing a two-way interaction between the intra- and extracellular environment.

In this section, an overview of the brain's mechanical properties and their alteration in pathological conditions will be provided, followed by a deeper explanation of the mechanisms mediated by cytoskeleton that influence oligodendroglial cells behavior.

1.2.1 Alterations in brain's mechanical properites in (de)myelination

Brain tissue is one of the softest tissues in the human body, with a Young's modulus of 0.1-1 kPa [72]. Nonetheless, it is important to notice that the myelination process itself influences brain's mechanical properties. Stiffness increases 2-3 times in both grey and white matter upon myelination and maturation, suggesting myelin is not only important for insulation and saltatory conduction, but also for axonal protection against physical insults [75], [76]. Alterations in brain parenchyma stiffness caused by demyelinating diseases are visible in MS. In particular, post-mortem analysis of gross anatomy of sclerotic plaques showed these areas were stiffer and shrunken in comparison to surrounding brain tissue [77], [78].

In vivo studies of brain mechanical properties rely on magnetic resonance elastography (MRE), a non-invasive technique used to measure parenchyma viscoelasticity [79]. Although few, studies using MRE in MS patients and different demyelination animal models mostly show a decrease in brain viscoelasticity, i.e. softer tissue, reduced parenchyma volume and loss of mechanical network geometry in acute demyelination lesions [80]–[84]. Works performed by Riek and Schregel further show

a recovery of the viscoelastic modulus during remyelination [81], [82]. However, Millward and co-workers found no alterations in brain viscoelasticity in demyelination in wild type C57BL/6 mice [84]. Such contradictory conclusions may be explained by the insufficient macroscopic spatial resolution of MRE or differences in animal models.

For more precise measurements of brain's mechanical properties in homeostatic and pathological conditions, resolution provided by MRE is insufficient. Post-mortem microscopic analysis of demyelinated lesions is an attractive alternative for such end.

Recent research using nanoindentation atomic force microscopy in the analysis of tissue from different demyelination models shows that mechanical properties differ between acute and chronic lesions. Acute demyelinated lesions are softer in comparison to healthy tissue. These lesions retain potential for remyelination and, when it happens, stiffness levels recover to normal values. On the contrary, chronic demyelination lesions are stiffer than healthy white matter [85], which could be related with the increased deposition of ECM components such as fibrillar collagens (e.g. collagen I) and fibronectin. The same technique has been applied for the mechanical characterization of glial scar in the injured rat cortex. The glial scar was significantly softer than the correspondent healthy CNS tissue. The decrease in stiffness correlated with an upregulation of expression of vimentin, GFAP, laminin and collagen IV. However, between 9 and 23 days post-injury, there was a partial recovery of the elastic modulus of cortical tissue and reduction of expression levels of laminin and collagen IV [86]. Although there is no direct correspondence between the glial scar and demyelinated sites, both of the aforementioned studies should be taken into consideration in the study of mechanobiology of sclerotic lesions where astrogliosis occurs.

In conclusion, alterations in brain stiffness and deterioration of the mechanical scaffold during demyelination are a result of changes in cerebral parenchyma and reduced myelin content as well.

1.2.2 Mechanotransduction and cytoskeletal behaviour of oligodendroglial cells

The oligodendroglial cells' cytoskeleton includes three main components: microtubules, actin microfilaments (F-actin) and myosin II motors, the latter two forming an actomyosin network. Intermediate filaments do not have a significant expression in this cell lineage [87], so they will not be considered in this review.

After a few days in culture, OLs present 5-10 main microtubule-enriched processes, as well as filopodia and lamellipodia rich in F-actin, the latter driving branching [88]. While microfilaments are present in the leading edges of these protrusions, microtubules do not extend to the most distal regions. Further differentiation into mature OLs results in the formation of a network with interbranch connections.

Microtubules are essentially responsible for cell morphology and organelle trafficking along OL processes, allowing the transport to the leading edge of organelles, mRNA granules and proteins for myelin assembly and maintenance [89].

Recent experiments with a zebrafish live imaging model and rat co-cultures of OLs and neurons have provided some interesting insights on the involvement of actin microfilaments in OPCs motility and myelination [90], [91]. OPC processes are adhered to the substrate. Actin filaments are present at the tip of the exploratory filopodia and lamellipodia, which extend and retract dynamically. When contacting with an axonal structure, there is an extensive assembly of microfilaments in this

direction, forming a motile leading edge, non-adherent to the axon. F-actin polymerizes in the leading edge, pushing the OL membrane around the axon, radially and laterally. Subsequent to the wrapping of various layers, the actin filaments are disassembled, reducing membrane surface tension and converting the leading edge into an adherent myelin layer. Such mechanism explains why F-actin is absent from mature compact myelin. In short, a coordinated assembly and disassembly in repetitive cycles leads to edge protrusion and spreading, allowing for progressive wrapping around the axon and myelin layer formation (Fig. 1.7) [90], [91].

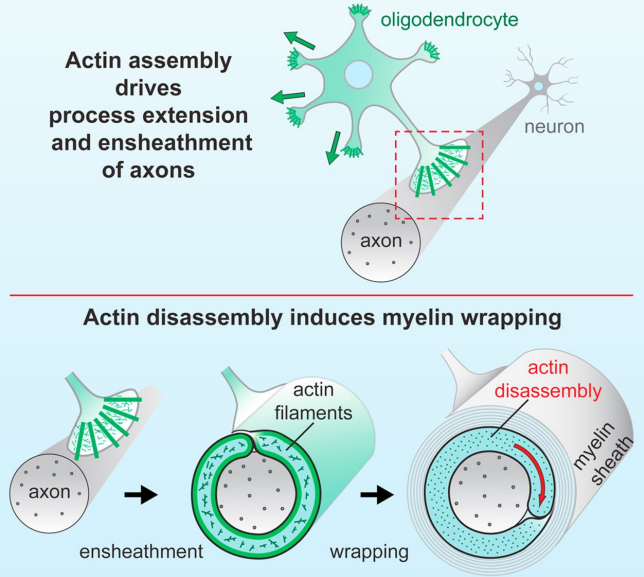


FIGURE 1.7: Actin assembly and disassembly during myelin wrapping [91]. Reprinted from "CNS myelin wrapping is driven by actin disassembly", *Developmental Cell*, vol. 34, no. 2, J.B. Zuchero *et al.*, pages 152-167, Copyright 2015, with permission from Elsevier.

Actin microfilaments interact closely with non-muscle myosin II motors. This actomyosin complex regulates process outgrowth in OPCs and myelin maintenance in OLs. During process outgrowth and wrapping, myosin heavy chain B (MHC-B) is bound to and pulls on F-actin, generating the necessary contractile forces. However, during myelin sheath formation, actin filaments are disassembled, and the expression of MHC-B decreases, so the interaction between myosin and F-actin diminishes sharply, as well as the membrane tension [92].

The described cytoskeletal behaviour is a response not only to intrinsic gene expression, but also to mechanosignalling from ECM components or other cells. Mechanotransduction is mainly possible through membrane receptors of the integrin family. Oligodendroglial cells express an array of integrins throughout differentiation. Particularly, $\alpha 6\beta 1$ and $\alpha v\beta 1$ integrins are strongly expressed in OPCs, while $\alpha v\beta 8$ and $\alpha v\beta 1$ are mainly expressed in mature OLs [93].

After integrins bind to a ligand, adaptor proteins establish a connection between the integrin's β-subunit and actin filaments, forming large complexes – focal adhesions. Focal adhesions are "key sensory machineries" that integrate extracellular signals and allow intracellular interaction between integrins and number of different proteins and kinases, initiating signalling pathways which influence OPC fate and myelination [71].

Integrins may bind to focal adhesion kinase (FAK), which interacts with actomyosin complexes and activates MAPK, PI3K and Rho signalling pathways, for example [71]. FAK has a regulatory role in the efficiency and timing of OPC maturation and early stages of myelination [94]. The effect is dependent on the ECM substrate. For OLs cultured on fibronectin, FAK activity constrains process network expansion. On the other hand, in the presence of laminin-2, FAK promotes morphological maturation [95].

Integrins also interact with Src family kinases. In oligodendroglial cells, fibronectin binding to β1 integrins activates the Fyn kinase which, in turn, activates Cdc42 and Rac1. These small GTPases promote actin polymerization at focal adhesions [87].

Moreover, integrins may interact with integrin-linked kinase (ILK). During OPC process outgrowth, laminin-2:α6β1 integrin interaction activates ILK [87]. This enzyme inhibits the RhoA/ROCK pathway, reducing actin disassembly and promoting actin polymerization. ILK activity promotes differentiation of OPCs to pre-myelinating OLs, branching and formation of myelin membranes [96].

1.3 Models to study the influence of mechanical forces in (de)myelination

The most common animal models to study de- and remyelination are based on localized and systemic administration of myelinotoxic substances (e.g. ethidium bromide and cuprizone, respectively) or experimental autoimmune encephalomyelitis (EAE, the most significant inflammatory model to study MS) [97]. However, the use of these type of systems in mechanobiology research has several limitations.

Firstly, studies with animal models are hardly reproducible and comparable, resulting in conflicting conclusions, as mentioned before. Additionally, one should notice that it is difficult to discern whether demyelination is caused by signaling factors or mechanical factors *in vivo*. Physical or mechanical aspects (e.g. ECM stiffness, axonal diameter) cannot be modulated by the operator. In conclusion, animal models are frequently unsuitable to study mechanotransduction and the influence of physical cues in de-, re- or myelination. Moreover, the various animal models for demyelination do not recapitulate all features of MS in humans. For example, de- and remyelination processes are reported to be less extensive and more acute in the EAE model than in humans [97].

Thus, *in vitro* models pose as an attractive alternative to understand the mechanobiology of demyelination. Contrary to the *in vivo* scenario, these systems allow the user to uncouple biochemical and mechanical cues. Taking into account that new-born mouse/rat oligodendroglial cells cultured *in vitro* in the absence of neurons phenotypically resemble the *in vivo* counterparts, these systems could be used to study the effect of mechanical cues *per se* [88], [98].

Within *in vitro* models, cell culture might be performed in two-dimensional (2D) or three-dimensional (3D) models. Most published studies rely on 2D culture of OL lineage cells. Although providing significant knowledge about myelination, these systems lack the topological support provided by the brain parenchyma. On the other hand, 3D systems more closely resemble the *in vivo* environment. Each cell is free to move and extend processes in all directions and can interact with multiple neighboring cells simultaneously, much alike what happens when an OPC differentiates, establishes contact with multiple axons and myelinates them. In particular, hydrogels can be tailored to provide 3D scaffolds mimicking the plasticity and stiffness of

brain parenchyma. Hydrogel-based 3D systems have been widely used for disease modelling, so they can be adapted to this type of study as well.

Conceptually, it is possible to consider various types of mechanical forces that cells can experience. Regarding externally applied forces, cells can be subjected to tension, compression, shear, swelling and membrane curvature forces, either from cell-ECM or cell-cell contact. Endogenous forces (developed from within the cell via the cytoskeleton) will not be focused here. In this section, a critical review and comparison of studies focusing on the influence of matrix stiffness and axoglial contact is performed. A summary of these research papers can be found in Table 1.1.

1.3.1 *In vitro* models of the influence of substrate/matrix stiffness

Different studies have proved that OPCs are mechanosensitive. Overall, for OPCs cultured on polyacrylamide (PA) gels of a wide range of stiffnesses (0.1-70 kPa), a stiffer substrate promotes a decrease of OPCs adhesion, proliferation and increase of migration, cell surface area, branching and differentiation [72], [99]. The optimal PA stiffness for differentiation corresponds to a Young's modulus of 1 kPa, which is within the stiffness range of brain parenchyma (0.1-1 kPa) [107]. Interestingly, OPCs themselves have a viscoelastic behavior, stiffening during differentiation [72]. Inhibition of Rho/ROCK signaling and myosin IIB resulted in a recovery of cell surface area and branching, revealing that the influence of mechanical properties is mediated by actomyosin contractility [99], [101].

OPCs behavior on PA gels of optimal stiffness significantly differed from those cultured on polystyrene (PS) or glass. For considerably stiffer substrata, some results are contradictory. For example, Urbanski and colleagues concluded that PA gels with 30 kPa inhibited branching and differentiation [101].

One must notice that the aforementioned studies correspond to 2D culture of OPCs. There are morphological and functional differences between OPCs cultured on substrates or within matrices, as proven by some authors [108], [109]. OPC morphology is flat and biased along the plane of the surface for 2D substrates, but round within HA 3D matrices. Inclusion of components that allow for matrix remodeling (e.g. from basal lamina) greatly improve cell integration, so OPCs extend long processes [109].

For HA gels of physiological stiffness (approximately 120 Pa), 3D culture of OPCs increases sprouting processes per cell (indicating differentiation) in comparison to 2D cultures on HA gels as well [100].

Together, these results provide motivation to revisit results about OL biology obtained on 2D rigid surfaces (e.g. glass, PS), but, most importantly, to adopt 3D matrices with physiologically relevant stiffness for future work.

1.3.2 *In vitro* models of the influence of axoglial contact

OLs are able to elaborate myelin membrane when cultured in the absence of neurons, suggesting an intrinsic program for the development of myelin membrane [110]. Yet, axonal contact and signaling are known to have a significant impact in CNS myelination [1], [25]. Therefore, mimicking axoglial contact in *in vitro* systems would more closely resemble the *in vivo* environment during CNS myelination. Various approaches have been developed to achieve this goal, from cocultures of OL lineage cells and neurons [111]–[115], to cultures with paraformaldehyde (PFA)-fixed axons [115], microfibers (horizontally-oriented structures) (Fig. 1.8(B)) [26], [102]–[104], [106] or micropillars (vertically-oriented structures) (Fig. 1.8(A)) [105], [106].

TABLE 1.1: Summary of papers exploring *in vitro* models to study the influence of substrate/ECM stiffness or contact with axonal-like structures in oligodendroglial cell development and myelination. References are indicated for each study according to the main text. Measurements indicated in the second part of the Table refer to fiber diameter.

Study	Substrate	Stimulus	Response	Ref.
Models of the influence of substrate/ECM stiffness				
Kippert et al., 2009	PA gels	↓ Stiffness (0.5, 1, 4.5, 6.5 kPa)	↓ Cell area	[99]
Jagielska et al., 2012	PA gels	↓ Stiffness (glass, PS, PA gels with 0.1, 0.4, 0.7, 1 and 70 kPa)	↑ Adhesion, survival, proliferation ↓ Migration, differentiation Optimal stiffness for OPC culture: 0.7-1 kPa	[72]
Li et al., 2013	HA hydrogels	3D culture (vs. 2D culture) Stiffness (4.8-624 Pa)	↑ Branching Optimal stiffness for OPC culture: 120 Pa	[100]
Urbanski et al., 2016	PA gels	↑ Stiffness (1.5 vs. 30 kPa)	↓ Differentiation	[101]
Models of the influence of contact with axonal-like structures				
Bullock et al., 2009	Glass microfibers (0.4 µm)	Glass microfibers (vs. 2D culture)	OLs cluster around microfibers ↑ Sulfolipids production	[102]
Howe et al., 2006	Glass (4 µm) or Vicryl (12 µm) microfibers	↓ Fiber diameter (4 vs. 12 µm)	↑ Wrapping, membrane thickness	[103]
Lee et al., 2012	PS microfibers	↑ Fiber diameter (2-4 vs. 0.2-0.4 µm)	↑ Differentiation, wrapping Minimum diameter for wrapping: 0.4 µm	[104]
Mei at al., 2014	Silica conic micropillars	Conic micropillars	Easier imaging and quantification of sheath diameter and length	[105]
Bechler et al., 2015	PLA microfibers	↑ Fiber diameter (0.5-1 vs. 1-2 vs. 2-4 µm)	↑ Sheath length	[26]
Espinosa-Hoyos et al., 2018	PDMS, pHEMA fibers p(HDDA-co-starPEG) fibers and pillars	↓ Fiber diameter (10 vs. 20 µm) ↑ Fiber stiffness (140 vs. 0.4 kPa)	↑ Differentiation, wrapping	[106]

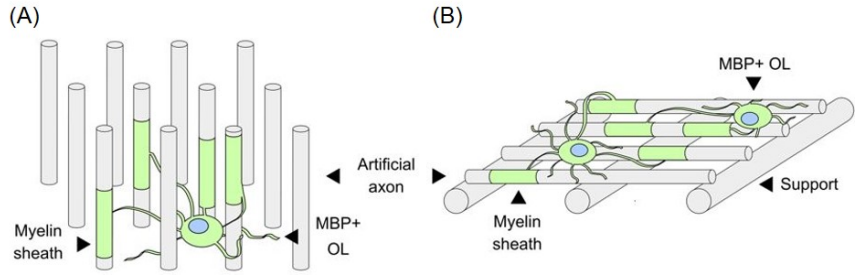


FIGURE 1.8: Schematic representation of micropillars (A) and microfibers (B) as *in vitro* artificial axons and OPC engagement and wrapping around the same. Adapted from [106] (open access article).

Although OPC-neuron cocultures might be the system that most faithfully represents the axonal cues that OPCs receive *in vivo* [111]–[115], they prevent the decoupling of molecular cues and biophysical properties of the axons – i.e. it is impossible for the user to know if a certain observed effect in OPCs/OLs is caused by biochemical or physical cues. For this purpose, alternative systems mimicking the axonal cylindrical architecture have been developed, cancelling molecular signaling effects.

Rosenberg and colleagues established a culture system where OPCs were seeded onto PFA-fixed dorsal root ganglia neurons, in order to determine what type of microenvironment constraints induce OPC differentiation. In this system, OPCs formed compact, concentric and multilaminar myelin-like sheaths around fixed axons. The group concluded that OPC differentiation is influenced by physical and geometrical constraints of the microenvironment, in a density-dependent manner: differentiation and myelination are more significant when OPCs are seeded in a higher initial density, through a mechanism of restriction of available axonal space [115].

Nonetheless, studying the influence of individual axonal cues on myelination (either physical or molecular) requires systems which provide more control on these same parameters than the previously mentioned PFA-fixed axons. Although PFA fixation preserves axons' physiological morphology and diameter, it does not allow the user to tune diameters/shapes and study the influence of these parameters in wrapping and myelination. Also, possible effects of PFA remnants in OPC morphology remain unknown. As an alternative, microfibers of various materials and stiffnesses have been explored– from glass, PS, polyglactin 910 (Vicryl), poly-L-lactic acid (PLLA), PDMS, poly(2-hydroxylethyl methacrylate) (pHEMA) to copolymers (Fig. 1.9) [72], [99], [103], [106], [116]. Fibers may be produced through electrospinning or, more recently, direct ink writing. These techniques allow the use of a wide range of materials and control of geometrical and mechanical properties.

Bullock et al. performed pioneering work, culturing neonatal rat OPCs with 0.4 µm-diameter glass microfibers, thinner than most biological axons. OPCs clustered around the fibers and presented an increased production of sulfolipids, which suggests that the physical cues promoted an increase of the production of membrane lipids in order to wrap these fibers [102]. Overall, OPCs adhesion is highly promoted by coating any type of fibers with PLL, Matrigel or ECM-derived preparations, in comparison to uncoated fibers – although it is not strictly necessary [103]. Across the studies on the influence of this stimulus on OPC differentiation and myelination, OPCs extend long processes, contact with multiple fibers simultaneously, when in contact with axonal surrogates. Additionally, it is possible to observe a concentric wrapping of these processes around the fibers, forming myelin sheaths of variable lengths [26], [103], [104], [106]. These features recapitulate the axoglial engagement

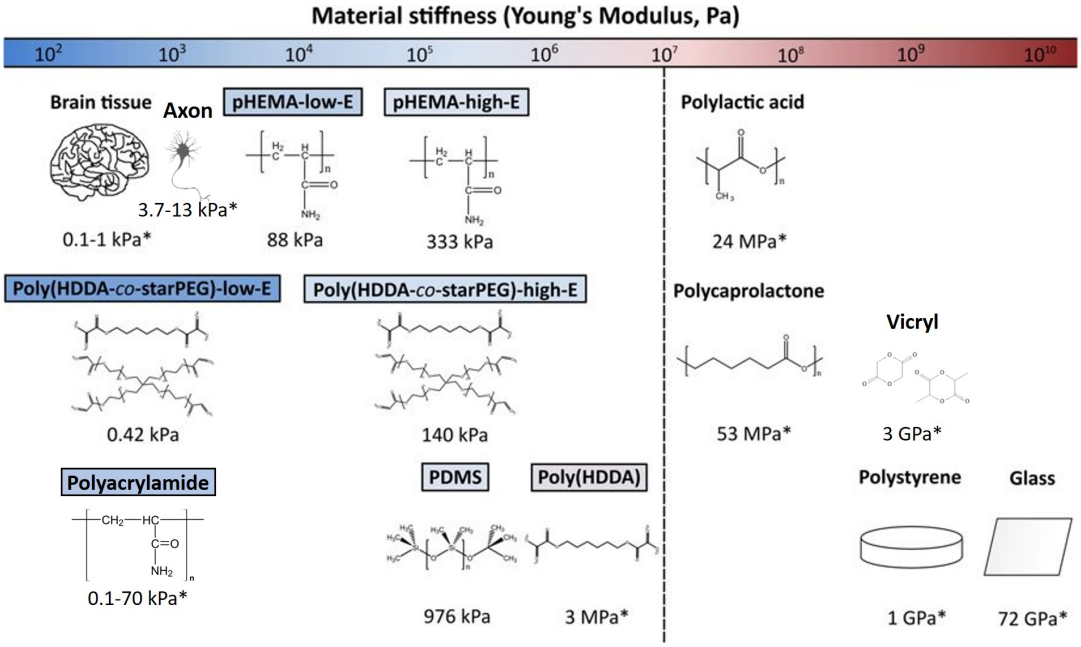


FIGURE 1.9: Young's modulus of materials used in various studies for myelination assays, either in 2D or 3D cultures, with microfibers or micropillars, and reference values of stiffness for brain parenchyma and axon. The dashed line indicates the difference between typically used (Young's modulus >10^7 Pa) and recently adopted materials (Young's modulus <10^7 Pa). *reported literature values from [72], [99], [103], [116]. Adapted from [106] (open access article).

in vivo. Howe et al. concluded that OPCs formed MBP^+ thick membrane sheaths around 4 µm diameter glass fibers, but only extended cell membrane projections on 12 µm-diameter Vicryl fibers [103]. Lee and co-workers compared small (0.2-0.4 µm) and large (2-4 µm) diameter PS fibers, concluding that OPCs extend membrane sheets on small-diameter fibers, but only form MBP^+ myelin-like segments around larger diameters. The minimum fiber diameter threshold for myelination was determined to be 0.4 µm [104]. Similarly, Bechler and colleagues tested OPC sheath formation around PLA fibers with 0.5-1, 1-2 and 2-4 µm diameter. Results revealed only a slight reduction in the number of sheaths for the smallest caliber microfibers, while large-diameter fibers lead to increased sheath lengths [26]. Moreover, work by Espinosa-Hoyos showed that OPCs wrapping around copolymeric fibers was three-fold greater for 10 µm- than for 20 µm-diameter fibers [106].

Nonetheless, microfiber systems have limitations. 2D imaging of formed myelin is challenging, with various confounding overlaying cell components, so visualization of concentric myelin wraps requires transversal cross-section. In addition, electrospinning is laborious and can only produce fibers with supraphysiological stiffness, due to the limited range of materials for which this manufacturing technique has been optimized [106].

Micropillars are one of the most recently explored alternatives. In these platforms, the axonal-resembling structure is vertically oriented, so that it is possible to directly observe concentric wrapping of OLs processes from a top view. Also, micropillar arrays can be fabricated through photolithography, an easy and ready for scale-up process, which makes them suitable for a high-throughput screening platform. Mei et al. designed a system of fused-silica conically-shaped micropillars, so that both diameter and length of a myelin internode could be interpolated from the dimensions

of the pillar using a single two-dimensional top-view compressed z-stack image. Culture of primary OPCs on these micropillars allowed for detection of concentric layers of myelin (Fig. 1.10(A-C)), and screening of 100 bioactive molecules resulted in the identification antimuscarinic compounds as promoters of OL differentiation and remyelination [105], [117]. It is particularly relevant to notice that OPCs wrapped MBP^+ sheaths around the base of micropillars, which were 50 μm in diameter. In spite of the technical advantage of this system, conic micropillars do not accurately represent the cylindrical geometry of axons and were made of silica, meaning they were highly stiff.

Once again, previous studies rely on materials orders of magnitude stiffer than the biological counterpart (axons). The influence of fiber diameter was concluded from studies using glass, PS and PLA fibers, which have Young's moduli of higher orders than MPa. On the other hand, axons have a predominant elastic behavior [118], with estimated initial and long-term elastic moduli of 12.86 kPa and 3.7 kPa, respectively [116], [118].

Espinosa-Hoyos' work aimed to develop mechanically compliant, unsupported, high-aspect ratio (AR) surrogates of biological axons. Using direct ink writing or projection micro-stereolithography, the group was able to produce PDMS and pHEMA fibers, as well as fibers and pillars of a copolymer of hexanediol diacrylate (HDDA) and polyethylene glycol (PEG), namely p(HDDA-co-starPEG) (Fig. 1.10(D-G)). The Young's moduli of printed fibers ranged 10^2-10^5 Pa, significantly lower than the previously used materials and closer to a biologically-relevant stiffness. Also, variation of diameter, stiffness and surface coating in p(HDDA-co-starPEG) fibers and pillars allowed to conclude that wrapping was threefold greater for 140 kPa pillars (vs. 0.4 kPa), 10 μm-diameter pillars (vs. 20 μm) and laminin-coated fibers (vs. PDL coating) [106].

Altogether, these studies provide an indication of the diameter permissive for concentric wrapping of OPCs processes. Axon surrogates must have at least 0.4 μm of diameter to allow for OPC wrapping and formation of myelin-like sheaths. Considering works by Mei and Redmond where OPC wrapping around conic micropillars with 50 μm sections was shown, it has not been established a maximum diameter for wrapping [105], [117]. *In vivo* observations show that CNS axons have diameters ranging from 0.2 up to more than 10 μm, and the majority is myelinated [119]–[121]. Hence, observations in this *in vitro* systems are consistent with the *in vivo* scenario, further showing that OLs can wrap even thicker axons. Also, fiber diameter is sufficient *per se* to initiate membrane wrapping, proving that no dynamic axonal signaling is necessary for the onset of myelination.

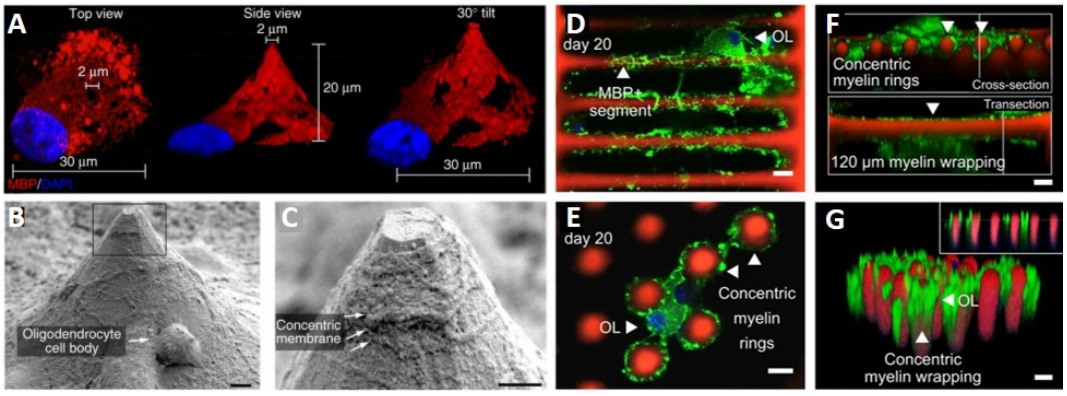


FIGURE 1.10: Culture of OPCs in microfibers or micropillars with various properties. (A) Single OL wrapping a conical micropillar. MBP (red) and DAPI (blue) staining. (B,C) SEM image of single OL wrapping a micropillar, with concentric layers of OL membrane. Scale bar: 1 µm [105]. (D-G) Fibers/pillars conjugated with rhodamine, MBP (green) and Hoechst (blue) staining. Scale bar: 10 µm. (D,F) OPC engagement and wrapping around p(HDDA-co-starPEG) microfibers with Young's modulus of 140 kPa, at diff. day 20, on top view (D) and cross-section (F). (E,G) OPC engagement and wrapping around p(HDDA-co-starPEG) micropillars with Young's modulus of 0.42 kPa, at diff. day 20, on top view (E) and transection (G) [106]. (A-C) Reprinted by permission from Springer Nature Customer Service Centre GmbH: Springer Nature, *Nature Medicine*, "Micropillar arrays as a high-throughput screening platform for therapeutics in multiple sclerosis", F. Mei *et al.*, Copyright 2014. (D-G) Adapted from [106] (open access article).

1.4 Development of a high-throughput micropillars-based platform for *in vitro* recapitulation of oligodendrocyte differentiation and myelination

Although increasing attention has been devoted to the mechanobiology of myelination, the influence of various mechanical/physical aspects in OPC differentiation, axonal wrapping and myelination is still poorly understood - not only in homeostatic myelination, but also in the pathological scenario of demyelinating diseases. Some *in vitro* approaches have paved the way to unravel the physical dimension of these processes, proving that mechanobiology must be included in the equation for a complete understanding of myelination.

In short, one must be careful when choosing the substrate for oligodendroglial cell culture. 2D culture on substrates as stiff as glass or PS is not advisable: it has been shown that the resultant morphology and phenotype is not representative of the *in vivo* scenario. Future *in vitro* approaches systems will probably rely on hydrogel-based systems with physiologically-relevant stiffness (0.1-1 kPa) for 3D culture of OPCs.

Summarizing the information in the previous section, overall, axonal surrogates with a diameter in the 2-10 µm range seem to promote higher OPC differentiation, wrapping and formation of myelin-like sheaths, in comparison to much thinner or thicker fibers/micropillars [26], [103], [104], [106]. However, in some of the aforementioned studies, conclusions about the influence of axonal diameter were drawn by making comparisons between fibers with very different diameters and very distant from the *in vivo* scenario (for example, comparing 10 µm to 20 µm fibers [106]). Moreover, the various explored systems are highly distinct among themselves, meaning comparison of results should be done carefully. Therefore, it is still

unknown whether a particular, biologically-relevant diameter promotes OPC differentiation and wrapping *in vitro*.

Acknowledging this issue, the present work aims to develop a new platform of axonal surrogates with physiologically-relevant morphology, dimensions and mechanical properties. Micropillars are the most attractive approach for high-throughput systems, given the ease of imaging and amount of information the user ought to obtain. Such high-throughput systems could be adapted for the study of various aspects of mechanobiology and mechanotransduction in myelination, as well as drug screening.

In order to study the influence of axonal diameter in myelination, PDMS micropillars with 1-5 µm diameter were used. This range was selected based on published results using other *in vitro* systems [26], [103], [104], [106], as well as average diameters of myelinated axons in the mammalian CNS [119], [121]. Micropillars were projected to have 10 µm in length and be inter-spaced by 30 µm, so that seeded cells fall inbetween these structures and not on top of them. Fig. 1.11 presents the basic design of these micropillars' platforms.

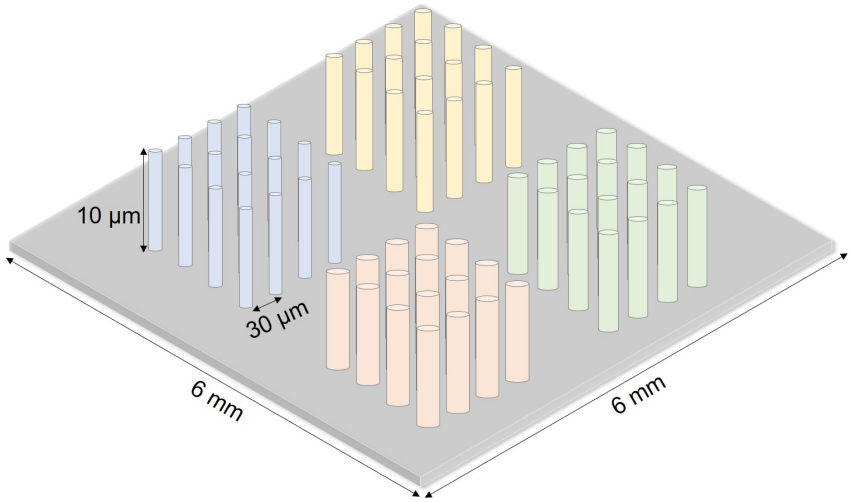


FIGURE 1.11: Design of PDMS micropillars' platform. Schematic representation of a micropillars' platform, indicating dimensions that are constant for all types of micropillars (width, micropillars' length and space between micropillars).

The squared platform is composed of 4 quadrants. There are three main types of squared platforms, according to the diameters in each quadrant: (i) micropillars with 1, 2, 3 and 4 µm diameter in each quadrant (i.e. 1-4 µm micropillars), (ii) micropillars with 2, 3, 4 and 5 µm diameter in each quadrant (i.e. 2-5 µm micropillars) and (iii) alternate micropillars of with 1, 2, 3 and 4 µm in all quadrants (i.e. mixed micropillars) (Fig. 1.12). Additionally, PDMS flat surfaces were also fabricated to be used as controls for the influence of micropillars. The 1-4 and 2-5 µm micropillars design allows the user to easily compare different diameters and conclude about their influence in wrapping and myelination. Micropillars were projected to have 10 µm in length. In this case, the AR corresponds to the ratio length/diameter, and varies from 2 (for 5 µm micropillars) to 10 (for 1 µm micropillars).

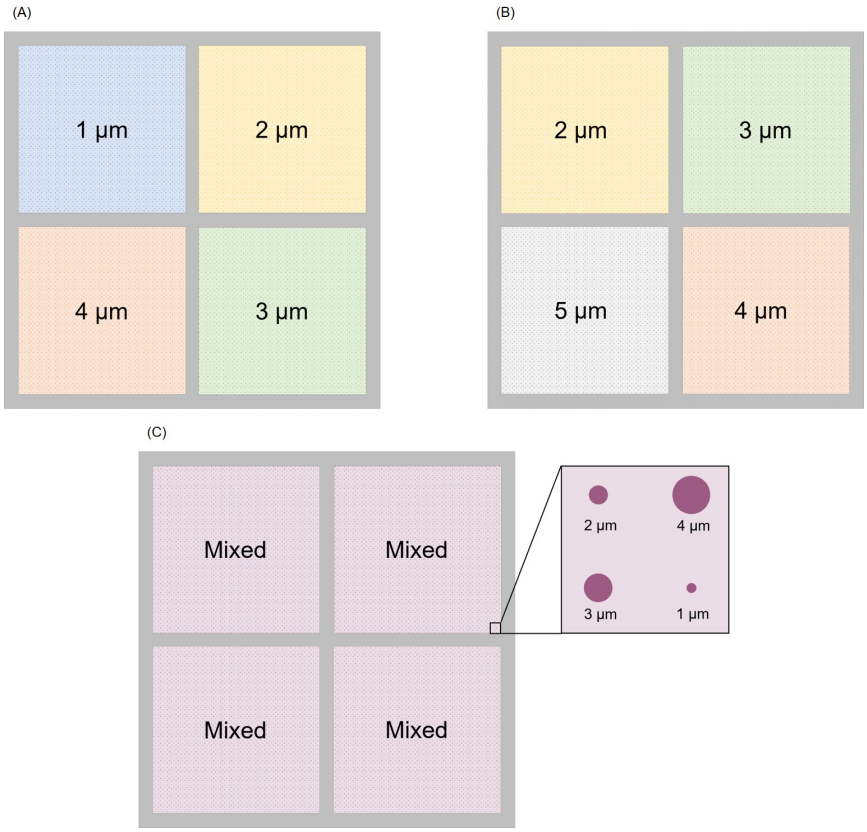


FIGURE 1.12: Schematic representation of quadrants in micropillars' platforms, namely (A) 1-4 µm micropillars, (B) 2-5 µm micropillars and (C) mixed micropillars.

PDMS is one of the most widely used polymers for microfluidic applications, due to its biocompatibility, ease of fabrication, mechanical properties, optical transparency, gas permeability and low price [122]. Its chemical and physical properties are extensively characterized [123].

The Young's modulus of PDMS is variable - from 0.1 MPa up to 2.97 MPa [106], [124]. Although stiffer than the axon, PDMS is still considerably softer than TCPS (1 GPa) or glass (72 GPa), the substrates classicaly used for cell culture. Moreover, the mechanical properties of PDMS samples can be modulated. In conclusion, PDMS poses as a good candidate for the fabrication of the aforementioned micropillars.

PDMS has an inorganic siloxane backbone and lateral organic methyl groups. Commercially, it is supplied as a rubber base and a curing agent, which form a prepolymer when mixed. Cross-linking of the polymer chains starts once the two components are mixed and is accelerated by exposure to high temperatures, resulting in the formation of a solid elastomer. PDMS has a high elastic modulus, i.e. it can be easily deformed, but it recovers the original shape after deformation. The final mechanical properties of the material are strongly influenced by curing temperature and time. For example, an increase in curing temperature from 25 to 200 ºC more than doubles the Young's modulus of PDMS (from 1.32 to 2.97 MPa) [124]. PDMS is mainly inert and non-cytotoxic. It is almost optically transparent in the range of visible wavelength (240-1110 nm), which makes it compatible with fluorescence-based methods. Hence, this polymer is suitable for cell culture after sterilization, hydrophilization and appropriate coating [122].

In order to recapitulate the myelination process *in vitro*, it is necessary to follow the OPC differentiation process, since it is intimately related with the myelination

process itself. OLs and pre-myelinating OLs do not proliferate *in vitro* and already have multiple processes, which could compromise their ability to wrap around micropillars. On the contrary, OPCs extend multiple processes which, when in contact with an axon, wrap around it several times, forming concentric membrane sheaths and, finally, a compact myelin internode.

Cell lines allow the user to obtain a large number of homogeneous, metabolically active cells, throughout a long period of time. However, these cells correspond to a more immature stage and the induced genomic alterations may disrupt the phenotype of the mature OLs eventually derived from these progenitors [125]. Some oligodendroglial cell lines reported in literature include OL-1, CG-4 and OLP6.

On the other hand, primary cultures closer resemble the *in vivo* scenario, both genotipically and phenotipically. Despite the inherent challenges (cell population heterogeneity and variability between biological replicates), primary rat OPCs were selected for this system.

Several methodologies have been used to isolate rat OPCs, from immunopanning, fluorescence-activated cell sorting, differential gradient centrifugation to shaking methods [126]. In order to reduce the complexity and cost of the isolation protocol, the shake-off method based on differential adherent properties of glial cells was selected [127]. This method is widely used for isolation of rat OPCs from mixed glial cultures (MGCs), including in the majority of systems reported in the previous section.

Chapter 2

Motivation and Objectives

Physical and mechanical cues have been found to have an impact in OPCs' process outgrowth and the formation of myelin-like sheaths, as suggested by *in vitro* and *in vivo* observations. Thus, it is logical to presume that these cues must be considered for a more complete comprehension of the processes of myelin formation and regeneration. It can be hypothesized that these factors could constitute possible therapeutic targets in the context of demyelination scenarios such as MS.

Nonetheless, critically analyzing the published models (reported on Table 1.1 of Chapter 1), it is possible to conclude that none of them presents axon surrogates with biologically relevant diameters as well as low substrate stiffness, while being technically advantageous for high-throughput screening. Therefore, a need for a system that closely resembles the *in vivo* microenvironment experienced by oligodendroglial cells has been identified.

These premises constituted the motivation for the present thesis, that proposes the development of a new *in vitro* high-throughput system capable of mediating the recapitulation of the processes of OPC differentiation and axonal wrapping. Our ultimate goal is to contribute to the uncovering of the impact of physical and mechanical stimuli on OL differentiation and myelination. The proposed platform is composed by PDMS micropillars of different diameters that will serve as surrogate axons. It is hypothesized that micropillars with diameters ranging from 1-5 μm and PDMS substrates with different stiffnesses differentially promote OPC differentiation and axonal wrapping.

Specific objectives of this project included:

1. Exploration of PDMS formulations for the production of micropillars and evaluation of the resulting substrate's mechanical properties;
2. Establishment of OPC cultures on micropillars;
   (a) Optimization of cell seeding density;
   (b) Evaluation of purity of OPC cultures through an automated image analysis method using open source software (particularly CellProfiler and CellProfiler Analyst) for quantification of GFAP$^+$, IBA1$^+$ and βIII tubulin$^+$ cells;
3. Assessment of the effect of micropillar diameter and substrate stiffness on OPC differentiation and myelination;
   (a) Development and optimization of automated image analysis methods using open source software (particularly ilastik and CellProfiler) for quantification of protein expression (Olig2, MBP and α-tubulin), towards the establishment of an *in vitro* high-throughput system;
   (b) Evaluation of gene expression (MBP) through Reverse Transcriptase quantitative Polymerase Chain Reaction (RT-qPCR);
   (c) Live imaging of OPC differentiation and micropillar wrapping.

Chapter 3

Materials and Methods

3.1 Fabrication of micropillars' platforms

3.1.1 Fabrication of PDMS micropillars' platforms

PDMS was obtained using Silastic® T-2 Translucent Base (viscosity 50,000 mPa.s) and Curing Agent (Dow Corning). PDMS prepolymer was prepared in a 10:1 base-to-curing agent ratio. Micropillars were fabricated by casting PDMS prepolymer into a silica wafer mold (produced by collaborators from TU Delft) and curing at 60 ℃ for approximately 1h15'. After polymerization, the micropillars were peeled off from the mold with isopropanol, cut out, grouped according to diameters and stored in isopropanol. PDMS flat surfaces (used as controls) were fabricated similarly. Fig. 3.1 illustrates the fabrication process of PMDS micropillars.

In order to decrease the substrate stiffness, micropillars of were also manufactured from a mixture of PDMS (10:1 ratio) with 360 Medical Fluid (viscosity 100 cSt, Dow Corning) (hereon designated dimethicone). Different mixtures were tested, namely 2:1 and 3:1 total PDMS-to-dimethicone ratios (w/w), and the respective polymerization time was determined.

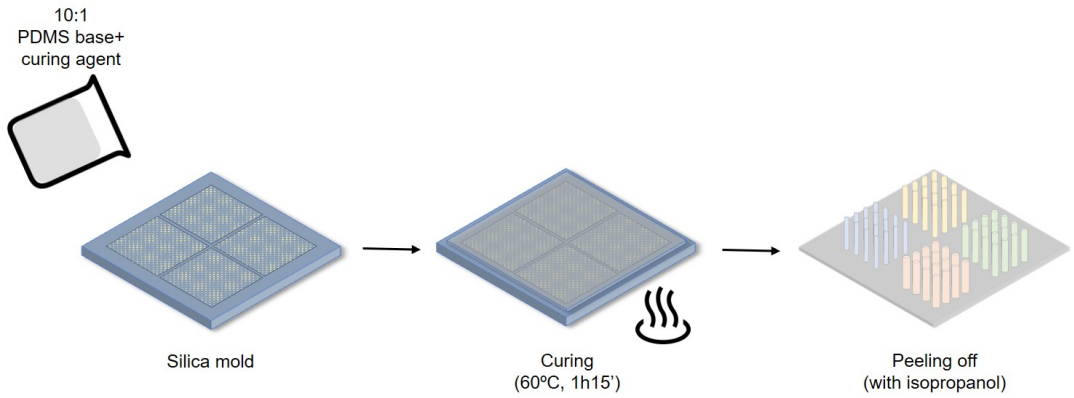


FIGURE 3.1: PDMS fabrication process using a silica wafer mold (produced by collaborators from TU Delft).

3.1.2 Critical point drying

Critical point drying with CO_2 was performed to dry PDMS surfaces and maintain micropillars upright. This technique takes advantage of critical point properties in order to avoid tangential forces caused by surface tension in liquid-gaseous interfaces, which would lead to deformation and micropillars' collapse [128]. Achieving critical point of water (374.2 ℃, 3197 psi) or isopropanol (235.2 ℃, 691 psi) would not only

be technically difficult but would also likely destroy PDMS samples [129]. Therefore, CO_2 is typically chosen as a transitional fluid for this procedure given its low critical point (31.1 ℃, 1084 psi) [128], [129]. However, it is important to notice that solubility of CO_2 is higher in ethanol than in isopropanol or water. Therefore, PDMS micropillars were washed with an increasing gradient of ethanol:isopropanol (50:50 and total volume of 99% ethanol) for a complete substitution of isopropanol for ethanol.

In the critical point dryer (Polaron Range CPD7501, Quorum Technologies), 6-7 cycles of flush (at 4℃, 800 psi) were performed in order to substitute ethanol for liquid CO_2, i.e. an increasing gradient of liquid CO_2:ethanol. Temperature and pressure were increased until 36-37℃ and 1000-1100 psi, surpassing the critical point and bringing CO_2 to its supercritical phase. After such, maintaining a constant critical point temperature (36-37℃), pressure was decreased at a maximum rate of 100 psi/min, allowing the conversion of CO_2 to the gaseous phase without surface tension phenomena [128]. PDMS surfaces (particularly high AR micropillars) were dried and their shape and position were preserved. After this procedure, PDMS surfaces were stored in a desiccator (low humidity atmosphere) until use.

3.1.3 Plasma treatment and coating of PDMS micropillars

After polymerization, PDMS has hydrocarbon groups ($-C_xH_y$), mainly methyl groups ($-CH_3$), exposed [130]. Consequently, PDMS surfaces are nonreactive and very hydrophobic. This would prevent further surface functionalization for cell adhesion and differentiation, as well as micropillars' collapse once these were submerged again. In order to increase hydrophilicity, promote exposure of reactive groups and sterilize PDMS platforms, these were submitted to plasma treatment, at low pressure, using the Diener Electronic Zepto Plasma Cleaner. During plasma treatment, the electrical charges incident on PDMS surfaces cause oxidation and formation of silanol groups ($-SiO_x$) (Fig. 3.2) [130].

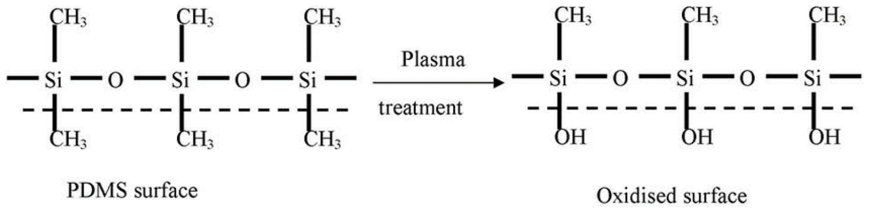


FIGURE 3.2: PDMS surface modifications with plasma treatment.

After placing the samples in the chamber and generating vacuum (pressure stabilized to 0.3 mbar), room air was inserted into chamber, increasing the pressure to 0.8 mbar. Subsequently, plasma was generated (at 20% intensity) and samples were treated for 3'. Finally, the chamber was ventilated, samples were removed and immediately transferred to a 24-well plate under a flow hood (maintaining sterility).

Because the PDMS surface modification is very fast (estimated to last only up to 5'), coating of PDMS surfaces with low molecular weight poly-L-lysine (PLL, Sigma P2636, molecular weight 30,000-70,000) was performed immediately after plasma treatment. PDMS surfaces were coated with PLL (50 µg/mL, 500 µL/well), left incubating overnight (ON) (37℃, 5% CO_2) and washed twice with type II water. Following this, PDMS platforms were coated with laminin 211 (Biolamina LN211, 10 µg/mL, 20 µL drop carefully placed on top of the PDMS surface) and incubated for 2h (37℃, 5% CO_2). No washing was performed after laminin coating.

Both PLL and laminin solutions were reused up to three times for coating.

3.2 Characterization of PDMS platforms

3.2.1 Rheology

In order to characterize the mechanical properties of materials used in micropillars, rheological measurements using the Kinexus Rheometer (Malvern Instruments Ltd.) were conducted.

Materials used in these platforms (particularly PDMS and PDMS:dimethicone of different ratios) are elastomers and can, therefore, be characterized by viscoelastic properties such as complex shear modulus (G*), elastic shear modulus (G') and viscous shear modulus (G").

Hence, 4mm-diameter flat discs of the aforementioned materials were used to perform oscillation tests with a 4mm parallel-plate geometry, at 37ºC and 0.1-0.2% compression. In order to determine the linear viscoelastic region (LVR), 3 amplitude sweep tests were performed at a constant oscillation frequency of 1 Hz. Once the LVR for each material was defined, 3 oscillation frequency sweep tests were conducted. For amplitude sweep tests, samples were submitted to strains in the range of 0.5-150%, at a constant frequency of 1 Hz (10 points per decade). For frequency sweep tests, samples were submitted to oscillations in the range of 0.1-10 Hz, at a constant strain of 5% (10 points per decade). Values of G*, G' and G" were determined from both types of tests. For each type of oscillation test, n=3 technical replicates were analyzed. The tolerance range of deviation for G*, G' and G" around the plateau value was $\pm$ 5%. Stiffness of the materials used in micropillars, as defined by the Young's modulus (E), was then calculated using G*. For linear isotropic materials, G* and E are related through the equation $E = 2G^*(1 + \nu)$, where ν stands for the Poisson's ratio [131]. The PDMS 4 mm-diameter discs were admitted to be isotropic (i.e. mechanical properties have identical values in all directions) and $\nu = 0.5$ was used as a reference value from literature for the Poisson's ratio [123].

3.2.2 Scanning electron microscopy

To observe the structure of the PDMS micropillars, scanning electron microscopy (SEM) analysis was performed.

Samples were coated with a gold/palladium thin film by sputtering, using the SPI Module Sputter Coater equipment. Coating was initially performed with a 45º tilt for 40", and then from a top view for 40".

Samples were then observed using the High Resolution Quanta 400 FEG ESEM, from a top view (no inclination) and lateral view (90º tilt). Diameter at mid-length, base and top of micropillars, length (from lateral view images) and distance between micropillars (from top view SEM images) determined from 3 measurements in different pillars in a single image of each type of micropillars (i.e. each unique condition).

3.3 Animals

All procedures involving animals and their care were performed in agreement with institutional ethical guidelines (IBMC/INEB/i3S), the EU directive (2010/63/EU) and Portuguese law (DL 113/2013). Experiments described here had the approval of Portuguese Veterinary Authorities. Animals had free access to food and water, being kept under a 12-h light/12-h dark cycle.

An Introductory Course on Laboratory Animal Science following FELASA Category B recommendations was taken. The course included a theoretical and practical component, with the correspondent evaluation, as well as Tutorial Training (10h). The obtained Certificate can be found in Appendix A.

3.4 Cell culture

3.4.1 Brain dissections and collection of cortices

Primary mixed glial cultures (MGCs) were obtained from P1-2 Wistar Han rats, as previously described [127].

Neonatal rat pups (usually a litter of 8-12 pups) were euthanized through decapitation. Brain dissection was performed in order to collect pre-frontal cortices. All instruments used in the process were previously sterilized by heat exposure (250 ºC, 60') and carefully cleaned with 70% ethanol.

Holding the left ear with a big forceps, the skin on top of the head was cut in a caudal-to-rostral direction, pointing a sharp scissor upwards and frontwards and avoiding touching the scalp with the scissor tip. The skin was separated from the scalp by pulling each part of the skin to opposite sides. Holding the head with the tweezers (without pressing to avoid brain damage), with a straight micro-scissor, the underlying cranial bone was also cut using a similar technique. Small transversal cuts from the midline to the lateral part were done, diving the skull bone in four parts. Separating the four parts to each correspondent side with a thin forceps, the brain was exposed. Sweeping the forceps under the brain (from the olfactory bulbs to the cerebellum) and making a cut at the cerebellar region, the brain was detached and collected in a Petri dish with Hank's Balanced Salt Solution without calcium or magnesium (HBSS, Sigma H2387-1L) 2% peninciline/streptavidine (P/S) and maintained on ice (in order to decrease tissue degradation and cell death). Afterwards, cortex isolation was performed in HBSS 2% P/S and under a magnifying glass. Brain hemispheres were separated with a thin forceps. Turning the medial side of one hemisphere up and fixing the cerebellar extremity, meningeal tissue was carefully detached from the cortex and discarded. The cerebellum and tissue underlying the cortex were removed and discarded as well. The isolated pre-frontal cortices were maintained in HBSS 2% P/S and on ice until dissociation.

3.4.2 Mixed glial cultures

The use of neonatal rat pups for primary MGCs ensured neuronal progenitor cells were already differentiated, hence theoretically preventing neuronal proliferation and survival in *in vitro* cultures. Typically, there is a stratification of glial cell types in culture, as reported [127]. Astrocytes adhere firstly and form an underlying layer, initially presenting a narrow morphology, but adopting a spread, quiescent-like morphology as cultures proceed. Oligodendroglial cells and microglia, on the other hand, adhere on top of the astrocyte layer. These two glial cell types have a similar morphology when in MGCs - round, bright cells, smaller than astrocytes. Given this stratified organization, the confluency of the astrocyte layer is particularly important to ensure that OPCs have a suitable substrate to adhere and proliferate.

After collection and once under the flow hood, HBSS medium was substituted by sterile HBSS 2% P/S (1 mL per collected brain). Mechanical digestion was promoted by pipetting the cortices up and down until obtaining a visibly homogeneous suspension, followed by extrusion through a 25G needle. The suspension was incubated with DNAse (0.1 mg/mL, Sigma D5025-15KU) and trypsin-EDTA (0.0025%, Gibco 25200) for 15', 37℃, flicking the tube every 5'. DNAse promotes degradation of DNA residues from cells destroyed during tissue mechanical digestion (which could itself cause increased cellular toxicity). Simultaneously, trypsin promotes enzymatic digestion and dissociation into single cells. These enzymes were inactivated by adding the same volume of culture medium (described in Table 3.1) to the suspension. After centrifuging (500 G, 10', Eppendorf 5810R) and discarding the supernatant, the pellet was resuspended in culture medium, transferred through a 70 µm nylon cell strainer (Falcon 352350) and distributed to PLL-coated T75 flasks (SPL Life Sciences) (2 collected brains per T75 flask). Fig. 3.3 illustrates this protocol.

MGCs were incubated for 4 days (37℃, 5% CO_2) to allow for cell adhesion and proliferation. On day 4, 4-5 mL of culture medium were refreshed (to let remaining cells attach). Afterwards, culture medium was refreshed every 2 days.

TABLE 3.1: Composition of MGCs' culture medium. Concentrations indicated in v/v are in relation to the final medium volume.

Components	Concentration
Dulbecco's Modified Eagle's Medium (DMEM) Glutamax High Glucose (Gibco 31966-021)	
Fetal Bovine Serum (FBS, Gibco 10270-106), *Heat inactivated (56℃, 30')*	10% (v/v)
P/S	1% (v/v)

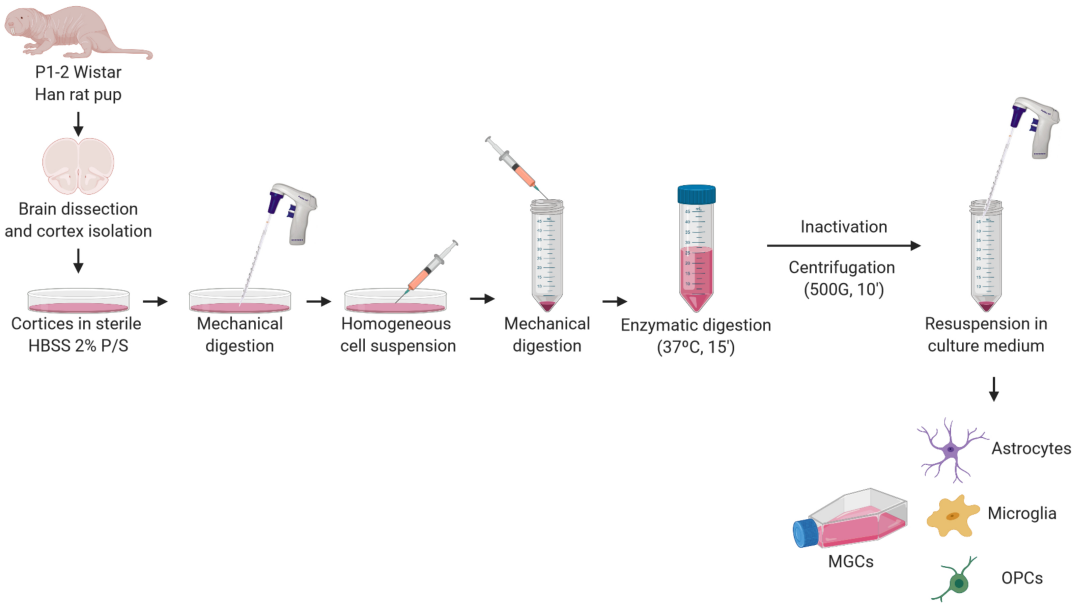


FIGURE 3.3: Schematic representation of the experimental procedure for MGCs. Only main steps indicated.

3.4.3 OPCs isolation and differentiation

OPCs were isolated from MGCs based on differential adhesion properties of the various glial cell types.

While astrocytes are strongly adherent cells, OPCs and microglia can be detached through orbital shaking. Furthermore, the adhesion/detachment process is faster for microglia than for OPCs. Based on these properties, a shake-off method has been established [127].

Around culture day 12-13, cells were confluent and the astrocytic layer was closed, indicating MGCs were ready for OPCs isolation. MGCs were submitted to a pre-shake (210 rpm, 2h, 37℃) in an Infors AG-4103 shaker, causing detachment of microglia. Medium with detached microglia was removed and culture medium was refreshed. Following a 2h incubation period (37℃, 5% CO_2), MGCs were submitted to shake-off (230 rpm, ON, 37℃), resulting in detachment of OPCs and remaining microglia (while astrocytes remain adhered during this procedure). Medium with detached OPCs and microglia was transferred to non-coated and non-treated Petri dishes (90 mm Normax) and incubated for 2h (37℃, 5% CO_2). Microglia adheres faster to non-treated substrates than OPCs, allowing for the removal of the remaining microglia. Medium with OPCs in suspension was collected from the Petri dishes and transferred to a Falcon tube through a 40 µm nylon cell strainer (Falcon 352340) to remove astrocyte clusters that could possibly have detached during shaking. After centrifuging (500 G, 10') and discarding the supernatant, the pellet was resuspended in differentiation medium (500 µL) (described in Table 3.2). Viable cells were determined using a Trypan blue exclusion test, and cell counting was performed in a Neubauer chamber and suspensions with the intended cell seeding density were prepared. For cell seeding, a 20 µL drop of cell suspension was carefully deposited on top of PLL/laminin-coated micropillars and incubated for 2h (37℃, 5% CO_2) to

allow for OPCs adhesion. After such, differentiation medium was added. Fig. 3.4 illustrates this protocol. After optimization of cell seeding density, and unless stated otherwise, experiments were performed with 20,000 cells/micropillar. For controls, 75,000 cells/well were seeded in PLL-coated (50 µg/mL, 37℃, 5% CO_2, 30') tissue culture polystyrene (TCPS) wells. Differentiation medium was refreshed every 2 days. At a defined timepoint, OPCs were fixed or lysated.

TABLE 3.2: Composition of OPC cultures' differentiation medium. Concentrations indicated in v/v are relation to the final medium volume. For components of SATO 10x, final concentrations in the differentiation medium are 1/10 of those indicated.

Components	Concentration
Differentiation medium	
DMEM Glutamax High Glucose (Gibco 31966-021)	
FBS (Gibco 10270-106), *Heat inactivated (56℃, 30')*	0.5% (v/v)
Insulin (Sigma I9278)	5 µm/mL
P/S	1% (v/v)
SATO 10x	0.1% (v/v)
SATO 10x	
DMEM Glutamax High Glucose (Gibco 31966-021)	
Transferrin (Sigma T2036)	1 mg/mL
Putrescine (Sigma P5780)	160 µg/mL
Bovine serum albumin (BSA, Biowest P6154)	1 mg/mL
Progesterone (Sigma P8783)	600 ng/mL
Sodium selenite (Sigma T1775)	400 ng/mL
Thyroxine (Sigma T1775)	400 ng/mL
Triiodo-L-thyronine (T3, Sigma T6397)	300 ng/mL

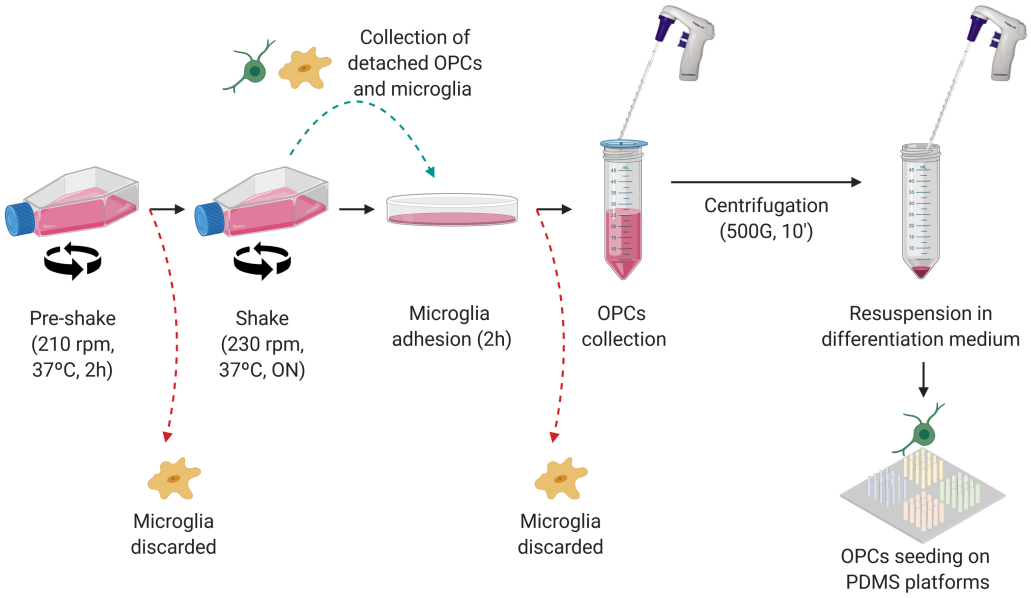


FIGURE 3.4: Schematic representation of the experimental procedure for OPC isolation and seeding on PDMS platforms. Only main steps indicated.

Isolation of OPCs was performed up to the third shake of MGCs, after which the MGCs cultures were discarded. Fig. 3.5 illustrates the timeline of both MGCs and OPC cultures.

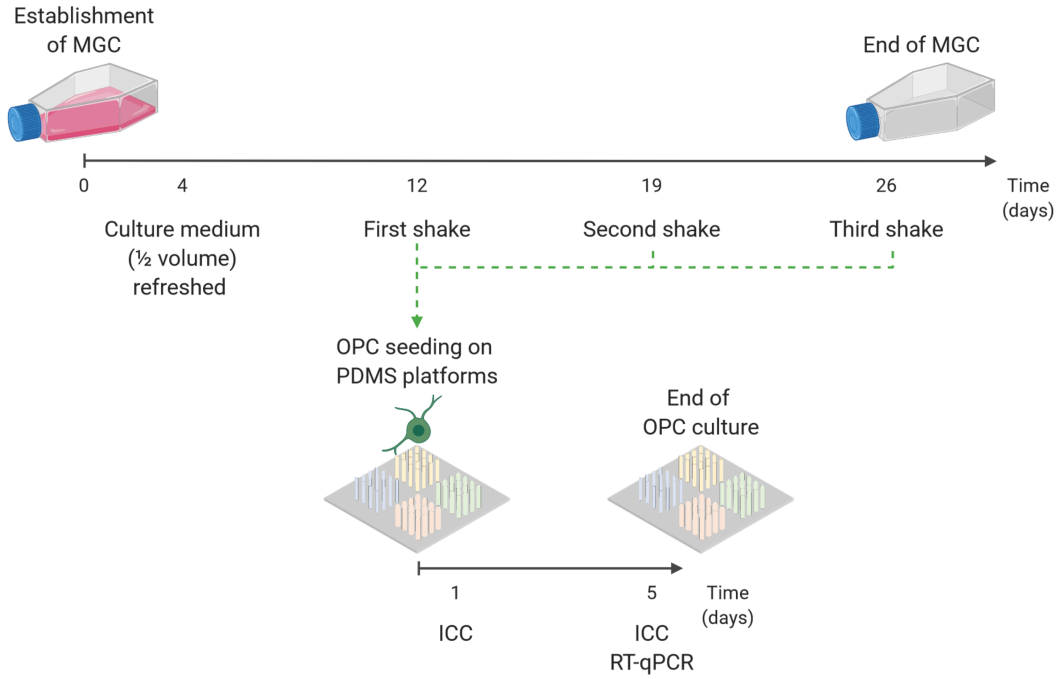


FIGURE 3.5: Timeline indicating the main timepoints in MGCs and OPCs. After day 4, culture medium in MGCs was refreshed every 2 days (not indicated). For OPC cultures, differentiation medium was refreshed on day 2 (not indicated).

3.5 Immunocytochemistry

At a defined timepoint, cells were fixed with 4% paraformaldehyde (PFA). Differentiation medium was removed, cells were washed twice with PBS (5', room temperature (RT)), fixed with 4% paraformaldehyde (PFA) (20', RT) and washed twice with PBS (5', RT). For long-term storage, samples were kept in PBS with 0.01% sodium azide at 4℃.

For immunostaining of OPCs/OLs cultures, permeabilization and blocking were performed simultaneously by incubation with 0.3% Triton X-100 and 5% normal donkey serum (NDS, Sigma D9663) in PBS (1h, RT). Primary and secondary antibodies were diluted in PBS with 0.15% Triton X-100 and 1% NDS. Samples were incubated with primary antibody solution (ON, 4℃) and washed three times with PBS (5', RT). Afterwards, samples were incubated with secondary antibody solution (1h, RT) and washed twice with PBS (5', RT). Nuclei were counterstained with Hoechst (1:1000 in PBS) (15min, RT) and washed twice with PBS (5min, RT).

Immunocytochemistry (ICC) protocols differed for each cell type and respective neural markers.

For ICC of astrocytes, permeabilization was performed by incubation with 0.3% Triton X-100 in PBS (15', RT), followed by blocking with 5% NDS in PBS (1h, RT). Primary and secondary antibodies were diluted in PBS with 0.15% Triton X-100 and 1% NDS.

For microglia and neurons, permeabilization was performed by incubation with 0.1% Triton X-100 in PBS (10', RT), followed by blocking with 5% NDS in PBS (1h, RT). Primary and secondary antibodies were diluted in PBS only. The remaining protocol, for both types of cultures, was similar to the aforementioned protocol for OPCs/OLs.

The following primary antibodies were used: rabbit anti-Olig2 (1:400, Merk Millipore AB9610), rat anti-MBP (1:100, Bio-Rad MCA409S), mouse anti-α tubulin (1:2000, Sigma T5168), rabbit anti-GFAP (1:1000, Abcam AB7260), rabbit anti-IBA1 (1:500, Wako 019-19741) and mouse anti-β III tubulin (1:500, BioLegend 801202). The following secondary antibodies were used (1:1000 dilution): Alexa-Fluor (AF) 568 anti-rabbit (Invitrogen A10042), AF 488 anti-rat (Life Technologies A21208), AF 594 anti-mouse (Invitrogen A11005), AF 488 anti-rabbit (Invitrogen A11034) and AF 488 anti-mouse (Life Technologies A21202). Table 3.3 indicates the combinations of primary and secondary antibodies used in ICCs.

TABLE 3.3: Primary and secondary antibody mixes used for ICC of different neural cell types.

Cell type	Primary Antibody	Secondary Antibody
OPCs/OLs	Rabbit anti-Olig2	AF 568 anti-rabbit
	Rat anti-MBP	AF 488 anti-rat
	Mouse anti-α tubulin	AF 594 anti-mouse
Astrocytes	Rabbit anti-GFAP	AF 488 anti-rat
Microglia and Neurons	Rabbit anti-IBA1	AF 568 anti-rabbit
	Mouse anti-βIII tubulin	AF 488 anti-mouse

Following ICC, micropillars were mounted upside-down with Mowiol in 35-mm ibidi dishes (ibidi 80136). Micropillars were left at RT overnight to allow for the mounting medium to dry.

3.6 Reverse transcriptase quantitative PCR

Cell lysis and RNA purification were performed using Quick-RNA MiniPrep (Zymo Research R1050). Briefly, for cell lysis, differentiation medium was totally removed and 20 µL of RNA Lysis Buffer were pipetted directly on top of the micropillar. These 20 µL were then collected to a RNase-free tube and stored at -80 ºC until further use. RNA purification was performed according to manufacturer's instructions. The cell lysate was thawed at RT, transferred to a Zymo-Spin™ IC Column in a collection tube and centrifuged (12000 G, 30"). An in-column DNase I treatment was performed for 15', at RT. Following this, the column was washed with RNA Prep Buffer (400 µL) and centrifuged (12000 G, 30") to recover RNA. To elute RNA, 15 µL of DNase/RNase-Free Water were pipetted to the column matrix and centrifuged (16000 G, 30"). Finally, the eluted RNA was stored at -80 ºC until further use.

Considering that RNA is very susceptible to degradation due to the ubiquity of RNases in the environment, it is critical to assess RNA quality before proceeding to qPCR, in order to avoid unnecessary downstream costs and inaccurate results. Quality assessment includes evaluation of RNA purity and integrity, as well calculation of RNA quantity.

In order to evaluate RNA purity and calculate its concentration, samples were analyzed in the NanoDrop 1000 Spectrophotometer (Thermo Fisher Scientific). Nucleic acids absorb light at 260nm, while aromatic amino acids absorb at 280nm. Therefore, the A260/A280 ratio was used to evaluate RNA purity in relation to proteins, and is typically required to be in the range 1.8-2.2 [132]. Measurements at 230nm are used to determine the amount of some common contaminants (present in RNA purification kits, for example), and the A260/A230 ratio is usually required to be at least 1.7 [132]. Using the NanoDrop 1000, for each sample, the A260/A280, A260/A230 and RNA concentration values were determined.

On the other hand, the analysis of RNA integrity was performed using Experion™ RNA StdSens Analysis Kit (Biorad, Cat. 700-7103). In this system, the sample is combined with a fluorescent dye and injected into wells of a microchip. The sample moves through a gel matrix in the microchannels and is submitted to electrophoresis. The bands are detected by fluorescence, and electropherograms and gel-like images are created for sizing and quantification. Information about RNA integrity can be obtained by intensity of the major ribossomal RNA (rRNA) bands, 28S and 18S. For mammalian rRNA, the 28S/18S rRNA ratio is used as a measurement for RNA integrity, and a 28S/18S ratio near 2 is representative of good-quality RNA [132]. Experion™ presents an RNA Quality Index (RQI) for each sample, indicating if it has good integrity and is suitable for RT-PCR. An example of and Experion™ analysis can be found in Appendix B.

After confirming RNA purity and integrity for all samples, cDNA synthesis was performed using the NZY First-Strand cDNA Synthesis Kit (NZY, MB12501), according to manufacturer's instructions. The kit includes (i) NZYRT 2x Master Mix, which contains deoxyribonucleotides triphosphate (dNTPs), $MgCl_2$, oligo$(dT)_{18}$ and random hexamers (used as primers); (ii) NZYRT Enzyme Mix, which includes the NZY Reverse Transcriptase (RNase H minus) and NZY Ribonuclease Inhibitor (to prevent RNA degredation); (iii) RNase H (from *E. coli*) to degrade RNA template in

cDNA:RNA hybrids after the first strand cDNA synthesis. cDNA was synthesized from 350 ng of RNA per sample.

For each sample, the reaction system was composed of 10 µL of NZYRT 2x Master Mix, 2 µL of NZYRT Enzyme Mix, 350 ng of sample RNA and DEPC-treated water, making up a total volume of 20 µL. These components were added and gently mixed in nuclease-free tubes. The reaction mix was incubated in a thermocycler (Biometra) according to the following program: (i) 25℃, 10'; (ii) 50℃, 30'; (iii) 85℃, 5' for inactivation of the reaction system; (iv) temperature decreased to 4℃. The samples were then chilled on ice and 1 µL of RNase H (*E. coli*) was added to each reaction tube. The tubes were again incubated in the thermal cycler (37℃, 20'). Finally, the cDNA product was stored at -20℃ until further use.

qPCR was performed to evaluate the expression of MBP (target gene), using YWHAZ as a reference gene for normalization of expression levels. YWHAZ and MBP primers (ThermoScientific) were provided by Dr. Pedro Moreno (INEB/i3S) and Dr. Joana Paes de Faria (IBMC/i3S), and sequences are specified in Table 3.4.

TABLE 3.4: MBP and YWHAZ sense and anti-sense primers' sequences.

Genes	Primer	Sequence
MBP	Sense	5' TGT CAC AAT GTT CTT GAA GAA 3'
	Anti-sense	5' GCT CCC TGC CCC AGA AGT 3'
YWHAZ	Sense	5' ACG ACG TAC TGT CTC TTT TGG 3'
	Anti-sense	5' GTA TGC TTG CTG TGA CTG GT 3'

Quantitative PCR (qPCR) was performed using SYBR Green master mix (SYBR Green Master Mix, Applied Biosystems), according to manufacturer's instructions. For each sample, the reaction system was composed of 0.25 µL of each primer (corresponding to a final concentration of 125 nM for each primer, sense and anti-sense), 10 µL of iTaq polymerase, 8.5 µL of water and 1 µL of cDNA. Reactions were performed in triplicates. The plate was incubated in CFX Biorad, according to the following program: (i) 95℃, 3' (1 cycle for activation); (ii) 95℃, 10"; (iii) 55℃, 30"; (iv) 72℃, 30" (40 amplification cycles, correspondent to these three steps); (v) 60℃, 5"; (vi) 95℃ till the end of the program.

Initially, YWHAZ and 18S were both tested as reference genes for normalization of expression. The amplification efficiency was tested for all pairs of primers. For such end, a qPCR was performed with a series of dilutions of cDNA (stock concentration, 1:10 and 1:100) and amplification cycles and standard curves were analyzed. YWHAZ was eventually selected to be used as a reference gene, while 18S was excluded (results presented in Appendix B). Data obtained in this efficiency study also allowed to determine qPCR could be performed from a 1:2 dilution of cDNA.

qPCR raw data was retrieved using Bio-Rad CFX Maestro (version 1.0, `https://www.bio-rad.com/`). Results were obtained using the ΔC_T method [133]. Briefly, the normalized gene expression of each sample was calculated as $2^(\Delta C_T)$, where ΔC_T corresponds to the difference between mean C_T values (from 3 technical replicates) of the target (MBP) and reference (YWHAZ) genes. This method assumes (i) the efficiency of amplification of both target and reference genes is near 100% and (ii)

the efficiency of amplification between target and reference genes differs less than 5%. Both conditions were verified in the efficiency tests [133].

3.7 Inverted fluorescence microscopy and confocal microscopy

Representative images of ICCs were obtained using the Confocal Microscope Leica SP5.

For image-based quantifications, imaging was performed using the INCell Analyzer 2000, an automated fluorescence widefiled microscope. For TCPS wells imaging, 25 equally-spaced fields were acquired in a 2D mode. For PDMS surface and micropillars imaging, 9 fields (3x3 grid of juxtaposed fields) were acquired per diameter, in a 2.5D mode (3 μm depth). Importantly, each diameter was manually framed in the grid and all acquired channels were manually focused.

3.8 Image segmentation and analysis

For quantification of non-oligodendroglial cells (astrocytes, microglia and neurons), images were segmented using CellProfiler (version 3.1.8, `https://cellprofiler.org/`), an open-source cell image analysis software. Classification was performed using CellProfiler Analyst (version 3.1.8, `https://cellprofiler.org/cp-analyst/`). Classification was performed using a Random Forest algorithm, with user-defined classes. At least 200 objects were included in each class, in order to create a training set. Once the accuracy of classification was above 80%, the classifier was used for bath processing. A detailed explanation of the process can be found in Chapter 4 and Appendix C.

For classification of OLs' differentiation stage, a method developed and published by Bouçanova and colleagues was adapted [134]. Images acquired in INCell Analyzer 2000 were segmented using ilastik (version 1.3.2, `https://www.ilastik.org/`), an open-source segmentation toolkit. Further image segmentation and analysis were performed using CellProfiler, and final results were analyzed using Microsoft Excel (Microsoft Office 2016). A detailed explanation of the process can be found in Chapter 4 and Appendix D.

For quantification of MBP^+ cells, MBP area and micropillars' wrapping, a new image analysis process was developed. Images acquired in INCell Analyzer 2000 were segmented using ilastik. Further image segmentation and analysis was performed using CellProfiler, and final results were analyzed using Microsoft Excel. A detailed explanation process can be found in Chapter 4 and Appendix E.

Images acquired in the Confocal SP5 and other presented images were treated using ImageJ (version 1.50b, `https://imagej.nih.gov/ij/`).

3.9 Live imaging of OPC cultures

For live imaging of OPC cultures, a mixed micropillars' platform was prepared and fixed on a 35-mm ibidi dish (ibidi 81156). After OPC seeding and adhesion for 2h, OPCs were incubated with culture medium with Sir-Actin (SC001, SpiroChrome) for 15'. Following this, medium with SiR-Actin was removed, fresh culture medium was added and imaging was initiated. Of notice, differentiation medium used in this experiment was prepared with FluoroBrite DMEM (Thermo Fisher Scientific,

A1896701), a transparent medium with low background fluorescence, instead of DMEM Glutamax High Glucose (Gibco 31966-021). The composition was similar to the described in Table 3.2, plus Glutamax (1% v/v, Gibco 35050) and Sodium Piruvate (1% v/v, Gibco 11360) Live imaging was performed using Leica DMI6000 FFW. Twenty fields were selected initially, covering representative fields throughout the mixed micropillars' area. Two channels were acquired (transmitted light and channel 647) every 15', up to a total of 48h.

3.10 Statistical analysis

Statistical analysis was performed using GraphPad Prism (version 7.00, `www.graphpad.com`). For all datasets, tests for identification of outliers and normality were performed. To identify and remove likely outliers, the Robust Regression and Outlier Removal (ROUT) method with Q=10% was used. Following this, Gaussian distributions were tested using the Shapiro-Wilk normality test (α=0.05). When all datasets followed a normal distribution, statistical differences between groups were calculated based on one-way (influence of one factor) or two-way ANOVA (influence of two factors), followed by Dunnet's or Tukey's multiple comparisons test, respectively, for multiple comparisons. In case one dataset did not follow a normal distribution, non-parametric tests were performed. Statistical differences between groups were calculated based in Kruskall-Wallis analysis, followed by Dunn's multiple comparisons test for multiple comparisons. A p-value below 0.05 was considered statistically significant and data are shown as mean $\pm$ standard deviation (SD).

Chapter 4

Results

4.1 Exploration of PDMS formulations for the production of micropillars and evaluation of mechanical properties

4.1.1 PDMS micropillars have the projected shape and dimensions, but are stiffer than brain parenchyma and axons

PDMS micropillars were produced through replica molding technique, peeled off in the presence of isopropanol and dried by critical point drying. To ensure the fabrication process was successful and micropillars had the projected dimensions, samples were analyzed using SEM (Fig. 4.1). The diameters at mid-length, base and top of the micropillars, as well as micropillars' length, were measured using lateral view images. The distance between micropillars was measured using top view images. The referred measurements were determined for 1-5 μm micropillars, as well as for mixed micropillars. Also, the real geometrical measurements were compared to the theoretical values, as presented in Table 4.1.

Micropillars presented the desired cylindrical shape and stand upright after critical point drying. Interestingly, the lateral walls were found to have an irregular surface. The real diameters (measured at mid-length) were larger than the theoretical values. It is also possible to observe that the base of the micropillars was, on average, 0.75 μm larger, while the top was 0.30 μm thinner in comparison to the midsection. Although the lowest absolute deviations occurred for 1 μm micropillars, these also corresponded to the greatest relative deviations due to the reduced diameter. While 1 μm and 2 μm micropillars have a smaller length than the theoretical one (10 μm), the remaining micropillars were longer than projected. Particularly, the thicker the micropillars, the longer they were (e.g. 5 μm were longer than 4 μm micropillars). The distance between micropillars was, on average, 6% shorter than the projected (30 μm), although practically constant among various diameters. Of notice, micropillars in platforms with mixed diameters had similar dimensions to the correspondent diameters in platforms with unique diameters.

These variations may not only be due to defects in the silica mold arising from the photolithography process, but also due to the swelling properties of PDMS [124].

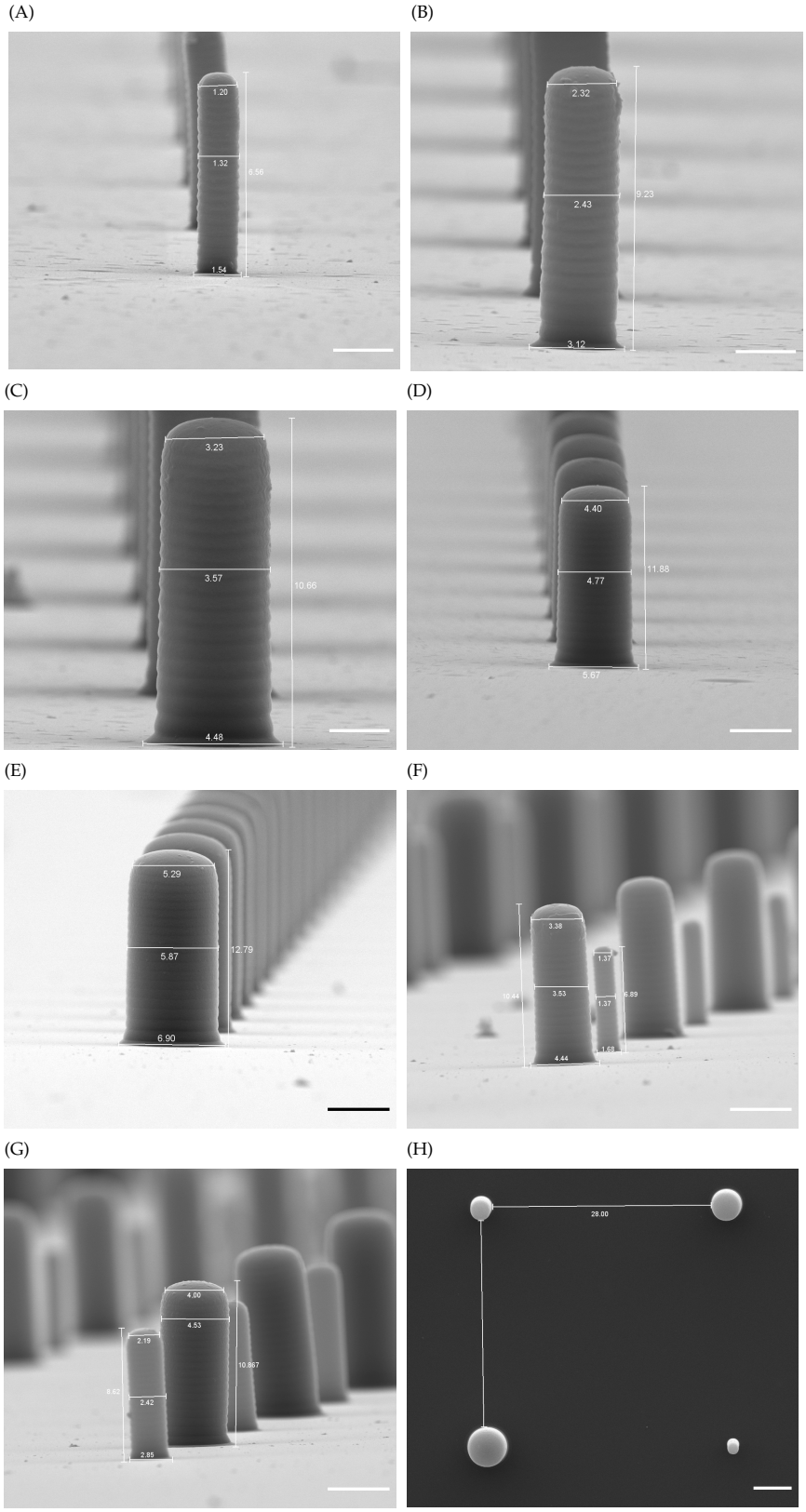


FIGURE 4.1: Representative SEM images of PDMS micropillars. (A-E) Lateral view images of 1-5 µm diameter micropillars, respectively. (F,G) Lateral view images of mixed micropillars, namely a row with alternating 1 and 3 µm diameters and a row with alternating 2 and 4 µm diameters, respectively. Lateral view images present measurements of top, mid-length, base diameters and length of micropillars. (H) Top view image of mixed micropillars, with measurements of distance between micropillars. Presented values correspond to an average of 3 measurements in the same micropillar, in a single image of each type of micropillars. n=1 independent experiment. All measurements presented in µm. Scale bars: (A-C) 2 µm; (D-G) 4 µm; (H) 5 µm.

TABLE 4.1: Measurements of diameter at mid-length, base and top of micropillars, length (from lateral view SEM images) and distance between micropillars (from top view SEM images), for PDMS micropillars. For diameter at mid-length, length and distance between micropillars, 'Diff.' represents the absolute difference between the real value and the theoretical value. 'Dev. (%)' represents the deviation in percentage of the real value from the theoretical value. 'Diff. Base-Midsection' and 'Diff. Top-Midsection' represents the absolute difference between the diameter at the base and top of the micropillar and the diameter at mid-length, respectively. Presented values correspond to an average of 3 measurements in the same micropillar, in a single image of each type of micropillars, n=1 independent experiment. All absolute measurements presented in µm.

Micropillar	Diameter at mid-length			Diameter at base		Diameter at top		Length			Distance between micropillars		
	Real value	Diff.	Dev. (%)	Real value	Diff. Base-Midsection	Real value	Diff. Top-Midsection	Real value	Diff.	Dev. (%)	Real value	Diff.	Dev. (%)
1 µm	1.32	0.32	31.83	1.54	0.22	1.21	-0.11	6.56	-3.44	-34.41	28.49	-1.51	-5.03
2 µm	2.43	0.43	21.55	3.12	0.68	2.32	-0.11	9.23	-0.77	-7.69	28.46	-1.54	-5.12
3 µm	3.57	0.57	19.12	4.48	0.90	3.23	-0.34	10.66	0.66	6.64	28.33	-1.67	-5.57
4 µm	4.77	0.77	19.37	5.67	0.89	4.40	-0.38	11.88	1.88	18.80	27.91	-2.09	-6.96
5 µm	5.87	0.87	17.42	6.90	1.03	5.29	-0.58	12.79	2.79	27.86	28.02	-1.98	-6.61
Mixed 1 µm	1.37	0.37	37.07	1.68	0.31	1.39	0.02	6.89	-3.11	-31.10			
Mixed 2 µm	2.42	0.42	20.87	2.85	0.44	2.19	-0.23	8.62	-1.38	-13.78			
Mixed 3 µm	3.53	0.53	17.79	4.44	0.91	3.34	-0.20	10.44	0.44	4.40	28.01	-1.99	-6.64
Mixed 4 µm	4.53	0.53	13.33	5.45	0.92	4.00	-0.53	10.87	0.87	8.67			

In order to evaluate the mechanical properties of the produced PDMS, 4 mm-diameter discs were produced using the same procedure as the referred PDMS micropillars and submitted to rheological tests. As reported in literature, PDMS is an elastomer, i.e. it has a viscoelastic behaviour, presenting a low Young's modulus and high failure strain in comparison to other materials [124]. PDMS discs were submitted to oscillation tests in order to determine the viscoelastic complex modulus.

Firstly, the samples were submitted to an amplitude sweep test in order to determine the LVR of the material. The LVR corresponds to a range where applied shear strains are reduced enough to maintain the material's structure intact and, therefore, the material's response is independent of the magnitude of deformation (i.e. G' and G" remain constant with increasing shear strains). After some iterations for the frequency (0.5 and 1Hz were tested, and the latter was chosen), start and end strains of the test, it was possible to conclude that the LVR was in the 0.5-20% shear strain range, corresponding to a complex shear stress in the 2-60 MPa range (Fig. 4.2).

Subsequently, oscillation tests were performed using 0.5-150% shear strain, since this range contains the LVR. The complex shear modulus (G*), as well as its elastic (G') and viscous (G") components, were determined by both amplitude sweep tests (Fig. 4.2) and frequency sweep tests (Fig. 4.3).

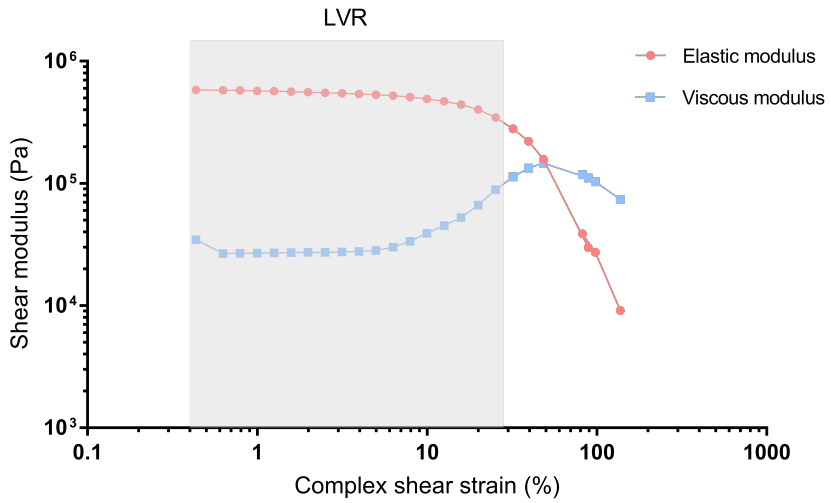


FIGURE 4.2: Representative graph of an amplitude sweep test performed in the 0.5-150% shear strain range, at 1 Hz, 10 points per decade. Determination of LVR for PDMS 4 mm-diameter discs in the 0.5-20% shear strain range.

In order to directly compare the mechanical properties of the obtained PDMS with literature values, the Young's modulus (E) was calculated from the complex shear modulus (as specified in Chapter 3). Results, determined from both amplitude and frequency sweep tests, are presented in Table 4.2.

There were no significant differences between the parameters obtained from amplitude sweep and frequency sweep tests. For discussion and further comparisons, the results from amplitude sweep tests will be used as reference values.

The relative values of the elastic and viscous modulus can be used to conclude about the viscoelastic character of PDMS discs. For both types of tests, G' was higher than G", indicating that the produced PDMS has a solid behaviour, as expected. According to calculations, the resultant G* of 433 kPa corresponds to an estimated Young's modulus of 1.3 MPa. Hence, the produced PDMS is stiffer than

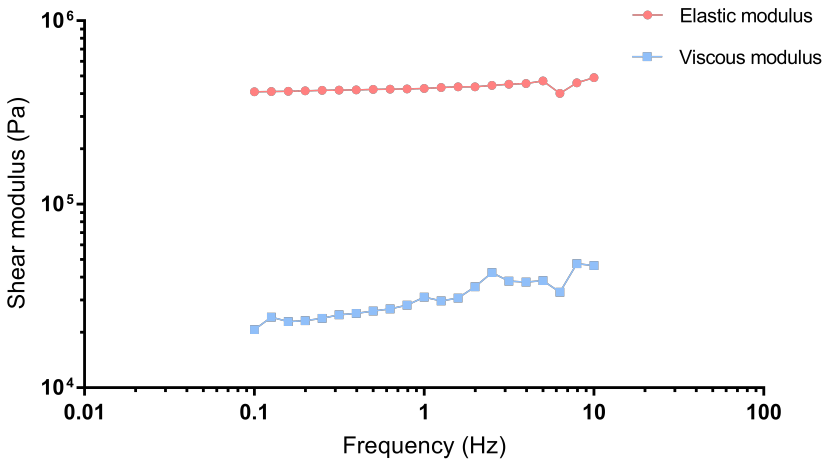


FIGURE 4.3: Representative graph of a frequency sweep test performed in the 0.1-10 Hz oscillation frequency range, at 5% shear strain, 10 points per decade.

the brain parenchyma or biological axons (considering reference values from literature [72], [116]).

TABLE 4.2: G*, G' and G" determined by amplitude and frequency sweep tests, and E calculated from the correspondent G*, for PDMS 4 mm-diameter discs. n=1 independent experiment, n=3 technical replicates per condition, for each type of oscillation test. Presented values correspond to mean±SD. All values in kPa.

		PDMS
Amplitude sweep tests	G*	433±11
	G'	432±11
	G"	28.1±1.3
Calculated E		1300±33
Frequency sweep tests	G*	416±22
	G'	415±22
	G"	26.4±1.9
Calculated E		1250±67

4.1.2 Addition of dimethicone reduces PDMS stiffness by up to 70%

In order to further approximate PDMS micropillars to biological axons, a new PDMS formulation was tested. Samples of PDMS with dimethicone in different ratios (namely 2:1 and 3:1 w/w total PDMS-to-dimethicone ratio) were produced, using the same procedure as for normal PDMS (hereon designated control PDMS). The curing time was determined to be 1h35' for the 3:1 and 1h45' for 2:1 PDMS-to-dimethicone ratio formulations.

Dimethicone consists of a siloxane - hence, it has a chemical composition similar to the PDMS base, but lower viscosity. Therefore, mixing PDMS prepolymer with dimethicone decreases the final stiffness, because of the oligomer concentration of the final mixture diminishes. In fact, combination of dimethicone with other siloxanes can be used to decrease the final material's stiffness, as previously reported [135], [136].

The viscoelastic properties of these formulations were also evaluated submitting 4 mm-diameter discs to amplitude sweep and frequency sweep tests (with the same parameters as for control PDMS discs). Similarly, E was calculated from G* using the aforementioned expression. Results are presented in Table 4.3.

TABLE 4.3: G*, G' and G" determined by amplitude and frequency sweep tests, and E calculated from the correspondent G*, PDMS 4 mm-diameter discs prepared with 3:1 and 2:1 PDMS-to-dimethicone ratio formulations. n=1 independent experiment, n=3 technical replicates per condition, for each type of oscillation test. Presented values correspond to mean±SD. All values in kPa.

		Ratio 3:1	**Ratio 2:1**
Amplitude sweep tests	G*	169±1.5	127±8.3
	G'	168±1.4	126±8.3
	G"	16.2±0.3	12.8±0.6
Calculated E		505±4.2	380±2.5
Frequency sweep tests	G*	163±4.3	121±7.4
	G'	162±4.4	120±7.4
	G"	14.9±0.3	11.7±0.9
Calculated E		489±1.3	364±2.2

The values of G' were higher than G", showing that these new formulations maintain the solid-like behaviour of PDMS.

For 3:1 PDMS-to-dimethicone ratio, G* was 168 kPa, while for 2:1 PDMS-to-dimethicone ratio, G* was 127 kPa. According to calculations, these shear moduli correspond to an E of 505 kPa and 380 kPa, respectively (Table 4.3).

In comparison to control PDMS, the addition of dimethicone to total PDMS in a ratio of 3:1 and 2:1 caused a significant reduction in shear moduli and stiffness of 60% and 70%, respectively. However, no significant differences were detected between the 3:1 PDMS and 2:1 PDMS formulations (Fig. 4.4).

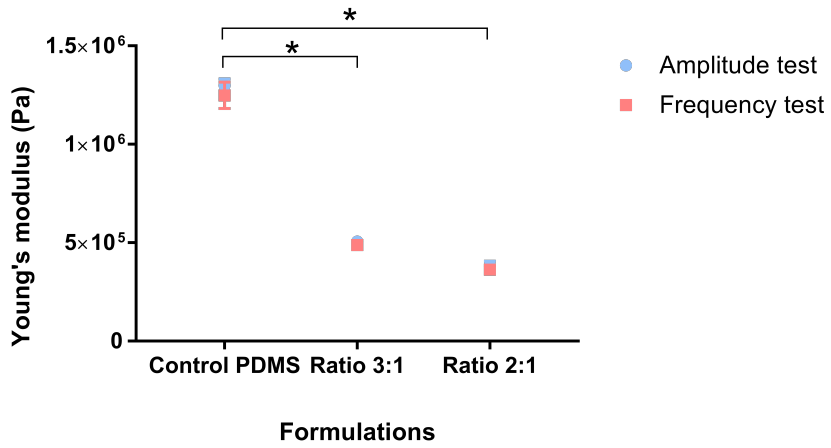


FIGURE 4.4: Comparison of E from control PDMS, 3:1 and 2:1 PDMS-to-dimethicone ratio formulations. n=1 independent experiment, n=3 technical replicates per condition, for each type of oscillation test. Presented values correspond to mean±SD. Statistical analysis performed using One-way ANOVA, * $p<0.05$

4.1.3 Micropillars produced with 2:1 PDMS-to-dimethicone ratio have similar shape and dimensions than those of control PDMS

It was possible to produce micropillars using both 3:1 and 2:1 PDMS-to-dimethicone ratio formulations. Considering that 2:1 ratio was softer (i.e. closer to biologically relevant stiffness values), this formulation was selected for further experiments. The 2:1 total PDMS-to-dimethicone formulation is hereon designated as "soft PDMS", (while PDMS without dimethicone continues to be designated as "control PDMS").

The fabrication process of soft PDMS micropillars was similar to that of control PDMS (only with a longer curing time). Notwithstanding, these softer platforms required a more careful handling to avoid damage or micropillars' collapse.

The soft PDMS micropillars were also analyzed using SEM (Fig. 4.5). Measurements were performed as previously mentioned for control PDMS micropillars. Results are presented in Table 4.4.

The mid-length diameters of soft PDMS micropillars were closer to the theoretical values than those of control PDMS micropillars. These soft PDMS micropillars were only around 0.15 µm thicker than the theoretical value. The differences between the base or top diameter and mid-length diameter were also verified. Similarly to control PDMS micropillars, thicker micropillars were also longer. However, in this case, for most diameters, micropillars were shorter than projected. Soft PDMS micropillars were closer among each other than control PDMS micropillars. Once again, micropillars in platforms with mixed diameters had similar dimensions to the correspondent diameters in platforms with unique diameters.

Considering that soft PDMS micropillars had the appropriate dimensions, these micropillars were used for further experiments to study the influence of substrate stiffness on OPC differentiation and micropillars' wrapping. Results are reported in Section 4.4.

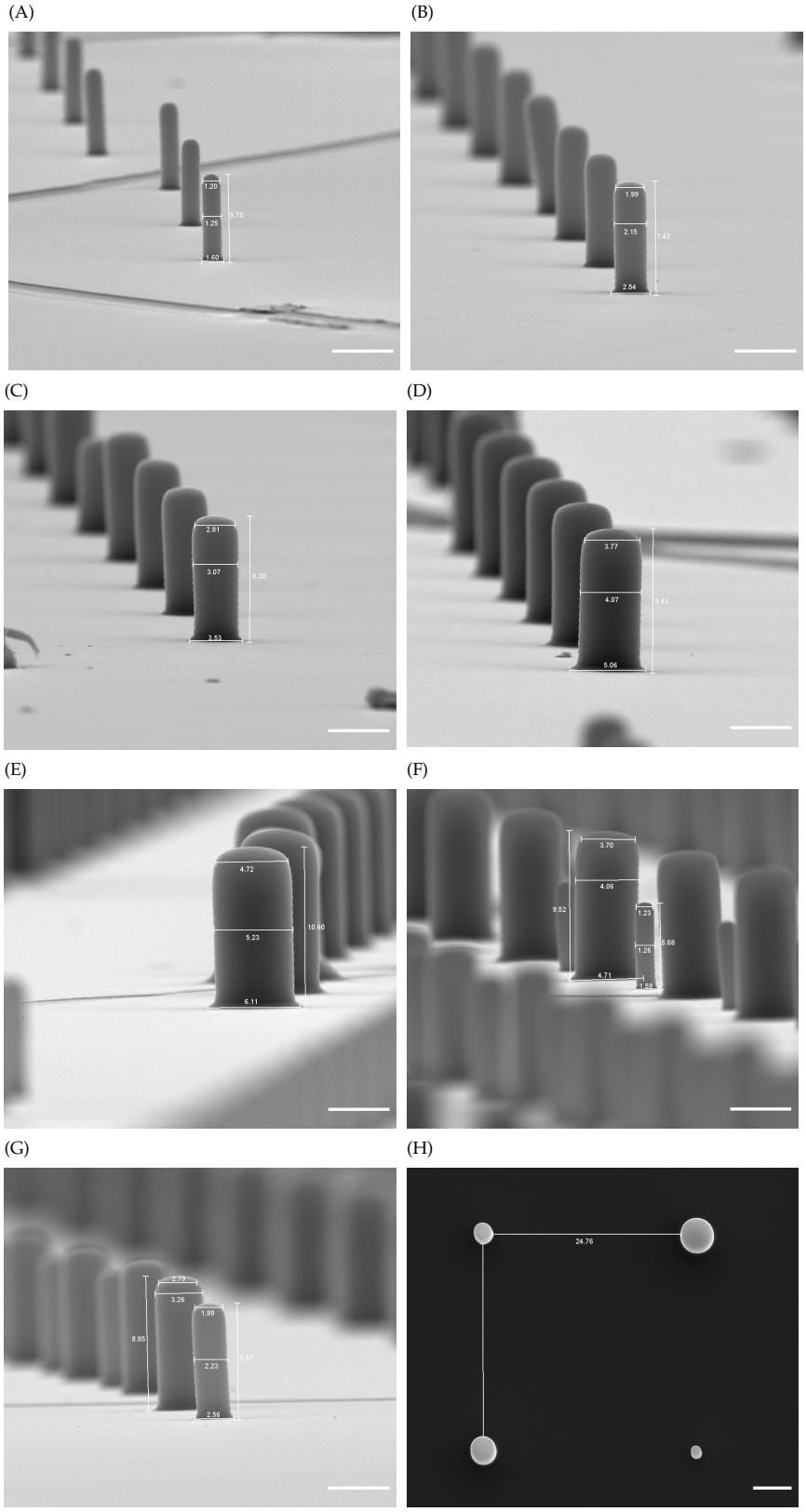


FIGURE 4.5: Representative SEM images of soft PDMS micropillars. (A-E) Lateral view images of 1-5 µm diameter micropillars, respectively. (F,G) Lateral view images of mixed micropillars, namely a row with alternating 1 and 3 µm diameters and a row with alternating 2 and 4 µm diameters, respectively. Lateral view images present measurements of top, mid-length, base diameters and length of micropillars. (H) Top view image of mixed micropillars, with measurements of distance between micropillars. Presented values correspond to an average of 3 measurements in the same micropillar, in a single image of each type of micropillars, n=1 independent experiment. All measurements presented in µm. Scale bars: (A-C) 2 µm; (D-G) 4 µm; (H) 5 µm.

TABLE 4.4: Measurements of diameter at mid-length, base and top of micropillars, length (from lateral view SEM images) and distance between micropillars (from top view SEM images), for control PDMS micropillars. For the diameter at mid-length, length and distance between micropillars, 'Diff.' represents the absolute difference between the real value and the theoretical value. 'Dev. (%)' represents the deviation in percentage of the real value from the theoretical value. 'Diff. Base-Midsection' and 'Diff. Top-Midsection' represents the absolute difference between the diameter at the base and top of the micropillar and the diameter at mid-length, respectively. Presented values correspond to an average of 3 measurements in the same micropillar, in a single image of each type of micropillars, n=1 independent experiment. All absolute measurements presented in µm.

Micropillar	Diameter at mid-length			Diameter at base		Diameter at top		Length			Distance between micropillars		
	Real value	Diff.	Dev. (%)	Real value	Diff. Base-Midsection	Real value	Diff. Top-Midsection	Real value	Diff.	Dev. (%)	Real value	Diff.	Dev. (%)
1 µm	1.25	0.25	24.70	1.60	0.36	1.20	-0.05	5.75	-4.25	-42.48	25.80	-4.20	-14.00
2 µm	2.15	0.15	7.52	2.54	0.39	1.99	-0.17	7.42	-2.58	-25.82	25.70	-4.30	-14.33
3 µm	3.07	0.07	2.21	3.53	0.46	2.81	-0.25	8.30	-1.70	-17.04	25.54	-4.46	-14.88
4 µm	4.07	0.07	1.78	5.06	0.99	3.77	-0.31	9.43	-0.57	-5.72	25.47	-4.53	-15.10
5 µm	5.23	0.23	4.61	6.11	0.88	4.72	-0.51	10.60	0.60	5.99	25.50	-4.50	-15.00
Mixed 1 µm	1.26	0.26	26.33	1.59	0.333	1.23	-0.04	5.68	-4.32	-43.32			
Mixed 2 µm	2.23	0.23	11.40	2.56	0.33	2.00	-0.23	7.57	-2.43	-24.30			
Mixed 3 µm	3.26	0.26	8.66			2.79	-0.47	8.85	-1.15	-11.54	24.77	-5.23	-17.44
Mixed 4 µm	4.06	0.06	1.42	4.71	0.66	3.70	-0.35	9.52	-0.48	-4.76			

4.2 Optimization of cell seeding density on PDMS platforms

OPC differentiation is highly influenced by cell density, as previously reported [29], [115]. Therefore, in order to ensure that OPC differentiation was correctly promoted on PDMS platforms, various cell seeding densities were tested on PLL/laminin-coated PDMS 1-4 μmicropillars.

In previous experiments, the best seeding density for PLL-coated micropillars was 1250 cells/mm^2 [137]. Considering that laminin promotes OPC adhesion and differentiation [30], [95], lower and higher seeding densities were tested. Table 4.5 presents the tested seeding densities.

TABLE 4.5: Cell seeding densities tested on PLL/laminin-coated PDMS platforms. The indicated cell number corresponds to number of viable cells (determined by trypan blue exclusion assay).

Substrate	Area (mm^2)	Cell number	Cell seeding density (cells/mm^2)
PDMS platform	36	20,000	556
		45,000	1250
		60,000	1667

OPC cultures were observed at differentiation (diff.) day 2 by optical microscopy. At diff. day 5, OPCs were fixed, stained for Olig2 and MBP and observed by confocal microscopy (Fig. 4.6).

For a seeding density of 556 cells/mm^2, OPCs are well dispersed through the PDMS platform, with little aggregation (Fig. 4.6, first column). Although there may be some cell clusters, it does not affect OPCs' process extension and morphological differentiation. Cells seeded at this density follow a normal morphological differentiation process. At diff. day 2, most cells have few (2-3), short processes. It is not possible to observe membrane sheets in the optical microscopy images. At diff. day 5, MBP staining reveals that most cells have a highly branched morphology, with primary and secondary processes. It is also possible to observe some MBP$^+$ membrane sheets.

On the other hand, for a seeding density of 1250 cells/mm^2, there is the formation of some cell clusters, from diff. day 2 up to day 5 (Fig. 4.6, second column). Although it may not be visible in optical microscopy images, confocal images reveal that OPCs in these clusters do not present the expected morphology. OLs in these clusters do not extend many processes outwards, according to MBP staining. This phenomenon is even more significant for a seeding density of 1667 cells/mm^2, where most cells are "retained" in large clusters (Fig. 4.6, last column). Additionally, it is possible to see that these cell clusters surround various micropillars, consequently impeding the observation of OPCs' interaction with these micropillars. In short, increasing seeding density causes OPC aggregation and prevents process extension and branching.

According to optical microscopy images from diff. day 2, there are no observable differences between OPCs cultured on flat PDMS and on micropillars, for any seeding density. Importantly, the formation of cell clusters with increasing seeding density is similar for OPCs cultured on flat surfaces and micropillars. This tendency is maintained throughout the culture. For diff. day 5, cell clusters remain in cultures of 1250 and 1667 cells/mm^2 seeding densities.

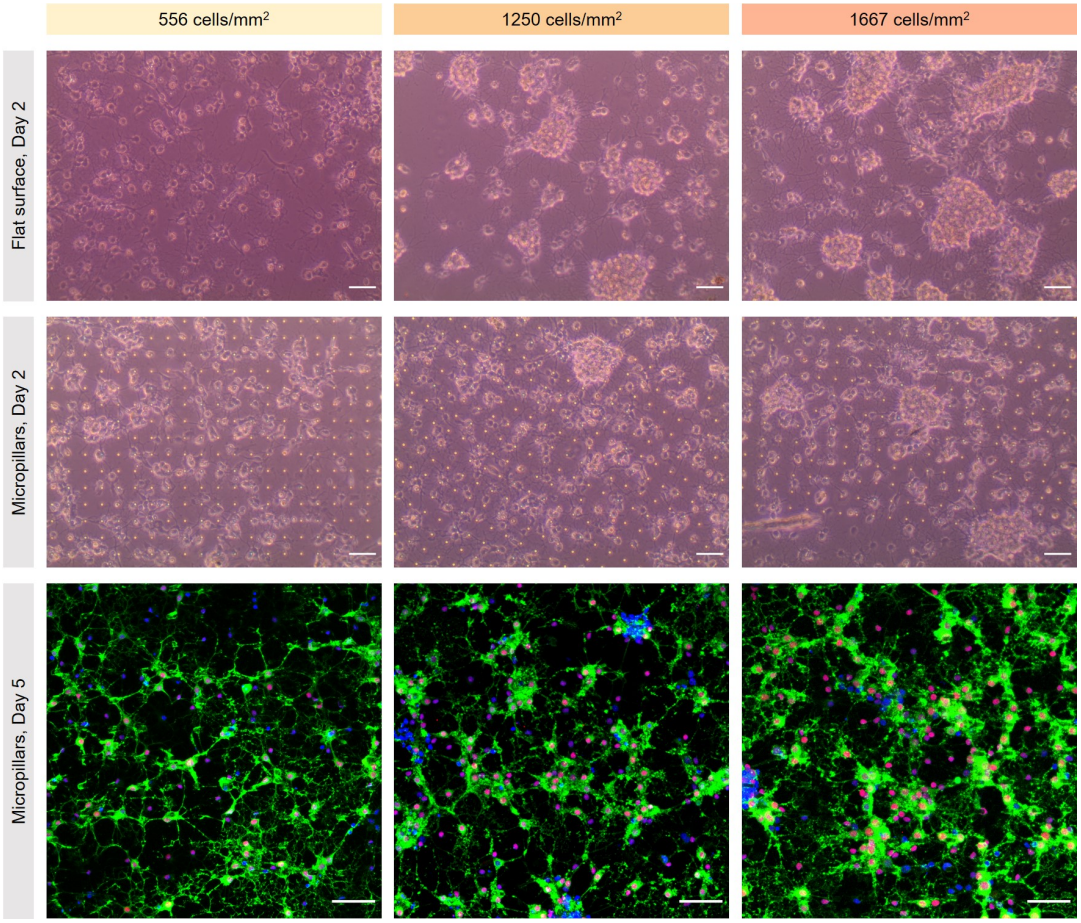


FIGURE 4.6: Representative images of OPC morphology for seeding densities of 556 cells/mm^2, 1250 cells/mm^2 and 1667 cells/mm^2. Upper rows present optical microscopy images from OPC cultures on PDMS flat surfaces and micropillars at diff. day 2. Last row presents confocal microscopy images of OPC cultures on 4 µm micropillars, at diff. day 5. ICC for Olig2 (red), MBP (green) and nuclei counterstained with Hoechst (blue). Scale bars: 50 µm.

It is also important to notice that conclusions are similar for the various diameters tested (1-4 µm). Indeed, for the lowest seeding density (556 cells/mm^2), there were also no visible differences in OPC morphology and branching at diff. day 5 between the various analyzed diameters (Fig. 4.7).

Based on these observations, cell seeding density of 556 cells/mm^2 was selected for future experiments using this micropillars' platform.

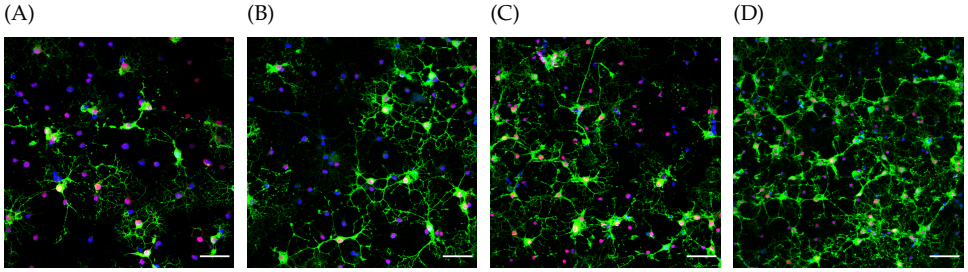


FIGURE 4.7: Representative confocal images of OPC morphology for seeding density of 556 cells/mm^2 at diff. day 5, on 1-4 µm micropillars (A-D, respectively). ICC for Olig2 (red), MBP (green) and nuclei counterstained with Hoechst (blue). Scale bars: 50 µm.

4.3 Evaluation of purity of OPC cultures

Primary MGCs were prepared from Wistar Han P1-2 cortices. It is, therefore, possible that some neuronal progenitors and immature neurons may survive in culture. Furthermore, OPCs are isolated from primary MGCs as described in Chapter 3. Considering that the isolation process is only dependent on the differential adherent properties of glial cell types under orbital shaking conditions, it is likely that some microglia and astrocytes are present in OPC cultures.

In order to evaluate the purity of OPC cultures, these cells were cultured on PDMS platforms (both 1-4 μm, 2-5 μm micropillars and flat surfaces) up to diff. days 1 and 5. Such timepoints were selected so as to assess how OPC purity evolved throughout time. At these timepoints, cultures were fixed and stained for GFAP, IBA1 and βIII tubulin – widely used markers for reactive astrocytes, microglia and neurons, respectively [138]–[140]. In particular, PDMS platforms were either stained for GFAP or co-stained for IBA1 and βIII tubulin.

INCell Analyzer 2000 was used for imaging of the stained platforms. Image segmentation was done with CellProfiler, while cell classification was performed with CellProfiler Analyst. CellProfiler is a software tool for quantifying data from biological images, with a flexible interface composed by modules set up by the user. CellProfiler Analyst is a software that allows for classification of objects of interest into one of various user-defined classes, using machine learning-based algorithms.

Briefly, the CellProfiler pipeline identifies the nuclei using the DAPI channel images, creating primary objects named “Nuc”. Through a 5 pixels-radial expansion of these objects, the pipeline creates secondary objects, denominated “NucExp”. The intensity of the GFAP signal inside the NucExp objects is measured. Following this, images are analyzed in CellProfiler Analyst. The user classifies NucExp objects as GFAP-positive or negative (at least 200 objects per class), creating a training set. An algorithm is trained in order to classify objects in one of these two classes, based on the intensity of the GFAP channel inside the NucExp objects. In order to obtain a classification accuracy of at least 80%, the training set may need to be further expanded. Once that criterion is met, the model is used to classify the NucExp objects of all images. A similar CellProfiler pipeline was used for samples co-stained for IBA1 and βIII tubulin, and NucExp objects are classified into one of three classes (IBA1 positive, βIII tubulin-positive or double negative objects) with CellProfiler Analyst. Finally, it was possible to quantify the percentage of non-oligodendroglial cells and estimate the purity of OPC cultures. The flowchart presented in Fig. 4.8 corresponds to a brief description of the image analysis process. Further explanation of the image analysis process, accompanied with an image as example, can be found in Appendix C.

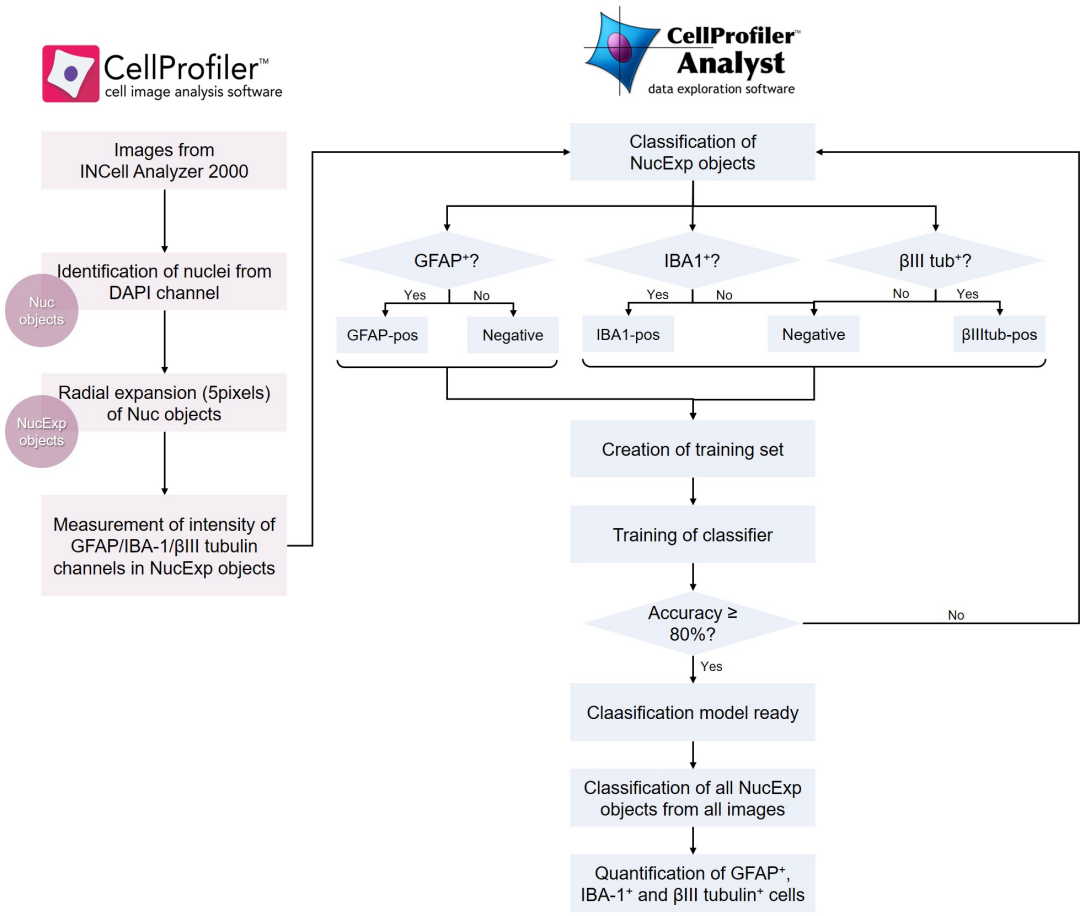


FIGURE 4.8: Flowchart of the image analysis process for evaluation of OPC cultures purity. The image analysis process includes two main steps in the referred programs: CellProfiler and CellProfiler Analyst.

4.3.1 GFAP-, IBA1- and βIII tubulin-positive cells are present in OPC cultures, decreasing OPC purity

Fig. 4.9 includes representative images of GFAP staining at both timepoints and Fig. 4.10 presents the quantification results of GFAP stainings.

The percentage of GFAP$^+$ cells in OPC cultures tends to increase from diff. day 1 to diff. day 5, for almost all types of substrates. Statistically significant differences were only verified for 2, 3 and 4 µm micropillars and TCPS, although cells cultured on 5 µm micropillars and flat surfaces appear to follow the same tendency. Overall, GFAP$^+$ cells represented around 5% of total cells in OPC cultures on diff. day 1, increasing to 11% on diff. day 5. These values were slightly lower for the TCPS control (1.8$\pm$0.8 % on day 1 and 7.5$\pm$3.6 % on day 5). Although the tendency remains for diff. day 5, no significant differences between the various types of substrates were found at this timepoint. Hence, it is possible to conclude that GFAP$^+$ astrocytes survive in OPC cultures, and cultures on PDMS substrates may promote a higher percentage of GFAP$^+$ cells (vs. TCPS). On the contrary, the presence of micropillars does not influence astrocyte survival.

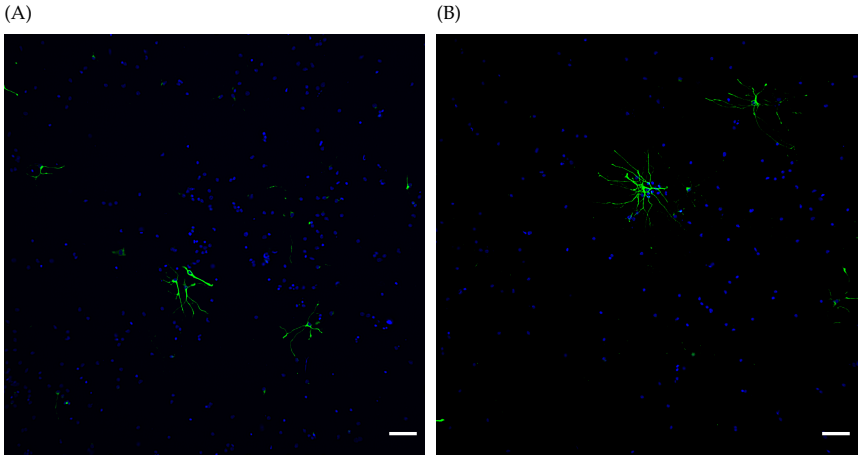


FIGURE 4.9: Representative images of GFAP$^+$ cells in OPC cultures on control PDMS micropillars at (A) diff. day 1 and (B) diff. day 5. ICC for GFAP (green) and nuclei counterstained with Hoechst (blue). Images obtained with INCell Analyzer 2000. Scale bars: 50 µm.

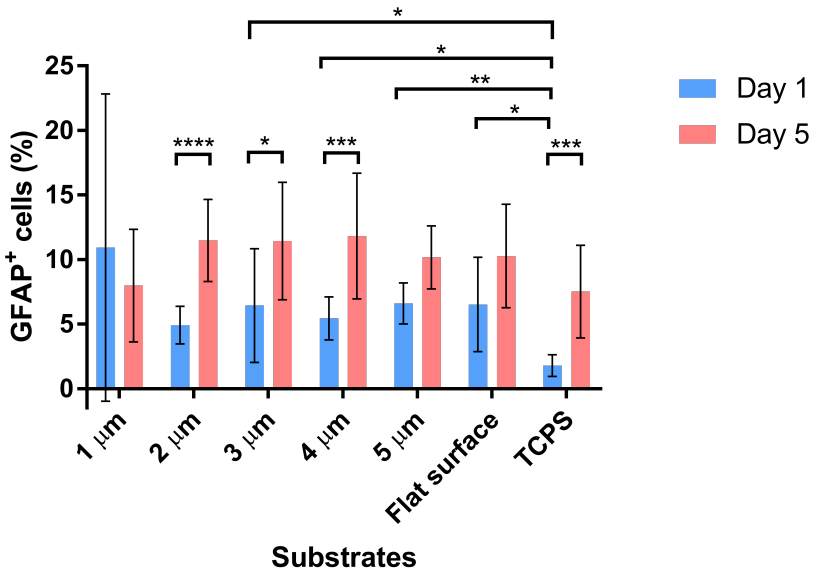


FIGURE 4.10: Quantification of GFAP$^+$ cells in OPC cultures on control PDMS platforms and TCPS wells, at diff. days 1 and 5. n=3 independent experiments, 2-4 technical replicates per diameter. Graphs present mean values with SD bars. All unique conditions followed normal distribution, except for 3 µm micropillars at diff. days 1 and 5. Statistical analysis performed using Kruskal-Wallis test, * p<0.05, ** p<0.01, *** p<0.001, **** p<0.0001

Regarding the presence of microglia, there are no clear tendencies. While for 1, 2 µm micropillars and flat surfaces, there seems to be an increase in the average percentage of IBA1$^+$ cells, for 3, 4 and 5 µm micropillars this percentage decreases from day 1 to day 5. IBA1 expression varied considerably between substrates on diff. day 5. Statistical differences were found for 3, 4 and 5 µm micropillars in comparison to flat surfaces. Microglia was not detected in TCPS controls, for any timepoint. PDMS flat surfaces seemed to allow for higher microglia survival than micropillar

substrates. Fig. 4.11 includes representative images of IBA1 and βIII tubulin staining at both timepoints and Fig. 4.12 presents the quantification results of IBA1 stainings.

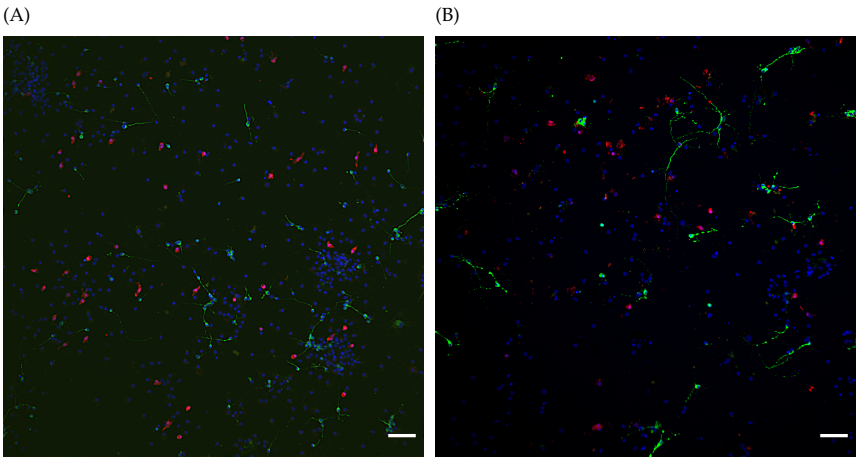


FIGURE 4.11: Representative images of IBA1$^+$ and βIII tubulin$^+$ cells in OPC cultures on control PDMS micropillars at (A) diff. day 1 and (B) diff. day 5. ICC for βIII tubulin (green), IBA1 (red) and nuclei counterstained with Hoechst (blue). Images obtained with INCell Analyzer 2000. Scale bars: 50 µm.

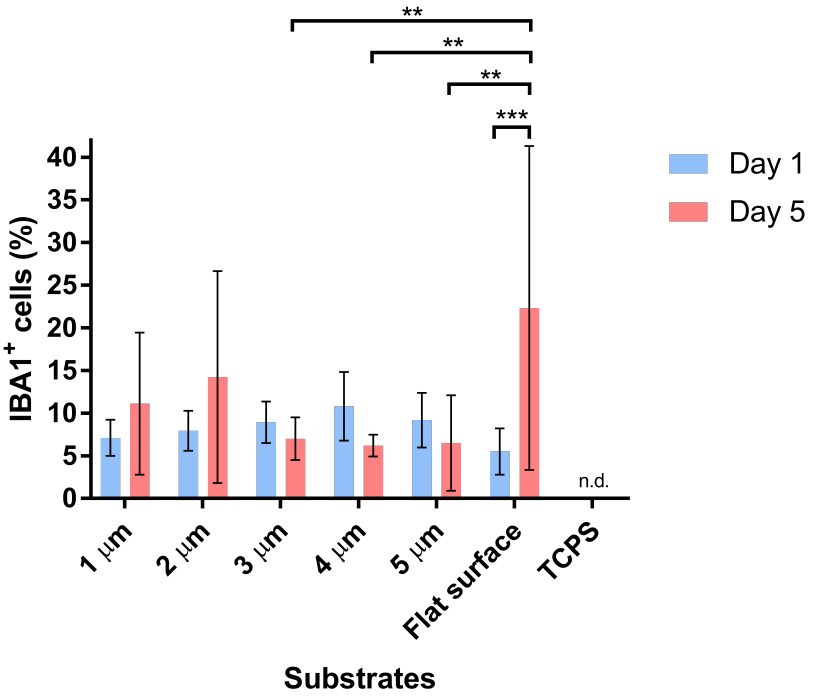


FIGURE 4.12: Quantification of IBA1$^+$ cells in OPC cultures on control PDMS platforms, at diff. days 1 and 5. IBA1$^+$ cells not detected in TCPS wells. n=3 independent experiments, 2-4 technical replicates per diameter. Graphs present mean values with SD bars. Statistical analysis performed using Two-way ANOVA, ** p<0.01, *** p<0.001

Concerning βIII tubulin-expressing cells, these were present in all types of substrates (except in TCPS). Their percentage tended to decrease from day 1 to 5 (significant differences for 3 and 4 µm micropillars). Apart from a slightly higher percentage of βIII tubulin$^+$ cells in 5 µm micropillars versus other substrates on day 5, there were no differences between substrates worth of notice at both timepoints. On diff. day 1, approximately 10% of cells in OPC cultures were positive for this neuronal marker, while on diff. day 5, the percentage decreased to around 5% (except for 5 µm micropillars). Neuronal cells were not detected in TCPS controls as well, for any timepoint. Fig. 4.11 includes representative images of IBA1 and βIII tubulin staining at both timepoints and Fig. 4.13 presents the quantification results of IBA1 stainings.

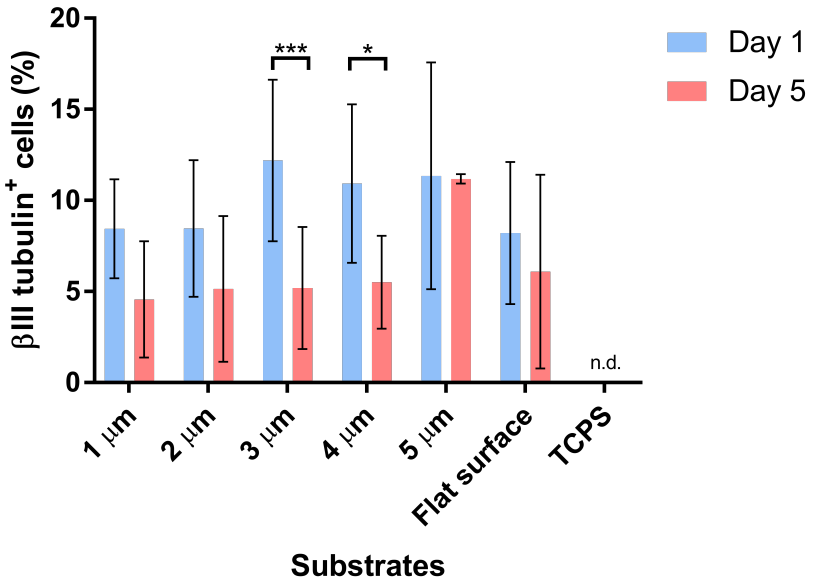


FIGURE 4.13: Quantification of βIII tubulin$^+$ cells in OPC cultures on control PDMS platforms, at diff. days 1 and 5. βIII tubulin$^+$ not detected in TCPS wells. n=3 independent experiments, 2-4 technical replicates per diameter. Graphs present mean values with SD bars. Statistical analysis performed using Two-way ANOVA, * p<0.05, *** p<0.001

Taking together the percentage of all non-oligodendroglial cells present in OPC cultures, it is possible to estimate OPC purity to be approximately 75% at diff. day 1, evolving to 72% at diff. day 5 (considering an average value of all substrates). However, there is considerable variability between substrates. While for 1, 3 and 4 µm micropillars OPC purity increased slightly between both timepoints, other substrates showed an opposite tendency. Notably, OPC purity for control substrates (flat PDMS and TCPS wells) decreased from day 1 to 5. Overall, there is an increase in GFAP$^+$ cells and decrease in βIII tubulin$^+$ cells. The presence of IBA1$^+$ cells is highly variable. Fig. 4.14 indicates the fraction of cells present in OPC cultures for diff. days 1 and 5. Tables with the average values for each unique condition, at diff. days 1 and 5, can be found in Appendix F.

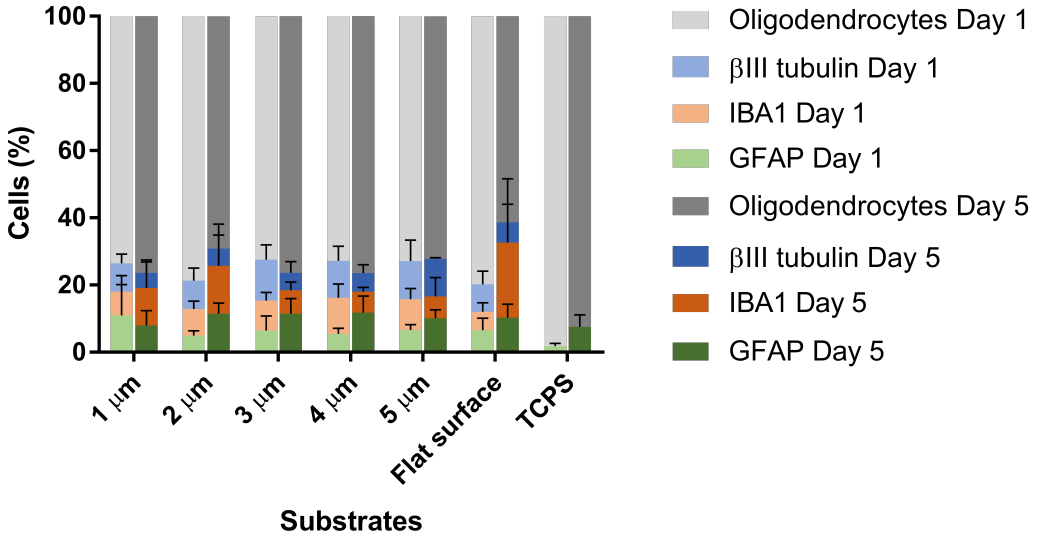


FIGURE 4.14: Estimation of OPC purity for cultures on PDMS platforms and TCPS wells at diff. days 1 and 5. Percentage of oligodendroglial cells calculated as the difference between 100% and the sum of average values for GFAP$^+$, IBA1$^+$ and βIII tubulin$^+$ cells. Graphs present mean values with SD bars. No SD bars for the oligodendroglial fraction.

These results indicate that neuronal cells were still present in MGCs. Although OPCs were carefully isolated from MGCs based on differential adherent properties, a fraction of non-oligodendroglial cells remained in culture throughout OPC differentiation. Furthermore, the use of primary cultures resulted in great variability among independent experiments.

4.4 Effect of micropillar diameter and substrate stiffness on OPC differentiation and myelination

Mechanical stimuli of various types may influence OPC differentiation, axonal wrapping and myelination (as reviewed in Chapter 1). Here, mechanical stimulus was modulated in three ways: substrate stiffness (comparing control and soft PDMS platforms), micropillars' presence (vs. PDMS flat surface) and micropillars' diameter. The influence of these mechanical stimuli was evaluated through: expression of MBP (at both the protein and gene level), cell morphology and MBP area, differentiation stage and micropillars' wrapping.

OPCs were cultured on control and soft PDMS platforms (namely 1-4 µm, 2-5 µm micropillars and flat surfaces) and stained for Olig2, MBP and α-tubulin at diff. days 1 and 5. This staining was performed so as to evaluate the antigenic differentiation of oligodendroglial cells (by the number of Olig2$^+$ and MBP$^+$ cells), as well as morphological differentiation (by observation of tubulin microtubules). Importantly, for assessment of gene expression, and due to the micropillars platform design (one platform has four areas with different diameters), it was not possible to compare the various micropillars' diameters. As a consequence of this technical obstacle, only two types of stimuli were evaluated: substrate stiffness (using control and soft PDMS

platforms) and micropillars' presence (comparing cultures on mixed micropillars and flat surfaces).

The ICCs were observed using confocal microscopy, but for high content screening (HCS) and quantification, the INCell Analyzer 2000 was used. Six channels were acquired for each field: DAPI, Olig2, MBP focused on the cell body (designated MBP wix1), MBP focused on the micropillar wraps (named MBP wix, in a different focal plane than MBP wix1), α-tubulin and brightfield – for micropillar visualization. Fig. 4.15 presents an example of all the acquired channels for a single field. Image segmentation and analysis was performed with ilastik and CellProfiler, and results were analyzed using Microsoft Excel. Ilastik is an open-source software that uses machine learning algorithms to easily and interactively segment, classify and tracks objects of interest. For this type of image segmentation, pixel classification workflows were created for different channels. Two CellProfiler pipelines for image analysis were used: the "Collar Occupancy" and the "Myelinated Micropillars" pipelines.

In order to determine the differentiation stage of OPCs cultured in various unique conditions, the CellProfiler pipeline "Collar Occupancy" (previously validated and published) was used [134]. OLs were classified in four differentiation stages: stage I corresponds to mono- or bipolar OPCs; stage II OPCs are primary branched, with 3-4 processes; stage III OLs are secondary branched, with 4-5 main processes; stage IV corresponds to fully mature, extensively branched OLs with membranous processes [141]. The OPCs' differentiation stage can be determined according to their collar occupancy. In order to understand the concept of collar occupancy, one must first define what is the collar and cellular protrusions. The collar corresponds to the region of the cell body surrounding the nucleus. Cellular protrusions are the primary and secondary branches of OPCs where microtubules are present. Protrusions inside collar correspond to primary/secondary branches inside the collar region. Thus, the collar occupancy can be defined as the percentage of collar area occupied by cellular protrusions, as specified by Equation 4.1. The higher the differentiation stage of an oligodendroglial cell, the more branched it will be and, consequently, the higher the collar occupancy for that cell. Establishing ranges of collar occupancy for each stage, it is possible to classify OLs in culture into one of the four differentiation stages previously described.

$$CollarOccupancy(\%) = \frac{Areaof ProtrusionsinCollar}{Areaof Collar} * 100 \tag{4.1}$$

Fig. 4.16 includes a schematic representation and an example of an oligodendroglial cell in each differentiation stage.

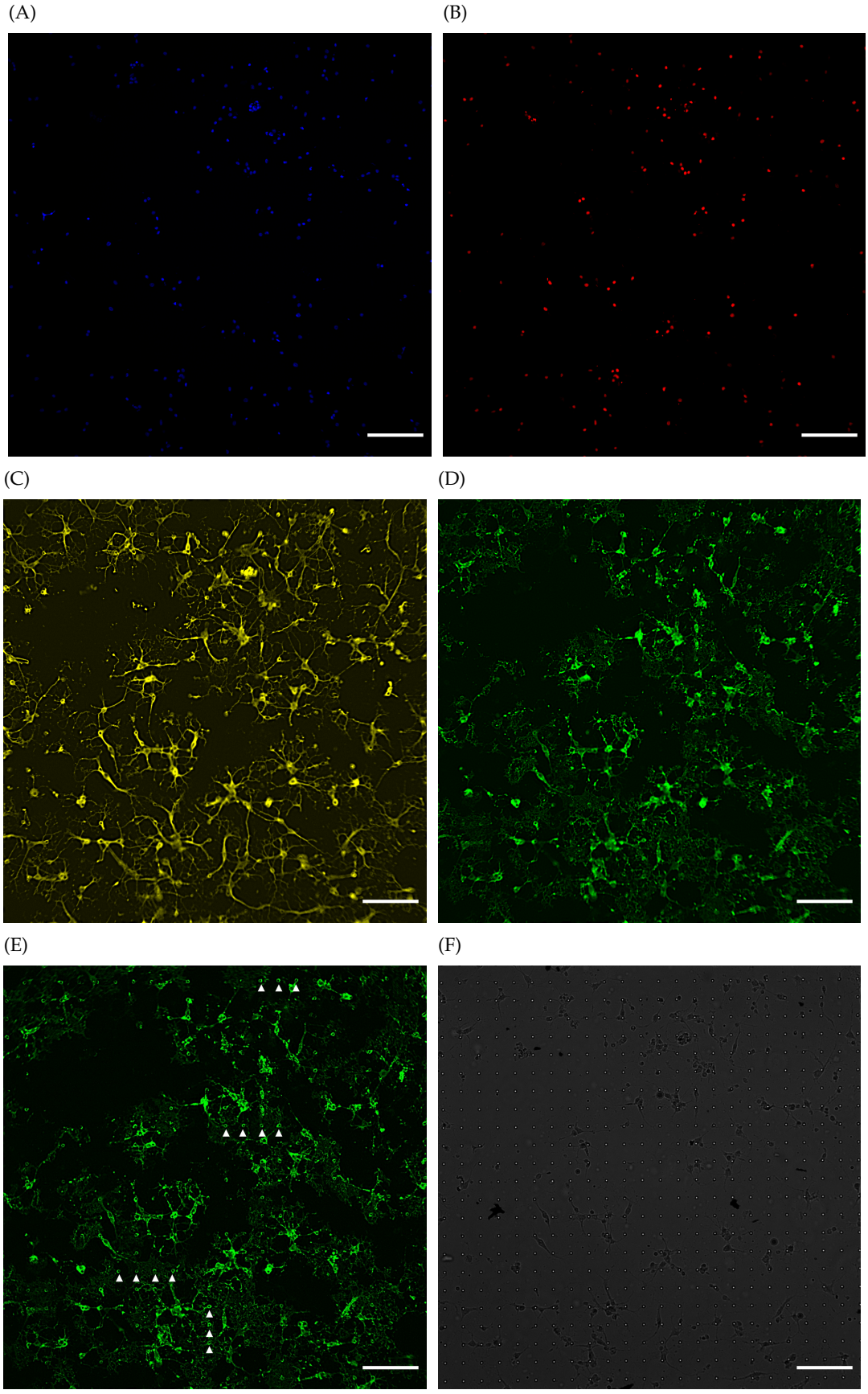


FIGURE 4.15: Representative images of acquired channels in INCell Analyzer 2000 for OPC cultures in 4 µm micropillars at diff. day 5. (A) Nuclei counterstained with Hoechst, (B) Olig2, (C) α-tubulin, (D) MBP wix1 (focused on cell bodies), (E) MBP wix2 (focuse on myelin wrapping pillars) and (F) brightfield (indicating micropillars). Arrowheads indicate myelin rings around micropillars as evidenced by the MBP wix2 channel. Scale bars: 100 µm.

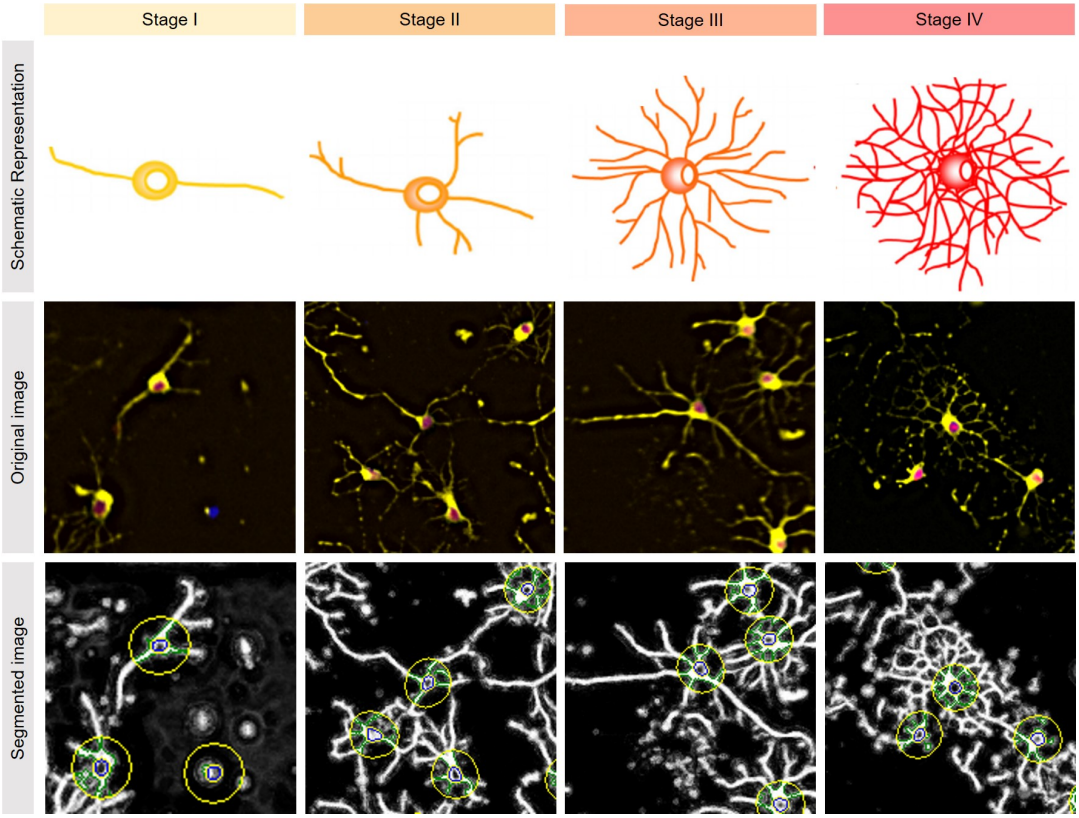


FIGURE 4.16: Representative examples of oligodendroglial cells in differentiation stages I-IV, including a schematic representation, original images and ilastik-segmented images. Stage I: mono- or bipolar OPCs (collar occupancy of example: 22.6%); Stage II: OPCs with 3-4 primary processes (collar occupancy of example: 26.6%); Stage III: OPCs with 4-5 main processes, secondary branched (collar occupancy of example: 38.9%); Stage IV: fully mature, extensively branched OL with membranous processes (collar occupancy of example: 52.2%). Schematic representation cells adapted from [141]. Original images correspond to ICC for Olig2 (red), α-tubulin (yellow) and nuclei counterstained with Hoechst. Ilastik-segmented images with indications of collar area (outlined in yellow) and cellular processes inside the collar (outlined in green).

Briefly explaining the image analysis process, the α-tubulin images were segmented using ilastik. Together with DAPI and Olig2 channels, they were used as input images for the "Collar Occupancy" pipeline. The CellProfiler pipeline first identifies the nuclei using the DAPI channel images, creating primary objects named "Nuc". Through a 12-pixels radial expansion of these objects, the pipeline creates secondary objects, denominated "NucExp". Removing the Nuc objects to the NucExp objects, tertiary objects named "Collar" are created. Next, the program uses the ilastik-segmented α-tubulin images to create other primary objects, "Cell network", measuring their area. Using a minimum area value, the program filters these objects in order to remove some debris, creating "Filtered Cell network" objects. The pipeline proceeds to mask the Filtered Cell network objects using the Collar objects, therefore obtaining exclusively the "Protrusions in Collar" objects. Finally, the program measures the area of the Nuc, Collar and Protrusions in Collar objects, as well as the intensity of the Olig2 in the Nuc objects. All these measurements are exported to a spreadsheet. Identification of Olig2$^+$, well segmented cells and their differentiation stage is performed using Microsoft Excel. The flowchart presented in Fig. 4.17 corresponds to a brief description of the image analysis process of the "Collar Occupancy" pipeline. Further explanation, accompanied with an image as

example, can be found in Appendix D.

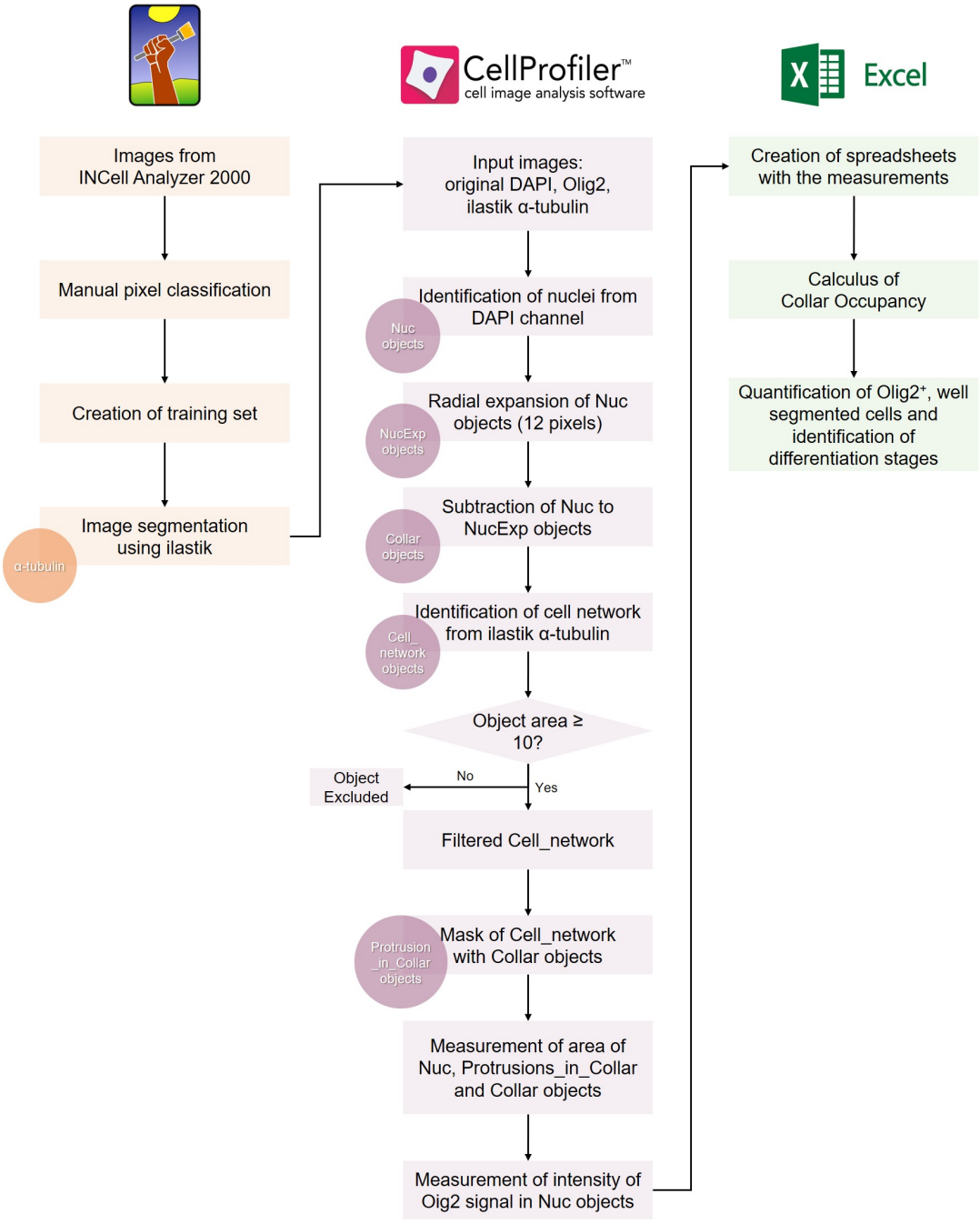


FIGURE 4.17: Flowchart of the image analysis process for evaluation of OLs differentiation stage ("Collar Occupancy" pipeline). The image analysis process includes three main steps, in the referred programs: ilastik, CellProfiler and Microsoft Excel.

Furthermore, the OLs' biological response to each unique condition was also evaluated through MBP expression, MBP area and micropillars wrapping. For that aim, the "Myelinated Micropillars" pipeline was developed. Initially, the MBP wix1, MBP wix2 and Brightfield images were segmented using ilastik, to create clearer, more defined images. Together with the original MBP wix1 and wix2 images, DAPI and Olig2 images, these were used as input for the CellProfiler pipeline, developed in the context of this project.

This pipeline starts by identifying Nuc and NucExp objects and measuring the intensity of the Olig2 and MBP wix1 signals in these objects, as previously mentioned for other pipelines. Following this, the pipeline identifies the MBP wix1 as primary objects, designated "MBPinFocus", and measures the intensity of the original MBP wix1 image inside these objects, as well as their area. This first part of the pipeline allows the user to identify Olig2$^+$, MBP$^+$ cells and the MBP area. The second part of the pipeline is dedicated to the identification of wrapped micropillars. Firstly, the program identifies micropillars as primary objects from the ilastik-segmented brightfield image ("Pillars" objects). Through a 2-pixels radial expansion, secondary objects denominated "PillarsExp" are created. The pipeline filters the PillarsExp objects with a minimum area of 25 and minimum form factor of 0.7 – in order to remove unwanted pixels that were mistakenly identified as micropillars. The output objects are called "FinalPillars". The next step is to identify the MBP wrapping around micropillars. For that, and using the ilastik-segmented MBP wix2 image, the pipeline creates the "MBPpillars" primary objects. Using a mask of the FinalPillars on these MBPpillars objects, it is possible to obtain the MBP wix2 objects that are inside the micropillars area only. Finally, it is possible to relate the FinalPillars with the MBPinPillars objects, identifying which FinalPillars present an MBP signal, i.e., which micropillars are wrapped. All these measurements are exported to a spreadsheet. Identification of Olig2$^+$, MBP$^+$ cells, MBP area and wrapped micropillars is performed using Microsoft Excel.The flowchart presented in Fig. 4.18 corresponds to a brief description of the image analysis process of the "Myelinated Micropillars" pipeline. Further explanation, accompanied with an image as example, can be found in Appendix E.

In short, the output measures used to compare the various conditions are:

1. Percentage of MBP$^+$ cells;
2. MBP area per MBP$^+$ cell;
3. Percentage of Olig2$^+$ cells in a differentiation stage I-IV;
4. Percentage of wrapped micropillars;
5. Number of wrapped micropillars per MBP$^+$ cell.

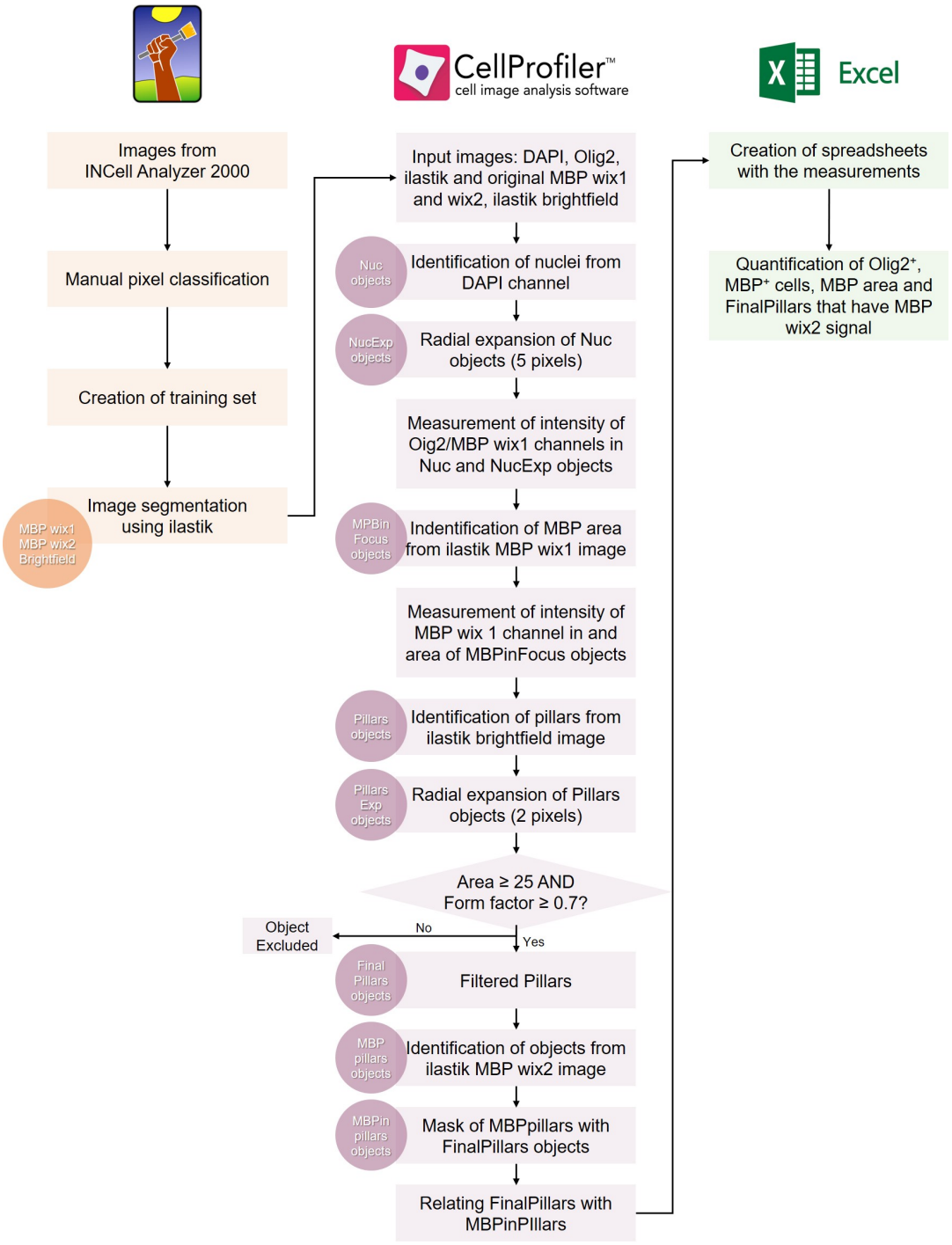


FIGURE 4.18: Flowchart of the image analysis process for Evaluation of OL myelin area and micropillars' wrapping ("Myelinated micropillars" pipeline). The image analysis process includes three main steps, in the referred programs: ilastik, CellProfiler and Microsoft Excel.

4.4.1 OPCs cultured on softer substrates and flat surfaces seems to differentiate more up to differentiation day 1

On diff. day 1, most OPCs are MBP^- (only around 10% of $Olig2^+$ cells expressed MBP) and present a 2-3 main processes. Fig. 4.19 includes representative images for flat and micropillars' platforms at diff. day 1.

At this timepoint, although the average percentage of MBP^+ cells was slightly higher for PDMS flat surfaces in comparison to TCPS, the latter has a great SD. Also, no significant differences between control and soft PDMS were found for any type of substrates, so it is not possible to draw conclusions about the influence of substrate stiffness on this parameter. The percentage of MBP^+ cells remains similar for all micropillars in comparison to control PDMS flat surfaces, except for 1 μm, where a decrease was verified. Significant differences were detected between 1 and 5 μm micropillars of soft PDMS (Fig. 4.20(A)).

Cells cultured on TCPS appear to be have a larger MBP area versus those cultured on PDMS flat surfaces. No particular differences or tendencies were verified between control and soft PDMS platforms. Regarding the influence of micropillars, cells cultured on 1 and 2 μm micropillars present a slightly higher MBP area (Fig. 4.20(B)). Also, MBP area per cell tends to be slightly higher for cultures on micropillars than on flat surfaces of the same PDMS formulation.

Regarding the differentiation stage, at diff. day 1, most cells were on diff. stage II and III, while only a small percentage was at stage IV (Fig. 4.20(C-F)). Each differentiation stage was treated as an independent output for statistical analysis. There seems to be no particular relationship between the physical stimulus of micropillars and the percentage of cells on stage I (although control PDMS 3 μm micropillars present a higher percentage of stage I OPCs). On the other hand, the percentage of stage I cells tends to be higher for control PDMS than soft PDMS substrates (although not as clearly for 5 μm micropillars and flat surfaces). Regarding stage II, there are no differences between unique conditions to be noticed. On the contrary, the percentage of cells on stage III tends to be higher for soft PDMS than for control PDMS substrates. The same tendency was observed for differentiation stage 4 (except for 1 μm micropillars and flat surfaces, although the associated SDs are large).

Finally, considering micropillar wrapping, only around 6% of micropillars are wrapped at this early timepoint, corresponding to an average of 1.5-2 micropillars per MBP^+ cell (Fig. 4.20(G,H)). There are no differences between control and soft PDMS worth of notice. In spite of the large SDs associated, a slight tendency is observable in the percentage of myelinated micropillars – this percentage tends to be higher for thicker micropillars (Fig. 4.20(G)). This tendency is more clearly observed soft PDMS, where significant differences were detected comparing 3, 4, 5 μm to 1 μm micropillars (Fig. 4.20(H)).

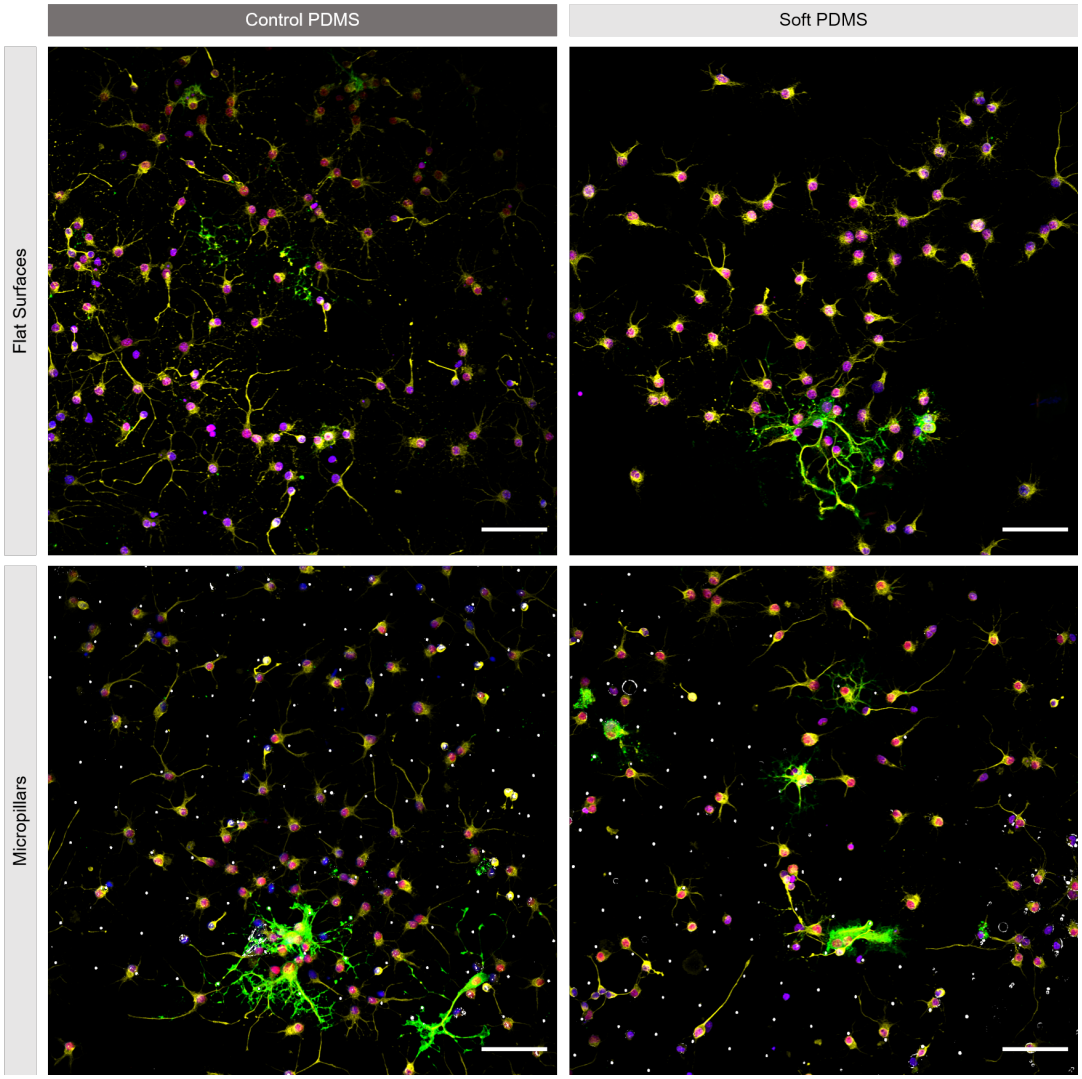


FIGURE 4.19: Representative images of OPC cultures on control and soft PDMS platforms (flat surfaces and micropillars) at diff. day 1. ICC for Olig2 (red), α-tubulin (yellow), MBP (green), nuclei counterstained with Hoechst (blue) and micropillars visible in brightfield. Scale bars: 50 µm.

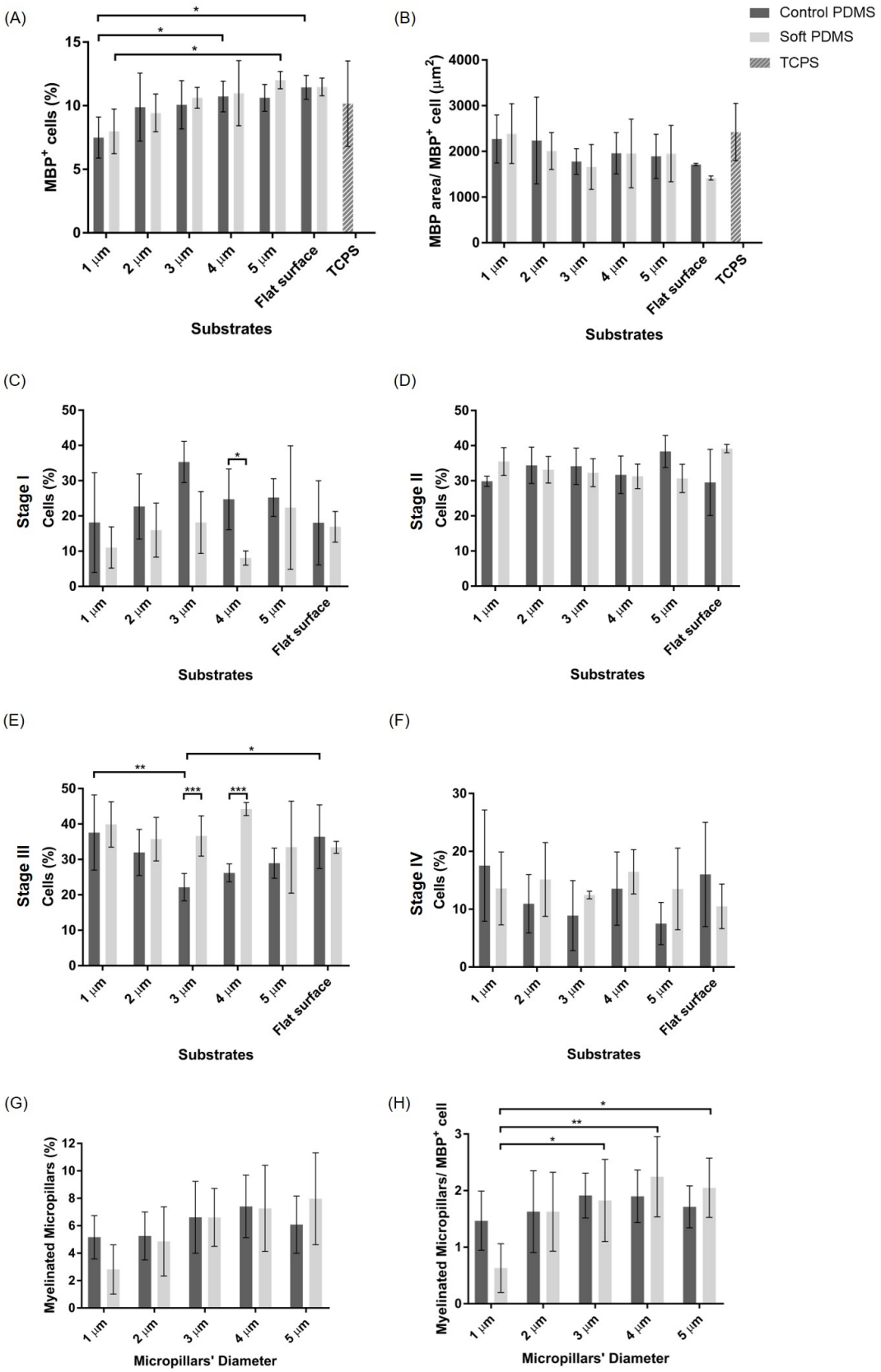


FIGURE 4.20: Quantification of differentiation and micropillars' wrapping in OPC cultures on control and soft PDMS platforms at diff. day 1. (A) Percentage of MBP^+ cells (calculated from $Olig2^+$ cells); (B) MBP area per MBP^+ cell (μm^2); (C-F) Percentage of cells at differentiation stages I-IV, respectively (calculated from $Olig2^+$ cells); (G) Percentage of myelinated micropillars; (H) Number of myelinated micropillars per MBP^+ cell. For all graphs, dark grey bars refer to control PDMS, light grey bars refer to soft PDMS and patterned bars refer to TCPS. n=2 independent experiments, 2-4 technical replicates per diameter. Graphs present mean values with SD bars. Statistical analysis performed using Two-way ANOVA, * $p<0.05$, ** $p<0.01$, *** $p<0.001$.

4.4.2 Lower substrate stiffness and micropillars with larger diameters seem to promote OPC differentiation and myelination

Oligodendroglial cells differentiated significantly from day 1 to 5 (Fig. 4.21). The percentage of MBP^+ cells increased to around 50-60% at diff. day 5. There are no coherent differences between PDMS flat surfaces and TCPS control. Although, in general, the average percentage for soft PDMS platforms tends to be slightly higher than that of control PDMS platforms, no accurate conclusions can be drawn due to the large SDs. The average percentage of MBP^+ cells appears to be higher for control PDMS micropillar platforms versus flat surfaces, particularly for thicker micropillars (for example, 5 μm micropillars). However, this tendency is not verified for soft PDMS platforms (Fig. 4.22(A)).

Regarding the MBP area per cell, there are no evident tendencies between TCPS, control and soft PDMS platforms. It appears that the MBP area is slightly lower for thick micropillars in comparison to flat surfaces of the same PDMS formulation. For control PDMS platforms, the MBP area tends to decrease with increasing diameters (despite the large SDs associated). Soft PDMS platforms do not follow the same trend, however (Fig. 4.22(B)).

Differentiation of oligodendroglial cells is also evident in terms of morphology. At diff. day 5, it is possible to observe that the fraction of cells at stage III is larger than those at stages I and II (Fig. 4.22(C-F)). The percentage of cells on stage I is tendentially higher for control PDMS substrates in comparison to soft PDMS substrates (and significant differences are even verified for 1 and 2 μm micropillars). The percentage of stage I cells appears to be higher for micropillar platforms than flat surfaces, and particularly for thinner diameters of control PDMS. However, statistical significance was not verified. The aforementioned tendencies are also observed for cells on differentiation stage II. On the other hand, there appears to be a slightly higher percentage of cells at stage III for soft PDMS substrates than for control PDMS substrates. There are no apparent differences between the various type of substrates for each PDMS formulation. The percentage of cells on stage IV is also higher for soft PDMS than control PDMS micropillars. The percentage of cells in stage IV seems to be higher for cultures on control PDMS micropillars with a larger diameter (in comparison to thinner diameters).

Micropillars' wrapping increased significantly from day 1 to 5. Indeed, at this timepoint, around 20-35% of micropillars were myelinated, and one MBP^+ cell myelinated around 3-4 micropillars (Fig. 4.22(G,H)). No visible differences were detected between soft and control PDMS micropillars, for each diameter. For control PDMS platforms, the average percentage of myelinated micropillars tended to increase with increasing diameters.

Additionally, at this timepoint, MBP expression at the gene level was evaluated through RT-qPCR.

Initially, both 18S and YWHAZ were evaluated to be used as reference genes. To be considered reference genes, their expression should not vary between conditions [142]. Variations of almost 4 CTs were verified between unique conditions for 18S, resulting in the exclusion of this gene as a reference gene (previously reported to have a variable expression in oligodendrocytes [143]). Variations in YWHAZ expression were also verified, but were not as great (maximum of 1.3 CTs). YWHAZ expression occurred at high CT values (around 25-26 CTs), which was not expected. Although these conditions were not ideal, YWHAZ was used as a reference gene for the evaluation of MBP expression.

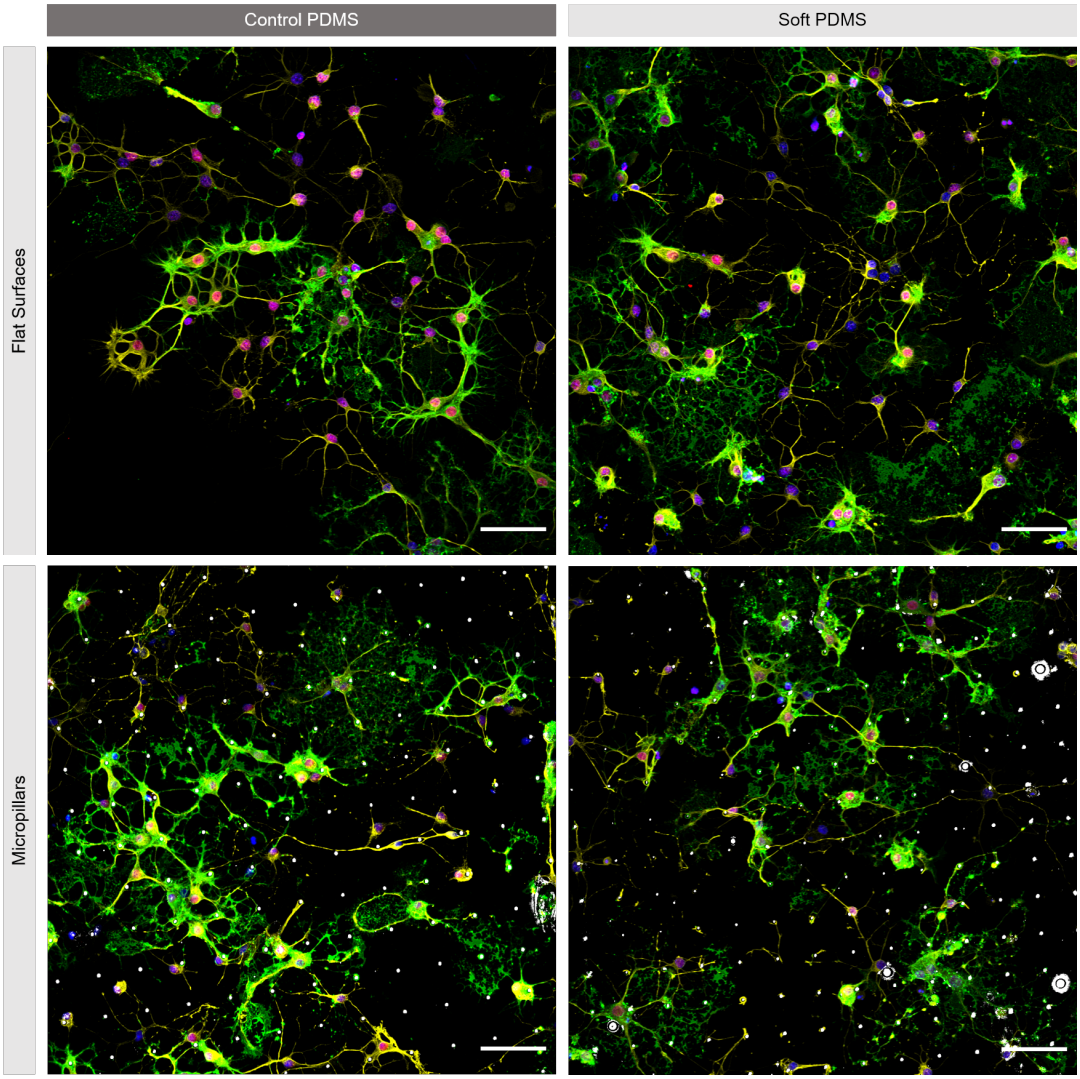


FIGURE 4.21: Representative images of OPC cultures on control and soft PDMS platforms (flat surfaces and micropillars) at diff. day 5. ICC for Olig2 (red), α-tubulin (yellow), MBP (green), nuclei counterstained with Hoechst (blue) and micropillars visible in brightfield. Scale bars: 50 µm.

For analysis purposes, independent experiments are presented separately in order to more easily identify tendencies between conditions (Fig. 4.23). MBP expression levels differed considerably between biological replicates, particularly for OLs cultured on micropillars (Fig. 4.23). In particular, MBP expression levels were lower for OPCs cultured on PDMS platforms than those cultured on TCPS (control). OPC culture on micropillars appeared to promote MBP expression in comparison to a flat surface of the same PDMS formulation. On the other hand, the influence of stiffness was not clear. For micropillars, it seems that variation of stiffness did not visibly affect MBP expression levels. However, for flat surfaces, MBP expression appeared to be slightly lower in soft PDMS than control PDMS.

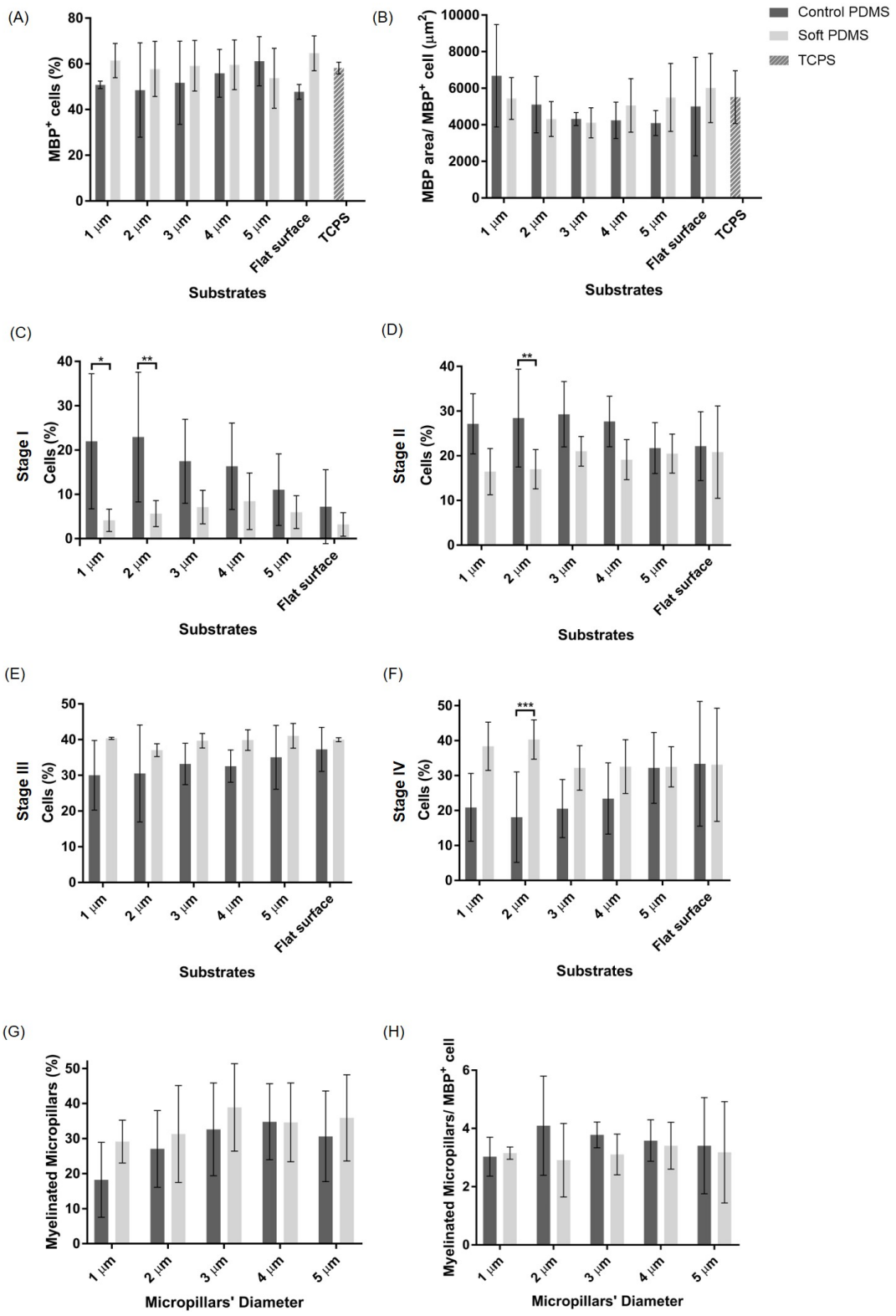


FIGURE 4.22: Quantification of differentiation and micropillars' wrapping in OPC cultures on control and soft PDMS platforms at diff. day 5. (A) Percentage of MBP^+ cells (calculated from $Olig2^+$ cells); (B) MBP area per MBP^+ cell (μm^2); (C-F) Percentage of cells at differentiation stages I-IV, respectively (calculated from $Olig2^+$ cells); (G) Percentage of myelinated micropillars; (H) Number of myelinated micropillars per MBP^+ cell. For all graphs, dark grey bars refer to control PDMS, light grey bars refer to soft PDMS and patterned bars refer to TCPS. n=2 independent experiments, 2-4 technical replicates per diameter. Graphs present mean values with SD bars. Statistical analysis performed using Two-way ANOVA, * $p<0.05$, ** $p<0.01$.

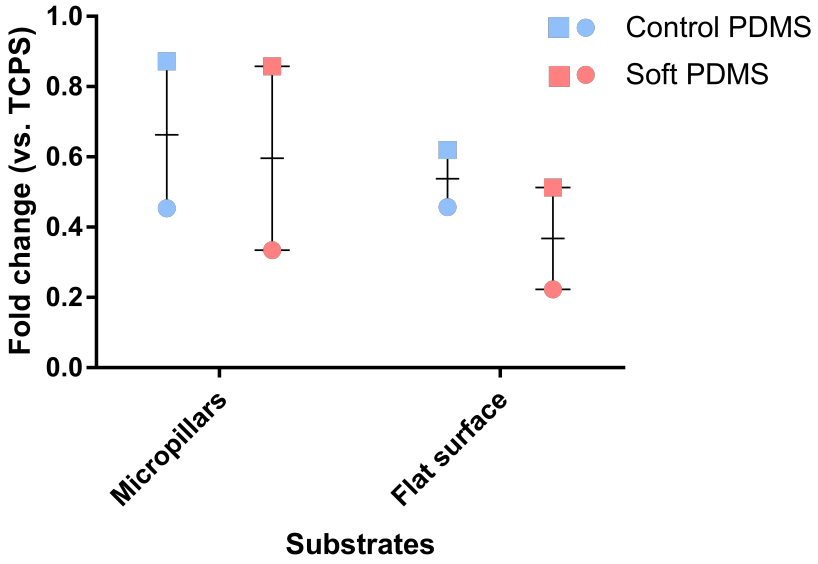


FIGURE 4.23: Quantification of MBP gene expression levels in OPC cultures on control and soft PDMS platforms at diff. day 5. Fold change of MBP expression levels in OPC cultures on PDMS platforms versus TCPS wells (calibrator sample). MBP levels normalized relatively to YWHAZ expression levels (reference gene). Blue symbols refer to control PDMS substrates, red symbols refer to soft PDMS substrates. n=2 independent experiments. Square symbols refer to first independent experiment, circle symbol refers to second independent experiment. The mid line represents the mean value.

For most of the enumerated outputs, a statistically significant difference between days 1 and 5 was found for almost all types of substrates, for both stiffnesses (Appendix G).

MBP expression and MBP area per cell increased significantly from day 1 to 5, as expected. This antigenic differentiation was accompanied by a morphological differentiation as well: it is possible to observe a decrease of cells on stage I and II, as well as a great increase of the fraction of cells on stage IV. On the contrary, the percentage of cells on stage III did not present much variation. Micropillars' wrapping, as expected, also increased significantly between both timepoints. Of notice, more statistically significant differences between both timepoints were verified for soft PDMS platforms.

A closer look at the structure of the oligodendrocytes at diff. day 5 reveals that these cells can develop large membranous structures, myelinating potentially up to 5 micropillars per cell. Also, the tubulin network does not cover the entire MBP area. In fact, tubulin is present in the main processes, but is absent from secondary processes and membranous structures (Fig. 4.24). Through a z-stack, it is possible to observe the myelin wrapping around the micropillars along their length (Fig. 4.25). The myelin wraps registered had approximately 6 µm in length.

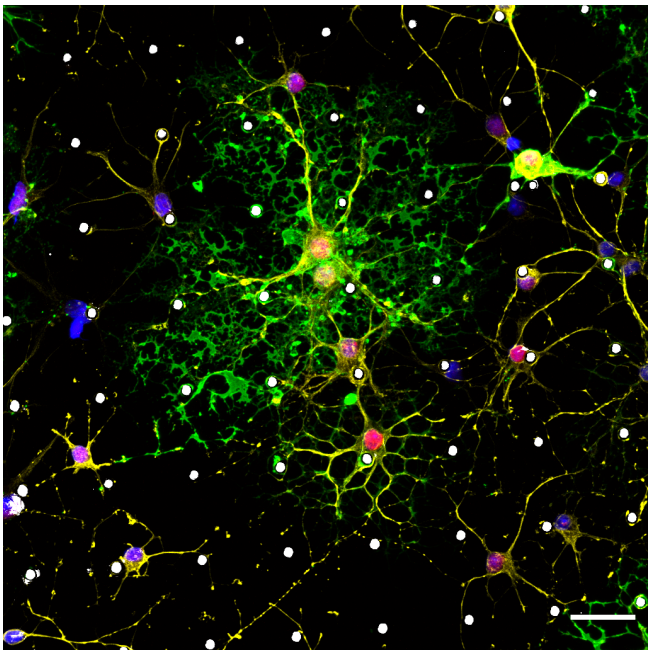


FIGURE 4.24: Representative confocal images of mature, myelinating OL on control PDMS micropillars (4 µm), at diff. day 5. ICC for Olig2 (red), α-tubulin (yellow), MBP (green), nuclei counterstained with Hoechst (blue) and micropillars visible in brightfield. Scale bar: 25 µm.

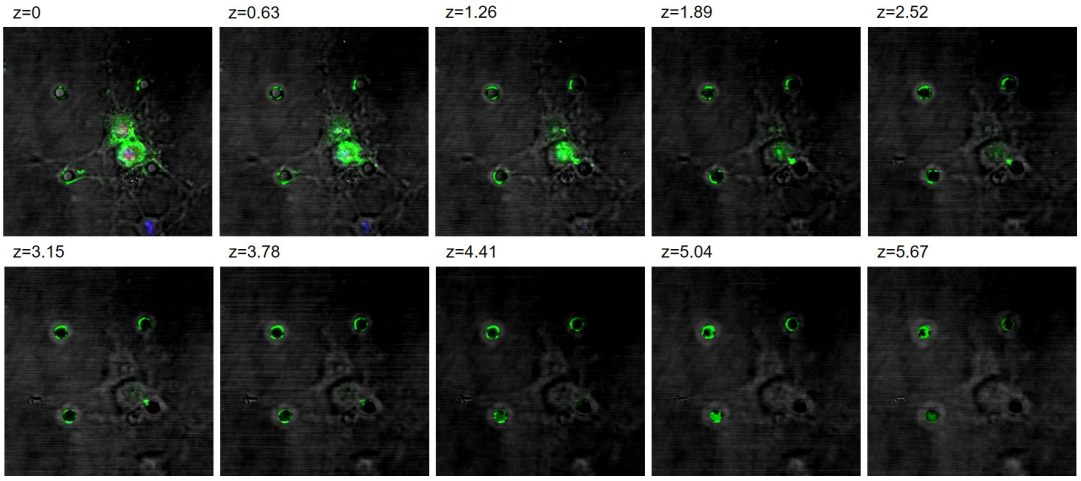


FIGURE 4.25: Representative confocal image (zoomed area from Fig. 4.24) of myelin rings wrapping around micropillars. Myelin ring from mature, myelinating OL on control PDMS micropillars (4 µm), at diff. day 5. ICC for Olig2 (red), MBP (green), nuclei counterstained with Hoechst (blue) and micropillars visible in brightfield. Absolute z-plane values indicated in µm, in a bottom to top direction. Z-step size: 0.21 µm.

4.5 Live imaging of OPC differentiation and micropillars' wrapping

Live imaging of OPCs cultured on micropillars is an important approach to more easily observe and understand OPCs' behavior when cultured on a substrate that provides different mechanical and physical cues. OPCs were seeded on mixed micropillars and live imaging was performed for the first 2 differentiation days (Fig. 4.26). A SiR-actin staining was tested, but the labelling of F-actin did not occur as expected. The staining was blurred and many cells were not stained. Therefore, this staining was not considered in the analysis.

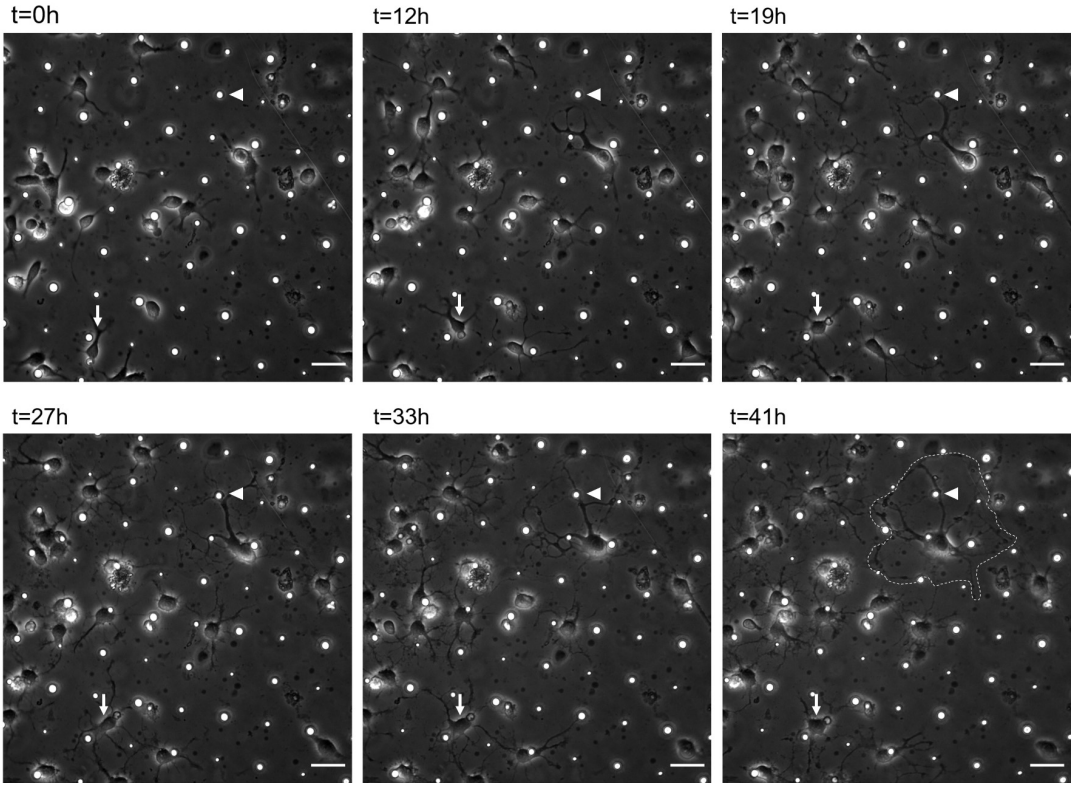


FIGURE 4.26: Representative field of live imaging of OPCs seeded on mixed micropillars for approximately two diff. days. Absolute timepoints indicated in hours. Arrowhead indicates myelinated micropillar. Arrows indicate cell with decreasing motility. Dashed line in last frame indicates cell area of a mature OL. Scale bars: 25 μm.

Initially, OPCs were mainly uni- or bipolar, presenting a round-shaped cell body. While they remain in differentiation stage I and II, these cells present some motility. The main processes are initially short, but highly dynamic. OPCs' processes extend and retract repeatedly, surveying the substrate. Of notice, since cells are cultured in differentiation medium (OL-SATO), it is not possible to observe cell division.

On the first day, OPCs rapidly extend 2-3 main processes, transitioning to differentiation stage II and III. Although no staining was performed, one could hypothesize that these main processes are mainly constituted by tubulin microtubules. As differentiation proceeds, OPCs' area and morphological complexity increases, while their motility decreases. Following this, it is possible to observe branching – small protrusions are formed throughout the primary processes, extending, enlarging and eventually forming secondary processes. Despite the lack of staining, presumably

these protrusions are formed by actin polymerization. The secondary branches may later be invaded by tubulin filaments. OPCs slightly evolve to pre-myelinating OLs.

Although the number of myelinated pillars at these early timepoints is very reduced, there are some OPCs' processes surrounding and wrapping around micropillars. It is difficult to observe this phenomenon in these images due to light dispersion around the micropillars. Nonetheless, some main processes are observed surrounding micropillars and, possibly, wrapping them. Cell bodies may also become adjacent to micropillars and surround the same with cell membrane.

By the end of diff. day 2, many cells have already differentiated up to stages II and III. There are also some mature OLs at differentiation stage IV, with a secondarily branched morphology and extensive membrane area (yet, the number of cells in this stage is reduced).

Chapter 5

Discussion

This project shows the implementation of a micropillars' platform to observe oligodendroglial cells' response to a biologically relevant environment. As previously reviewed in Chapter 1, not many studies using axon surrogates as a tool to study OLs' biology have been published. In comparison to the previous approaches, this new platform comprises different characteristics that bring the *in vitro* environment closer to the *in vivo* scenario: low substrate stiffness, presence of axon surrogates, biologically relevant axon diameters and the possibility of surface functionalization with ligands that represent homeostatic or pathological conditions. Furthermore, other features represent a technical upgrade from previously developed platforms: design of axon surrogates as aligned, unsupported, upright and high AR micropillars and detection of micropillars wrapping through top-view imaging. The previously used structures were mainly fibers, frequently produced with materials much stiffer than axons [26], [102]–[104]. On the other hand, Mei an co-workers developed the first micropillar array using silica – although it was a high-throughput platform, the micropillars neither had a biologically relevant shape nor stiffness [105]. Espinosa-Hoyos et al. developed a micropillars platform with very soft materials, but the diameters used were much larger than the typically myelinated axons *in vivo* [106].

In addition to producing these PDMS micropillars platform, it was also possible to decrease the PDMS stiffness using dimethicone from the initial 1.3 MPa to 380 kPa (approximately a 70% reduction). More importantly, micropillars were produced with this soft PDMS formulation, maintaining the shape and high AR of the structures. Thinner soft PDMS micropillars were shorter in comparison to both projected values and control PDMS micropillars, perhaps due to a slight deformation caused by their lower stiffness. Notwithstanding, the obtained diameters were close to the theoretical values and high AR values were maintained. Another interesting point is that, as revealed by SEM images, micropillars' lateral walls present a slightly irregular surface. Such feature may be advantageous, because micropillars may replicate the irregular membrane surface of axons (since these also do not have perfectly falt membranes).

Despite this alteration, the soft PDMS platforms are still stiffer than the *in vivo* counterparts. Considering the design of the micropillars' platform, the cell body of a seeded OPC remains in the spaces between the micropillars, while their processes establish contact and wrap around those structures. The flat areas that are in contact with cell bodies mimic the brain's ECM, while micropillars wrapped by OL's processes mimic axons. Therefore, PDMS stiffness should be compared to the stiffness of both brain parenchyma and CNS axons. The Young's elastic modulus of brain parenchyma is 0.1-1 kPa [72], considerably lower than the obtained soft PDMS. Considering the mechanical properties in bulk, soft PDMS is also stiffer than axons (3.7-12.86 kPa) [116], although the difference is not as great.

It is also important to highlight that the Young's modulus of PDMS membranes changes from a bulk behavior to a dimension-dependent behavior for thicknesses below 200 μm [144]. Such variation should be taken into account in this system, considering the dimensions of the PDMS micropillars. Rheology is a useful technique to study the mechanical properties of bulk samples. However, to determine the Young's elastic modulus of PDMS micropillars, AFM-enabled nanoindentation would have been a more adequate technique (as previously done in other studies with fibers [106]). Nonetheless, it is relevant to emphasize that performing nanoindentation would be technically difficult for greatly inter-spaced, thin structures as micropillars.

In addition to mechanical properties of the substrate, OPC differentiation is also highly influenced by cell density [115]. The cell seeding density used in all experiments was 556 cells/mm^2, as initially optimized for PLL/laminin-coated platforms (Section 4.2). Laminin is known to play a relevant role in OLs biology, signaling through integrin receptors and promoting OPC differentiation and branching [30], [87]. Coating PDMS platforms with laminin-211 promotes OPCs adhesion and differentiation, although no experiments were performed to study this effect. It is possible that this cell seeding density is not appropriate if other types of coating or surface functionalization are performed.

Optimization of seeding density is important not only for biological aspects, but also for technical reasons. Automated image analysis requires images with distinguishable individual nuclei or cells (depending on the purpose and method of analysis). Therefore, one must guarantee that cells are not too confluent. The image analysis that was performed required information from the nucleus and the peripheric region – up to a distance of 12 pixels (see the CellProfiler pipelines described in Appendixes D and E). For such end, the optimized cell seeding density was appropriate, since nuclei and peripherical regions were individualized. However, the outer regions of OLs membranes frequently overlapped. For other analysis methods that require information from the entire cell area (e.g. Scholl analysis), cells should be considerably separated to avoid overlapped cytoplasmic regions and/or processes. Therefore, depending also on the selected method for (semi-)automated image analysis, seeding density may need to be optimized.

On the contrary, the optimized cell density may hamper the application of other techniques, such as qPCR. It had been previously determined in the group that 300,000 OPCs per unique condition were necessary to collect enough RNA for analysis of gene expression [137]. Considering the optimized seeding density, it was necessary to prepare 16 platforms per unique condition, for each independent experiment. The design of the silica wafer (which included only 12 platforms of mixed micropillars) and the capacity of the critical point drying equipment (18 samples) constituted the limiting steps in the preparation of the platforms. For future experiments, the minimum number of cells for a particular technique/output may be reduced, in order to maintain the optimized seeding density and facilitate these experiments.

Considering the selected method for OPC isolation, it was particularly important to estimate OPC purity obtained in this system. The quantification of non-oligodendroglial cell types revealed great variability between biological replicates, as suggested by the large SD bards for almost all unique conditions. This variability can be caused by various aspects. Firstly, primary cultures are typically associated with less reproducible results (even though closer to the biological environment). Secondly, the isolation protocol relies only on the adhesion properties of each cell

type, which involve weak forces between cells and substrate. Therefore, the non-oligodendroglial cell fraction may vary from experiment to experiment. Furthermore, the image analysis process may also have some associated errors. In fact, the accuracy of the GFAP classifier was 85%, while the accuracy of IBA1 and βIII tubulin was 83%. Thus, there is a small percentage for which the classification may not be correct, so there may be some false negatives and false positives. The accumulation of all these sources of variability results in the large SDs observed in the results.

Analyzing the isolation protocol, it is possible to identify some steps that mainly contribute to the presence of other glial cell types in OPC cultures. Astrocytes form an underlying layer in MGCs. However, if they are not confluent and the layer is not closed, it is possible that some of these cells detach during the shake-off. On the other hand, microglia could come from a slow pre-shake or an incorrect handling during microglia adhesion in untreated Petri dishes. Regarding βIII tubulin$^+$ cells, they probably correspond to neuronal progenitors of rat cortices that survive in MGCs and in OPC cultures.

While astrocytes were detected in both TCPS controls and PDMS platforms, microglia and neurons were only detected in PDMS platforms. Therefore, the presence of non-oligodendroglial cell types in PDMS substrates could be due to proliferation of these cells in PDMS or due to experimental errors. Indeed, PDMS platforms and TCPS controls varied in one very important aspect: the laminin coating (performed after PLL coating in PDMS platforms, but not in TCPS). Similarly to OLs, laminin is also reported to promote adhesion of astrocytes and neural progenitors [145], [146]. As for microglia, studies have reported that these cells only "weakly adhere" to laminin substrates [147], but that this ECM molecule also exerts an effect on microglia morphology and function [148]. Thus, laminin coating likely plays a role in the differences registered between these substrates. Over days of culturing, the presence of micropillars seems to promote survival of astrocytes and neuronal progenitors, but not microglia. Importantly, no diameter seems to promote survival of non-oligodendroglial cell types in particular. For future experiments, it is important to always maintain TCPS and PDMS flat surfaces as controls. OPC culture on PLL/laminin-coated TCPS wells should also be considered as a condition for future studies.

Various studies have previously reported crosstalk between these various cell types [52], so these results suggest caution. The observed effects in experiments using this system could either be a result of mechanical cues and/or biochemical cues from the crosstalk between these different cell types. Maintaining the reported protocol, some parameters (e.g. incubation times, shaking speed) may be optimized in order to increase OPC purity. A purity threshold could be defined and only experiments with a purity above this threshold would be considered. An alternative strategy would be to include other techniques for OPC isolation based on the expression of specific markers, i.e. immunopanning or FACS [126]. Of notice, FACS would imply submitting cells to significant shear stress, which could mechanically influence OPCs biology, so immunopanning would be a more attractive alternative.

The antigenic and morphological differentiation of oligodendroglial cells occurred as expected from day 1 to 5: there was a significant increase in the percentage of MBP$^+$ cells, MBP area occupied per cell, percentage of cells in differentiation stage IV and percentage of wrapped micropillars, for all unique conditions. However, the tendencies verified between all unique conditions were not the same for all outputs. As a consequence, it is difficult to conclude about an optimal substrate to promote OPC differentiation and micropillars' myelination.

Regarding the influence of substrate stiffness, there are contradictory variations. Throughout time, soft PDMS substrates appear to promote antigenic and morphological differentiation better than control PDMS substrates. This is supported not only by greater differences between both timepoints, but also by higher values of percentage of MBP^+ cells, MBP area and cells on differentiation stage IV for soft PDMS substrates. However, results at the gene expression level show opposite tendencies. Culture on softer substrates appeared to decrease MBP gene expression. The differences between results at the protein and gene levels could be partially explained the analyzed timepoints. One must consider proteins' turnover rate and temporal relationship between gene expression and protein synthesis. Evaluation of gene expression could perhaps be performed at earlier timepoints as well (e.g. diff. days 2 or 3) and be compared to protein expression at later timepoints (e.g. diff. day 5). Moreover, the variation of YWHAZ expression levels could be another reason for the contradictory results. Alternative reference genes (e.g. Rpl13A, CycA, Pgk1) should be considered and tested [143].

Results of the influence of mechanical stimuli produced by micropillars are also inconclusive. Although initially there may be more MBP^+ cells in flat surfaces, throughout differentiation time this percentage increases for micropillars platforms. In this case, the RT-qPCR results are in line with the ICC results. In fact, for each PDMS formulation, cells cultured on micropillars present higher MBP gene levels than those cultured in flat surfaces. Therefore, the presence of micropillars apparently promotes antigenic differentiation of OPCs into fully mature OLs. Nonetheless, the same cannot be concluded about morphological complexity. Results at diff. day 5 suggest there is a tendency for a higher percentage of cells in stage IV in flat surfaces than micropillars' platforms. Such inconsistency may be due to errors in the classification of differentiation stages (the selected approach is discussed later). Yet, another hypothesis could be formulated: because mature OLs have processes wrapping around micropillars, these processes could be "less available" for branching, so OLs would not apparently be in differentiation stage IV. In fact, it appears that MBP area per cell is lower for thicker micropillars than flat surfaces, which could endorse this hypothesis.

When it comes to the influence of diameter, larger diameters (particularly 4 and 5 μm micropillars) seem to promote antigenic differentiation. The percentage of myelinated micropillars is higher for this type of micropillars. However, the number of myelinated micropillars per MBP^+ cell does not reveal such clear tendencies. Perhaps a more accurate approach would be to directly determine the number of micropillars myelinated by each cell and consider the mode. This would require relating three different objects – nucleus, cellular network and micropillars – which would be technically difficult and highly prone to errors. Although that method was not adopted in this case, it could be considered as an improvement.

More importantly, the reported results correspond to a reduced number of independent experiments (only n=2 in each approach). A higher number of biological replicates would be important for conclusive results, particularly using primary cultures.

Several aspects of the image analysis process and experimental procedure are worth of emphasis, due to their potential effect in final results.

The "Collar Occupancy" pipeline was adapted from the work of Bouçanova and colleagues [134]. The protocol uses collar occupancy to classify oligodendroglial cells into one of four differentiation stages. Collar occupancy is calculated based on the percentage of the collar area that is occupied by cellular protrusions, detected

with tubulin staining. This method is easier to implement because it takes into account only a small area around the nucleus, decreasing the chances of overlapping objects and reducing the complexity of analysis. However, tubulin is only present in the main primary and secondary processes of OLs. The morphology and extension of actin filaments is a key characteristic of mature, myelinating OLs. For example, actin filaments present in myelin membranes may be a differentiating factor between a stage III and a stage IV OL. Actin filaments are not considered in this classification method. Therefore, although validated and published, this may not be the most appropriate method for the classification of oligodendroglial cells into differentiation stages I to IV. Results obtained with this protocol presented few statistically significant differences between unique conditions. Considering that two differentiation stages may be distinguished by the presence of tubulin$^-$, actin$^+$ secondary/tertiary processes, some stage IV cells could have been erroneously classified as stage III cells, which could partially explain why most cells remain on stage III and not on stage IV at diff. day 5.

Initially, the Collar Occupancy protocol was tested on the INCell Investigator software, which uses the original images taken from INCell Analyzer 2000. However, the obtained results were not accurate – most cells on diff. day 5 were classified as being on differentiation stage I or II. It was noticed that the tubulin segments were not correctly segmented and seemed "fragmented". The use of 4% PFA may have caused loss of proteins and fragmentation of microtubule processes, which resulted in loss of tubulin segments within the collar area and underestimation of collar occupancy. Consequently, it was necessary to pre-process the tubulin images, in order to have clearer tubulin segments and accentuate some pixels that belong to these segments. The alternative CellProfiler pipeline provided by the authors was used in order to use these pre-segmented images. Although ilastik segmentation may improve the detection of the entire extension of processes, it also appears to slightly "thicken" them. Therefore, it is possible that the calculated collar occupancy is higher than the real values and, overall, cells are less differentiated than determined. Because collar occupancy, as a variable, has a quasi-normal distribution, this imprecision mostly affects cells identified in differentiation stages II and III (because the majority of cells are in these stages) - which may also explain the inexistence of significant differences from day 1 to 5. Notwithstanding, live cell imaging shows OPCs rapidly extend processes in the first differentiation days, explaining why the percentage of cells on differentiation stage I is so reduced even at this early timepoint. Due to the transition from INCell Investigator to CellProfiler, it was also not possible to use the gates for each stage determined in the paper. New gates had to be determined through visual inspection – which presented some technical difficulties due to the hardly interactive CellProfiler interface. A manual classification of at least one independent experiment would be necessary to validate these new gates. Alternatively, using microtubule protecting-PFA (MP-PFA) could improve the quality of fixation and, consequently, the quality of images [149]. This would be advantageous since the original images could be directly used for evaluation of OLs' differentiation stage.

The "Myelinated Micropillars" pipeline was entirely developed for this project. This pipeline was used to determine the percentage of MBP$^+$ cells, MBP area per cell, the percentage of myelinated micropillars and number of myelinated micropillars per MBP$^+$ cell. In order to easily identify micropillars, MBP in focus and MBP around pillars as primary objects, it was also necessary to pre-segment the correspondent images (brightfield, MBP wix1 and MBP wix2) using ilastik. The greatest challenge was the segmentation of micropillars. Initially, the brightfield images were acquired

with little contrast, so pixels in the center of the micropillars had the same color as the background. Because of this the segmentation included a lot of debris, i.e. pixels from the background that did not correspond to micropillars. The issue was solved by improving image acquisition: the brightfield images were captured in a z-plane that provided high contrast, so that micropillars corresponded to white pixels on a dark background.

Another difficult task was to detect the MBP signal in the pillar areas and relate these primary objects (denominated "MBPpillars") with micropillars. This was an important step in order to avoid overestimation of myelinated pillars. Due to variations in the MBP signal intensity, occasionally two or three "MBPpillars" objects could be identified in the area of one micropillar. Therefore, it was not possible to take the total number of "MBPinPillars" objects, but these objects had to be related to the correspondent micropillar.

The first attempted approach to identify myelinated micropillars was to use CellProfiler Analyst: create a training set with myelinated and non-myelinated micropillars, train a classification algorithm and classify micropillars. However, for unidentified reasons, CellProfiler Analyst was unable to identify all micropillar objects (e.g. in an image with 500 micropillars, it would only identify the first 100), which resulted in quantification errors. Quantification was then performed using Microsoft Excel and establishing thresholds through visual inspection. With this method, myelinated micropillars are identified only according to an intensity thresholds applied to the MBPinPillars objects. A manual counting of at least one independent experiment would be necessary to validate these thresholds.

Although the developed platform differs in many aspects from previously published systems, the obtained results are in line with other conclusions [26], [72], [99], [103], [104], [106]. Models reviewed in Chapter 1 have a lower range of stiffness, closer to the *in vivo* scenario. Overall, the optimal stiffness for OPC culture and differentiation has been determined to be around 0.7-1 kPa. Similarly, our model reveals that softer PDMS platforms promote branching and MBP expression. It is also relevant to highlight that this corresponds to a "2.5D" model – oligodendroglial cells are cultured in 2D but wrap micropillars in the z-axis. Regarding micropillars' presence, it was not possible to obtain conclusive results. Analysis of OPC cultures on mixed micropillars (i.e. OPCs in contact with micropillars of various diameters) would be the most appropriate approach to draw conclusions on this stimulus - rather than combination of data obtained for different diameters. Results about the influence of micropillars' diameters were not conclusive – although tendencies indicated that higher diameters (4 and 5 μm) seemed to promote OPC differentiation and micropillars' wrapping. This tendency is in line with published data [26], [103], [104], [106]. It is interesting to observe that these diameters are, in reality, higher than the average diameter of CNS axons (1-2 μm).

Chapter 6

Conclusions and Future Perspectives

Comprehension of myelination and myelin regeneration is of utmost importance in the development of therapeutic strategies for demyelinating diseases such as MS. These highly complex processes englobe not only chemical mechanisms, but also biomechanical signaling. Since oligodendroglial cells are mechanosensitive, *in vitro* systems developed for the recapitulation of OPC differentiation and myelination should provide appropriate physical and mechanical cues, mimicking the CNS milieu.

In vitro systems published in this framework are few and present some drawbacks (as reviewed in Chapters 1 and 5). As a consequence, various aspects of the mechanobiology of oligodendrocytes remain to be clarified – particularly the influence of substrate stiffness and axonal diameter. Acknowledging these unmet questions, this project aimed to evaluate OPC differentiation and myelination using a micropillars' platforms and implementing automated analysis methods.

Using an accessible and scalable fabrication method (replica molding), it was possible to produce PDMS micropillars with biologically-relevant geometry (micropillars of 1-5 μm diameters) and considerably reduced stiffness (bulk PDMS of 380 kPa), technically advantageous for screening and amenable for chemical and/or physical surface modifications. A system that promotes OPC differentiation and mimics axonal wrapping and formation of myelin-like sheaths was established with this micropillars' platform. Furthermore, the development of automated image analysis pipelines with open-source software allowed the assessment of the effect of substrate stiffness and micropillars' diameter in the aforementioned biological processes.

The results suggest that soft PDMS substrates (with mechanical properties closer to brain parenchyma and biological axons) promote OPC antigenic and morphological differentiation, despite not exerting a significant influence in micropillars' wrapping. On the other hand, there is a tendency for higher differentiation and wrapping of 4 and 5 μm micropillars in comparison to thinner micropillars. Live imaging of OPCs confirms these cells have dynamic processes and interact closely with micropillars.

This approach endorses the importance of adopting systems that physically and mechanically resemble the *in vivo* microenvironment. The implementation of these systems may be critical to obtain reliable data on OL's biology, even in other frameworks (e.g. in the context of biochemical studies).

To better understand to what extent the OPC differentiation and myelination processes are recapitulated in this platform, future studies could address the role of the cytoskeleton and mechanotransduction mechanisms. Since actin filaments are particularly relevant in OLs' process outgrowth and axonal wrapping, labeling of F-actin and live observation of OLs' interaction with micropillars (e.g. with the SiR Actin

dye) could be of particular interest. It could also be relevant to investigate the role of integrin receptors, adaptor proteins (e.g. FAK, Fyn kinase or ILK) and signaling pathways typically involved in OLs' mechanotransduction mechanisms (e.g. PI3K, RhoA/ROCK pathways). In order to observe the ultrastructure of myelin-like sheaths and oligodendrocytes engaging micropillars, OPC cultures on micropillars could be analyzed using TEM. On a related note, the protocol for evaluation of OLs' differentiation stage could be improved by taking into account the actin network. An actin staining could allow for a more rigorous distinction between OLs in differentiation stage III or IV, for example. Regarding the platform itself, it would be interesting to fabricate micropillars with fluorescent PDMS, for a more efficient imaging, segmentation and detection of the pillars (in comparison to brightfield images). Considering the reported difficulties in image acquisition, future work should also be dedicated to improvement and automation of image acquisition (e.g. imaging micropillars' platforms using an upright microscope). Finally, despite being initially developed for recapitulation of myelination, this micropillars' platform can be adapted for the study of demyelination mechanisms – namely by providing biochemical or mechanical cues that resemble the *in vivo* acute or chronic demyelination lesion.

The developed platform corresponds to an upgrade of previous systems for the recapitulation of OPC differentiation and myelination, resulting from the crossover of materials science and automated output analysis. The reported improvements pave the way for the design of a high-throughput system that is biologically relevant, versatile, adaptable, yet user friendly. The applicability of this platform ranges from fundamental biology studies regarding the (de)myelination process to drug screening.

Bibliography

[1] K.-A. Nave and H. B. Werner, “Myelination of the nervous system: Mechanisms and functions.”, *Annual review of cell and developmental biology*, vol. 30, pp. 503–533, 2014, ISSN: 1530-8995 (Electronic). DOI: 10.1146/annurev-cellbio-100913-013101.

[2] A. Wilkins, S. Chandran, and A. Compston, “A role for oligodendrocyte-derived igf-1 in trophic support of cortical neurons.”, *Glia*, vol. 36, no. 1, pp. 48–57, 2001, ISSN: 0894-1491 (Print).

[3] A. Wilkins, H. Majed, R. Layfield, A. Compston, and S. Chandran, “Oligodendrocytes promote neuronal survival and axonal length by distinct intracellular mechanisms: A novel role for oligodendrocyte-derived glial cell line-derived neurotrophic factor.”, *The Journal of neuroscience : the official journal of the Society for Neuroscience*, vol. 23, no. 12, pp. 4967–4974, 2003, ISSN: 1529-2401 (Electronic).

[4] Y. Lee, B. M. Morrison, Y. Li, S. Lengacher, M. H. Farah, P. N. Hoffman, Y. Liu, A. Tsingalia, L. Jin, P.-W. Zhang, L. Pellerin, P. J. Magistretti, and J. D. Rothstein, “Oligodendroglia metabolically support axons and contribute to neurodegeneration.”, *Nature*, vol. 487, no. 7408, pp. 443–448, 2012, ISSN: 1476-4687 (Electronic). DOI: 10.1038/nature11314.

[5] J. P. Michalski and R. Kothary, “Oligodendrocytes in a nutshell”, *Front Cell Neurosci*, vol. 9, p. 340, 2015, ISSN: 1662-5102 (Print)1662-5102. DOI: 10.3389/fncel.2015.00340.

[6] S. Aggarwal, L. Yurlova, and M. Simons, “Central nervous system myelin: Structure, synthesis and assembly.”, *Trends in cell biology*, vol. 21, no. 10, pp. 585–593, 2011, ISSN: 1879-3088 (Electronic). DOI: 10.1016/j.tcb.2011.06.004.

[7] H. Shi, X. Hu, R. K. Leak, Y. Shi, C. An, J. Suenaga, J. Chen, and Y. Gao, “Demyelination as a rational therapeutic target for ischemic or traumatic brain injury.”, *Experimental neurology*, vol. 272, pp. 17–25, 2015, ISSN: 1090-2430 (Electronic). DOI: 10.1016/j.expneurol.2015.03.017.

[8] S. Love, “Demyelinating diseases”, *Journal of Clinical Pathology*, vol. 59, no. 11, pp. 1151–1159, 2006, ISSN: 0021-9746. DOI: 10.1136/jcp.2005.031195.

[9] L. Conforti, J. Gilley, and M. P. Coleman, “Wallerian degeneration: An emerging axon death pathway linking injury and disease”, *Nat Rev Neurosci*, vol. 15, no. 6, pp. 394–409, 2014, ISSN: 1471-003x. DOI: 10.1038/nrn3680.

[10] R. J. M. Franklin and C. Ffrench-Constant, “Remyelination in the cns: From biology to therapy.”, *Nature reviews. Neuroscience*, vol. 9, no. 11, pp. 839–855, 2008, ISSN: 1471-0048 (Electronic). DOI: 10.1038/nrn2480.

[11] N. M. S. Society, Web Page, 2019. [Online]. Available: http://www.nationalmssociety.org/What-is-MS/Who-Gets-MS.

[12] M. S. I. Federation.

[13] E. Leray, T. Moreau, A. Fromont, and G. Edan, “Epidemiology of multiple sclerosis”, *Rev Neurol (Paris)*, vol. 172, no. 1, pp. 3–13, 2016, ISSN: 0035-3787 (Print)0035-3787. DOI: 10.1016/j.neurol.2015.10.006.

[14] M. T. Wallin, W. J. Culpepper, J. D. Campbell, L. M. Nelson, A. Langer-Gould, R. A. Marrie, G. R. Cutter, W. E. Kaye, L. Wagner, H. Tremlett, S. L. Buka, P. Dilokthornsakul, B. Topol, L. H. Chen, and N. G. LaRocca, “The prevalence of ms in the united states: A population-based estimate using health claims data”, *Neurology*, 2019, ISSN: 0028-3878. DOI: 10.1212/wnl.0000000000007035.

[15] M. Trisolini, A. Honeycutt, J. Wiener, and S. Lesesne, “Global economic impact of multiple sclerosis”, Multiple Sclerosis International Federation, Report 0211748.000.001, 2010.

[16] C. Lubetzki and B. Stankoff, “Demyelination in multiple sclerosis.”, *Handbook of clinical neurology*, vol. 122, pp. 89–99, 2014, ISSN: 0072-9752 (Print). DOI: 10.1016/B978-0-444-52001-2.00004-2.

[17] I. Kister, T. E. Bacon, E. Chamot, A. R. Salter, G. R. Cutter, J. T. Kalina, and J. Herbert, "Natural history of multiple sclerosis symptoms", *Int J MS Care*, vol. 15, no. 3, pp. 146–56, 2013, ISSN: 1537-2073 (Print). DOI: 10.7224/1537-2073.2012-053.

[18] R. Dutta and B. D. Trapp, "Mechanisms of neuronal dysfunction and degeneration in multiple sclerosis", *Prog Neurobiol*, vol. 93, no. 1, pp. 1–12, 2011, ISSN: 0301-0082. DOI: 10.1016/j.pneurobio.2010.09.005.

[19] R. J. Franklin and G. L. Hinks, "Understanding cns remyelination: Clues from developmental and regeneration biology.", *Journal of neuroscience research*, vol. 58, no. 2, pp. 207–213, 1999, ISSN: 0360-4012 (Print).

[20] B. Kornek, M. K. Storch, R. Weissert, E. Wallstroem, A. Stefferl, T. Olsson, C. Linington, M. Schmidbauer, and H. Lassmann, "Multiple sclerosis and chronic autoimmune encephalomyelitis: A comparative quantitative study of axonal injury in active, inactive, and remyelinated lesions.", *The American journal of pathology*, vol. 157, no. 1, pp. 267–276, 2000, ISSN: 0002-9440 (Print). DOI: 10.1016/S0002-9440(10)64537-3.

[21] N. Dargahi, M. Katsara, T. Tselios, M.-E. Androutsou, M. de Courten, J. Matsoukas, and V. Apostolopoulos, "Multiple sclerosis: Immunopathology and treatment update.", *Brain sciences*, vol. 7, no. 7, 2017, ISSN: 2076-3425 (Print). DOI: 10.3390/brainsci7070078.

[22] N. G. Bauer and C. Ffrench-Constant, "Physical forces in myelination and repair: A question of balance?", *Journal of Biology*, vol. 8, no. 8, p. 78, 2009, ISSN: 1475-4924. DOI: 10.1186/jbiol169.

[23] T. a. Lourenco, "Modulation of oligodendrocyte differentiation and maturation by combined biochemical and mechanical cues", *Scientific Reports*, vol. 6, p. 21 563, 2016, ISSN: 2045-2322 (Electronic). DOI: 10.1038/srep21563.

[24] H. S. Domingues, A. Cruz, J. R. Chan, J. B. Relvas, B. Rubinstein, and I. M. Pinto, "Mechanical plasticity during oligodendrocyte differentiation and myelination", *Glia*, vol. 66, no. 1, pp. 5–14, 2018, ISSN: 0894-1491. DOI: 10.1002/glia.23206.

[25] E. G. Hughes and B. Appel, "The cell biology of cns myelination", *Current Opinion in Neurobiology*, vol. 39, pp. 93–100, 2016, ISSN: 0959-4388. DOI: https://doi.org/10.1016/j.conb.2016.04.013.

[26] M. Bechler, L. Byrne, and C. ffrench Constant, "Cns myelin sheath lengths are an intrinsic property of oligodendrocytes", in *Curr Biol*. 2015, vol. 25, pp. 2411–6, ISBN: 0960-9822 (Print)1879-0445 (Electronic). DOI: 10.1016/j.cub.2015.07.056.

[27] V. E. Miron, T. Kuhlmann, and J. P. Antel, "Cells of the oligodendroglial lineage, myelination, and remyelination", *Biochim Biophys Acta*, vol. 1812, no. 2, pp. 184–193, 2011, ISSN: 0006-3002 (Print)0006-3002. DOI: 10.1016/j.bbadis.2010.09.010.

[28] K. Bercury and W. Macklin, "Dynamics and mechanisms of cns myelination", *Developmental Cell*, vol. 32, no. 4, pp. 447–458, 2015, ISSN: 1534-5807. DOI: https://doi.org/10.1016/j.devcel.2015.01.016.

[29] D. E. Bergles and W. D. Richardson, "Oligodendrocyte development and plasticity.", *Cold Spring Harbor perspectives in biology*, vol. 8, no. 2, a020453, 2015, ISSN: 1943-0264 (Electronic). DOI: 10.1101/cshperspect.a020453.

[30] S. Mitew, C. M. Hay, H. Peckham, J. Xiao, M. Koenning, and B. Emery, "Mechanisms regulating the development of oligodendrocytes and central nervous system myelin", *Neuroscience*, vol. 276, pp. 29–47, 2014, ISSN: 0306-4522. DOI: 10.1016/j.neuroscience.2013.11.02910.1016/j.neuroscience.2013.11.029.Epub2013Nov22..

[31] K.-J. Chang, S. A. Redmond, and J. R. Chan, "Remodeling myelination: Implications for mechanisms of neural plasticity", *Nature Neuroscience*, vol. 19, p. 190, 2016. DOI: 10.1038/nn.4200. [Online]. Available: https://doi.org/10.1038/nn.4200.

[32] M. E. Boyle, E. O. Berglund, K. K. Murai, L. Weber, E. Peles, and B. Ranscht, "Contactin orchestrates assembly of the septate-like junctions at the paranode in myelinated peripheral nerve", *Neuron*, vol. 30, no. 2, pp. 385–97, 2001, ISSN: 0896-6273 (Print)0896-6273. [Online]. Available: http://dx.doi.org/.

[33] H. Wake, F. C. Ortiz, D. H. Woo, P. R. Lee, M. C. Angulo, and R. D. Fields, "Nonsynaptic junctions on myelinating glia promote preferential myelination of electrically active axons", *Nat Commun*, vol. 6, p. 7844, 2015, ISSN: 2041-1723. DOI: 10.1038/ncomms8844.

[34] K. M. Young, K. Psachoulia, R. B. Tripathi, S. J. Dunn, L. Cossell, D. Attwell, K. Tohyama, and W. D. Richardson, "Oligodendrocyte dynamics in the healthy adult cns: Evidence for myelin remodeling", *Neuron*, vol. 77, no. 5, pp. 873–85, 2013, ISSN: 0896-6273. DOI: 10.1016/j.neuron.2013.01.006.

[35] M. Prinz, F. Garbe, H. Schmidt, A. Mildner, I. Gutcher, K. Wolter, M. Piesche, R. Schroers, E. Weiss, C. J. Kirschning, C. D. Rochford, W. Bruck, and B. Becher, "Innate immunity mediated by tlr9 modulates pathogenicity in an animal model of multiple sclerosis", *J Clin Invest*, vol. 116, no. 2, pp. 456–64, 2006, ISSN: 0021-9738 (Print)0021-9738. DOI: 10.1172/jci26078.

[36] S. L. Hauser, A. K. Bhan, F. Gilles, M. Kemp, C. Kerr, and H. L. Weiner, "Immunohistochemical analysis of the cellular infiltrate in multiple sclerosis lesions", *Ann Neurol*, vol. 19, no. 6, pp. 578–87, 1986, ISSN: 0364-5134 (Print)0364-5134. DOI: 10.1002/ana.410190610.

[37] M. Greter, F. L. Heppner, M. P. Lemos, B. M. Odermatt, N. Goebels, T. Laufer, R. J. Noelle, and B. Becher, "Dendritic cells permit immune invasion of the cns in an animal model of multiple sclerosis", *Nat Med*, vol. 11, no. 3, pp. 328–34, 2005, ISSN: 1078-8956 (Print)1078-8956. DOI: 10.1038/nm1197.

[38] R. Hoftberger, F. Aboul-Enein, W. Brueck, C. Lucchinetti, M. Rodriguez, M. Schmidbauer, K. Jellinger, and H. Lassmann, "Expression of major histocompatibility complex class i molecules on the different cell types in multiple sclerosis lesions", *Brain Pathol*, vol. 14, no. 1, pp. 43–50, 2004, ISSN: 1015-6305 (Print)1015-6305. [Online]. Available: http://dx.doi.org/.

[39] G. Disanto, J. M. Morahan, M. H. Barnett, G. Giovannoni, and S. V. Ramagopalan, "The evidence for a role of b cells in multiple sclerosis", *Neurology*, vol. 78, no. 11, pp. 823–32, 2012, ISSN: 0028-3878. DOI: 10.1212/WNL.0b013e318249f6f0.

[40] A. Mirshafiey and M. Kianiaslani, "Autoantigens and autoantibodies in multiple sclerosis", *Iran J Allergy Asthma Immunol*, vol. 12, no. 4, pp. 292–303, 2013, ISSN: 1735-1502 (Print)1735-1502. [Online]. Available: http://dx.doi.org/.

[41] J. K. Fazakerley and R. Walker, "Virus demyelination.", *Journal of neurovirology*, vol. 9, no. 2, pp. 148–164, 2003, ISSN: 1355-0284 (Print). DOI: 10.1080/13550280390194046.

[42] I. Coman, M. S. Aigrot, D. Seilhean, R. Reynolds, J. A. Girault, B. Zalc, and C. Lubetzki, "Nodal, paranodal and juxtaparanodal axonal proteins during demyelination and remyelination in multiple sclerosis", *Brain*, vol. 129, no. Pt 12, pp. 3186–95, 2006, ISSN: 0006-8950. DOI: 10.1093/brain/awl144.

[43] M. J. Craner, J. Newcombe, J. A. Black, C. Hartle, M. L. Cuzner, and S. G. Waxman, "Molecular changes in neurons in multiple sclerosis: Altered axonal expression of nav1.2 and nav1.6 sodium channels and na+/ca2+ exchanger", *Proc Natl Acad Sci U S A*, vol. 101, no. 21, pp. 8168–73, 2004, ISSN: 0027-8424 (Print)0027-8424. DOI: 10.1073/pnas.0402765101.

[44] L. W. Lau, R. Cua, M. B. Keough, S. Haylock-Jacobs, and V. W. Yong, "Pathophysiology of the brain extracellular matrix: A new target for remyelination.", *Nature reviews. Neuroscience*, vol. 14, no. 10, pp. 722–729, 2013, ISSN: 1471-0048 (Electronic). DOI: 10.1038/nrn3550.

[45] K. L. Adams and V. Gallo, "The diversity and disparity of the glial scar", *Nature Neuroscience*, vol. 21, no. 1, pp. 9–15, 2018, ISSN: 1546-1726. DOI: 10.1038/s41593-017-0033-9.

[46] P. Rieckmann and K. J. Smith, "Multiple sclerosis: More than inflammation and demyelination.", *Trends in neurosciences*, vol. 24, no. 8, pp. 435–437, 2001, ISSN: 0166-2236 (Print).

[47] S. Ljubisavljevic, "Oxidative stress and neurobiology of demyelination.", *Molecular neurobiology*, vol. 53, no. 1, pp. 744–758, 2016, ISSN: 1559-1182 (Electronic). DOI: 10.1007/s12035-014-9041-x.

[48] M. B. Bunge, R. P. Bunge, and H. Ris, "Ultrastructural study of remyelination in an experimental lesion in adult cat spinal cord", *J Biophys Biochem Cytol*, vol. 10, pp. 67–94, 1961, ISSN: 0095-9901 (Print)0095-9901. [Online]. Available: http://dx.doi.org/.

[49] H. S. Keirstead and W. F. Blakemore, "Identification of post-mitotic oligodendrocytes incapable of remyelination within the demyelinated adult spinal cord", *J Neuropathol Exp Neurol*, vol. 56, no. 11, pp. 1191–201, 1997, ISSN: 0022-3069 (Print)0022-3069. [Online]. Available: http://dx.doi.org/.

[50] J. M. Gensert and J. E. Goldman, "Endogenous progenitors remyelinate demyelinated axons in the adult cns", *Neuron*, vol. 19, no. 1, pp. 197–203, 1997, ISSN: 0896-6273 (Print)0896-6273. [Online]. Available: http://dx.doi.org/.

[51] K. E. Rhodes, G. Raivich, and J. W. Fawcett, “The injury response of oligodendrocyte precursor cells is induced by platelets, macrophages and inflammation-associated cytokines”, *Neuroscience*, vol. 140, no. 1, pp. 87–100, 2006, ISSN: 0306-4522 (Print)0306-4522. DOI: 10.1016/j.neuroscience.2006.01.055.

[52] H. S. Domingues, C. C. Portugal, R. Socodato, and J. B. Relvas, “Oligodendrocyte, astrocyte, and microglia crosstalk in myelin development, damage, and repair”, *Front Cell Dev Biol*, vol. 4, p. 71, 2016, ISSN: 2296-634X (Print)2296-634x. DOI: 10.3389/fcell.2016.00071.

[53] W. F. Blakemore, “Pattern of remyelination in the cns”, *Nature*, vol. 249, no. 457, pp. 577–8, 1974, ISSN: 0028-0836 (Print)0028-0836. [Online]. Available: http://dx.doi.org/.

[54] D. M. Chari and W. F. Blakemore, “Efficient recolonisation of progenitor-depleted areas of the cns by adult oligodendrocyte progenitor cells”, *Glia*, vol. 37, no. 4, pp. 307–13, 2002, ISSN: 0894-1491 (Print)0894-1491. [Online]. Available: http://dx.doi.org/.

[55] A. Niehaus, J. Shi, M. Grzenkowski, M. Diers-Fenger, J. Archelos, H. P. Hartung, K. Toyka, W. Bruck, and J. Trotter, “Patients with active relapsing-remitting multiple sclerosis synthesize antibodies recognizing oligodendrocyte progenitor cell surface protein: Implications for remyelination”, *Ann Neurol*, vol. 48, no. 3, pp. 362–71, 2000, ISSN: 0364-5134 (Print)0364-5134. [Online]. Available: http://dx.doi.org/.

[56] G. Wolswijk, “Oligodendrocyte regeneration in the adult rodent cns and the failure of this process in multiple sclerosis.”, *Progress in brain research*, vol. 117, pp. 233–247, 1998, ISSN: 0079-6123 (Print).

[57] ——, “Chronic stage multiple sclerosis lesions contain a relatively quiescent population of oligodendrocyte precursor cells”, *J Neurosci*, vol. 18, no. 2, pp. 601–9, 1998, ISSN: 0270-6474 (Print)0270-6474. [Online]. Available: http://dx.doi.org/.

[58] T. Kuhlmann, V. Miron, Q. Cui, C. Wegner, J. Antel, and W. Bruck, “Differentiation block of oligodendroglial progenitor cells as a cause for remyelination failure in chronic multiple sclerosis”, *Brain*, vol. 131, no. Pt 7, pp. 1749–58, 2008, ISSN: 0006-8950. DOI: 10.1093/brain/awn096.

[59] S. A. Back, T. M. Tuohy, H. Chen, N. Wallingford, A. Craig, J. Struve, N. L. Luo, F. Banine, Y. Liu, A. Chang, B. D. Trapp, J. Bebo B. F., M. S. Rao, and L. S. Sherman, “Hyaluronan accumulates in demyelinated lesions and inhibits oligodendrocyte progenitor maturation”, *Nat Med*, vol. 11, no. 9, pp. 966–72, 2005, ISSN: 1078-8956 (Print)1078-8956. DOI: 10.1038/nm1279.

[60] J. F. Talbott, D. N. Loy, Y. Liu, M. S. Qiu, M. B. Bunge, M. S. Rao, and S. R. Whittemore, “Endogenous nkx2.2+/olig2+ oligodendrocyte precursor cells fail to remyelinate the demyelinated adult rat spinal cord in the absence of astrocytes”, *Exp Neurol*, vol. 192, no. 1, pp. 11–24, 2005, ISSN: 0014-4886 (Print)0014-4886. DOI: 10.1016/j.expneurol.2004.05.038.

[61] P. Charles, R. Reynolds, D. Seilhean, G. Rougon, M. S. Aigrot, A. Niezgoda, B. Zalc, and C. Lubetzki, “Re-expression of psa-ncam by demyelinated axons: An inhibitor of remyelination in multiple sclerosis?”, *Brain*, vol. 125, no. Pt 9, pp. 1972–9, 2002, ISSN: 0006-8950 (Print)0006-8950. [Online]. Available: http://dx.doi.org/.

[62] G. R. John, S. L. Shankar, B. Shafit-Zagardo, A. Massimi, S. C. Lee, C. S. Raine, and C. F. Brosnan, “Multiple sclerosis: Re-expression of a developmental pathway that restricts oligodendrocyte maturation”, *Nat Med*, vol. 8, no. 10, pp. 1115–21, 2002, ISSN: 1078-8956 (Print)1078-8956. DOI: 10.1038/nm781.

[63] R. J. Franklin, “Why does remyelination fail in multiple sclerosis?”, *Nat Rev Neurosci*, vol. 3, no. 9, pp. 705–14, 2002, ISSN: 1471-003X (Print)1471-003x. DOI: 10.1038/nrn917.

[64] A. J. Bieber, D. R. Ure, and M. Rodriguez, “Genetically dominant spinal cord repair in a murine model of chronic progressive multiple sclerosis”, *J Neuropathol Exp Neurol*, vol. 64, no. 1, pp. 46–57, 2005, ISSN: 0022-3069 (Print)0022-3069. [Online]. Available: http://dx.doi.org/.

[65] S. A. Shields, J. M. Gilson, W. F. Blakemore, and R. J. Franklin, “Remyelination occurs as extensively but more slowly in old rats compared to young rats following gliotoxin-induced cns demyelination”, *Glia*, vol. 28, no. 1, pp. 77–83, 1999, ISSN: 0894-1491 (Print)0894-1491. [Online]. Available: http://dx.doi.org/.

[66] W. W. Li, J. Penderis, C. Zhao, M. Schumacher, and R. J. Franklin, “Females remyelinate more efficiently than males following demyelination in the aged but not young adult cns”, *Exp Neurol*, vol. 202, no. 1, pp. 250–4, 2006, ISSN: 0014-4886 (Print)0014-4886. DOI: 10.1016/j.expneurol.2006.05.012.

[67] A. Barateiro, D. Brites, and A. Fernandes, "Oligodendrocyte development and myelination in neurodevelopment: Molecular mechanisms in health and disease.", *Current pharmaceutical design*, vol. 22, no. 6, pp. 656–679, 2016, ISSN: 1873-4286 (Electronic). [Online]. Available: http://www.eurekaselect.com/137549/article.

[68] J. Patel and R. Balabanov, "Molecular mechanisms of oligodendrocyte injury in multiple sclerosis and experimental autoimmune encephalomyelitis", *International Journal of Molecular Sciences*, vol. 13, no. 8, pp. 10 647–10 659, 2012, ISSN: 1422-0067. DOI: 10.3390/ijms130810647.

[69] J. M. Barnes, L. Przybyla, and V. M. Weaver, "Tissue mechanics regulate brain development, homeostasis and disease", *J Cell Sci*, vol. 130, no. 1, pp. 71–82, 2017, ISSN: 0021-9533. DOI: 10.1242/jcs.191742.

[70] X. Lin, Y. Shi, Y. Cao, and W. Liu, "Recent progress in stem cell differentiation directed by material and mechanical cues", *Biomed Mater*, vol. 11, no. 1, p. 014 109, 2016, ISSN: 1748-6041. DOI: 10.1088/1748-6041/11/1/014109.

[71] J. M. Stukel and R. K. Willits, "Mechanotransduction of neural cells through cell-substrate interactions", *Tissue Eng Part B Rev*, vol. 22, no. 3, pp. 173–82, 2016, ISSN: 1937-3368. DOI: 10.1089/ten.TEB.2015.0380.

[72] A. Jagielska, A. L. Norman, G. Whyte, K. J. V. Vliet, J. Guck, and R. J. M. Franklin, "Mechanical environment modulates biological properties of oligodendrocyte progenitor cells.", *Stem cells and development*, vol. 21, no. 16, pp. 2905–2914, 2012, ISSN: 1557-8534 (Electronic). DOI: 10.1089/scd.2012.0189.

[73] N. Wang, "Review of cellular mechanotransduction", *Journal of Physics D: Applied Physics*, vol. 50, no. 23, p. 233 002, 2017, ISSN: 0022-3727 1361-6463. DOI: 10.1088/1361-6463/aa6e18.

[74] E. K. Paluch, C. M. Nelson, N. Biais, B. Fabry, J. Moeller, B. L. Pruitt, C. Wollnik, G. Kudryasheva, F. Rehfeldt, and W. Federle, "Mechanotransduction: Use the force(s)", *BMC Biology*, vol. 13, no. 1, p. 47, 2015, ISSN: 1741-7007. DOI: 10.1186/s12915-015-0150-4.

[75] J. Weickenmeier, R. de Rooij, S. Budday, P. Steinmann, T. C. Ovaert, and E. Kuhl, "Brain stiffness increases with myelin content.", *Acta biomaterialia*, vol. 42, pp. 265–272, 2016, ISSN: 1878-7568 (Electronic). DOI: 10.1016/j.actbio.2016.07.040.

[76] J. Weickenmeier, R. de Rooij, S. Budday, T. C. Ovaert, and E. Kuhl, "The mechanical importance of myelination in the central nervous system.", *Journal of the mechanical behavior of biomedical materials*, vol. 76, pp. 119–124, 2017, ISSN: 1878-0180 (Electronic). DOI: 10.1016/j.jmbbm.2017.04.017.

[77] M. Kipp, P. van der Valk, and S. Amor, "Pathology of multiple sclerosis.", *CNS & neurological disorders drug targets*, vol. 11, no. 5, pp. 506–517, 2012, ISSN: 1996-3181 (Electronic).

[78] C. Stadelmann, C. Wegner, and W. Bruck, "Inflammation, demyelination, and degeneration - recent insights from ms pathology.", *Biochimica et biophysica acta*, vol. 1812, no. 2, pp. 275–282, 2011, ISSN: 0006-3002 (Print). DOI: 10.1016/j.bbadis.2010.07.007.

[79] Z. Yin, A. J. Romano, A. Manduca, R. L. Ehman, and r. Huston J., "Stiffness and beyond: What mr elastography can tell us about brain structure and function under physiologic and pathologic conditions", *Top Magn Reson Imaging*, vol. 27, no. 5, pp. 305–318, 2018, ISSN: 0899-3459. DOI: 10.1097/rmr.0000000000000178.

[80] J. Wuerfel, F. Paul, B. Beierbach, U. Hamhaber, D. Klatt, S. Papazoglou, F. Zipp, P. Martus, J. Braun, and I. Sack, "Mr-elastography reveals degradation of tissue integrity in multiple sclerosis", *Neuroimage*, vol. 49, no. 3, pp. 2520–5, 2010, ISSN: 1053-8119. DOI: 10.1016/j.neuroimage.2009.06.018.

[81] K. Riek, J. M. Millward, I. Hamann, S. Mueller, C. F. Pfueller, F. Paul, J. Braun, C. Infante-Duarte, and I. Sack, "Magnetic resonance elastography reveals altered brain viscoelasticity in experimental autoimmune encephalomyelitis", *Neuroimage Clin*, vol. 1, no. 1, pp. 81–90, 2012, ISSN: 2213-1582 (Print)2213-1582. DOI: 10.1016/j.nicl.2012.09.003.

[82] K. Schregel, E. Wuerfel, P. Garteiser, I. Gemeinhardt, T. Prozorovski, O. Aktas, H. Merz, D. Petersen, J. Wuerfel, and R. Sinkus, "Demyelination reduces brain parenchymal stiffness quantified in vivo by magnetic resonance elastography", *Proc Natl Acad Sci U S A*, vol. 109, no. 17, pp. 6650–5, 2012, ISSN: 0027-8424. DOI: 10.1073/pnas.1200151109.

[83] K. J. Streitberger, I. Sack, D. Krefting, C. Pfuller, J. Braun, F. Paul, and J. Wuerfel, "Brain viscoelasticity alteration in chronic-progressive multiple sclerosis", *PLoS One*, vol. 7, no. 1, e29888, 2012, ISSN: 1932-6203. DOI: 10.1371/journal.pone.0029888.

[84] J. M. Millward, J. Guo, D. Berndt, J. Braun, I. Sack, and C. Infante-Duarte, "Tissue structure and inflammatory processes shape viscoelastic properties of the mouse brain", *NMR Biomed*, vol. 28, no. 7, pp. 831–9, 2015, ISSN: 0952-3480. DOI: 10.1002/nbm.3319. [Online]. Available: http://dx.doi.org/10.1002/nbm.3319.

[85] M. M. Urbanski, M. B. Brendel, and C. V. Melendez-Vasquez, "Acute and chronic demyelinated cns lesions exhibit opposite elastic properties", *Scientific Reports*, vol. 9, no. 1, p. 999, 2019, ISSN: 2045-23222045-2322. DOI: doi:10.1038/s41598-018-37745-7.

[86] E. Moeendarbary, I. P. Weber, G. K. Sheridan, D. E. Koser, S. Soleman, B. Haenzi, E. J. Bradbury, J. Fawcett, and K. Franze, "The soft mechanical signature of glial scars in the central nervous system", *Nature Communications*, vol. 8, p. 14 787, 2017. DOI: 10.1038/ncomms14787https://www.nature.com/articles/ncomms14787#supplementary-information.

[87] N. G. Bauer, C. Richter-Landsberg, and C. Ffrench-Constant, "Role of the oligodendroglial cytoskeleton in differentiation and myelination.", *Glia*, vol. 57, no. 16, pp. 1691–1705, 2009, ISSN: 1098-1136 (Electronic). DOI: 10.1002/glia.20885.

[88] B. Kachar, T. Behar, and M. Dubois-Dalcq, "Cell shape and motility of oligodendrocytes cultured without neurons", *Cell Tissue Res*, vol. 244, no. 1, pp. 27–38, 1986, ISSN: 0302-766X (Print)0302-766x. [Online]. Available: http://dx.doi.org/.

[89] K. F. Lunn, P. W. Baas, and I. D. Duncan, "Microtubule organization and stability in the oligodendrocyte.", *The Journal of neuroscience : the official journal of the Society for Neuroscience*, vol. 17, no. 13, pp. 4921–4932, 1997, ISSN: 0270-6474 (Print). [Online]. Available: http://www.jneurosci.org/content/jneuro/17/13/4921.full.pdf.

[90] S. Nawaz, P. Sanchez, S. Schmitt, N. Snaidero, M. Mitkovski, C. Velte, B. R. Bruckner, I. Alexopoulos, T. Czopka, S. Y. Jung, J. S. Rhee, A. Janshoff, W. Witke, I. A. T. Schaap, D. A. Lyons, and M. Simons, "Actin filament turnover drives leading edge growth during myelin sheath formation in the central nervous system.", *Developmental cell*, vol. 34, no. 2, pp. 139–151, 2015, ISSN: 1878-1551 (Electronic). DOI: 10.1016/j.devcel.2015.05.013.

[91] J. B. Zuchero, M. M. Fu, S. A. Sloan, A. Ibrahim, A. Olson, A. Zaremba, J. C. Dugas, S. Wienbar, A. V. Caprariello, C. Kantor, D. Leonoudakis, K. Lariosa-Willingham, G. Kronenberg, K. Gertz, S. H. Soderling, R. H. Miller, and B. A. Barres, "Cns myelin wrapping is driven by actin disassembly", *Dev Cell*, vol. 34, no. 2, pp. 152–67, 2015, ISSN: 1534-5807. DOI: 10.1016/j.devcel.2015.06.011.

[92] H. Wang, T. Rusielewicz, A. Tewari, E. M. Leitman, S. Einheber, and C. V. Melendez-Vasquez, "Myosin ii is a negative regulator of oligodendrocyte morphological differentiation", *J Neurosci Res*, vol. 90, no. 8, pp. 1547–56, 2012, ISSN: 0360-4012. DOI: 10.1002/jnr.23036.

[93] R. W. O'Meara, J.-P. Michalski, and R. Kothary, "Integrin signaling in oligodendrocytes and its importance in cns myelination.", *Journal of signal transduction*, vol. 2011, p. 354 091, 2011, ISSN: 2090-1747 (Electronic). DOI: 10.1155/2011/354091.

[94] A. D. Forrest, H. E. Beggs, L. F. Reichardt, J. L. Dupree, R. J. Colello, and B. Fuss, "Focal adhesion kinase (fak): A regulator of cns myelination", *J Neurosci Res*, vol. 87, no. 15, pp. 3456–64, 2009, ISSN: 0360-4012. DOI: 10.1002/jnr.22022.

[95] A. D. Lafrenaye and B. Fuss, "Focal adhesion kinase can play unique and opposing roles in regulating the morphology of differentiating oligodendrocytes", *J Neurochem*, vol. 115, no. 1, pp. 269–82, 2010, ISSN: 0022-3042. DOI: 10.1111/j.1471-4159.2010.06926.x.

[96] R. W. O'Meara, J. P. Michalski, C. Anderson, K. Bhanot, P. Rippstein, and R. Kothary, "Integrin-linked kinase regulates process extension in oligodendrocytes via control of actin cytoskeletal dynamics", *J Neurosci*, vol. 33, no. 23, pp. 9781–93, 2013, ISSN: 0270-6474. DOI: 10.1523/jneurosci.5582-12.2013.

[97] I. Osorio-Querejeta, M. Saenz-Cuesta, M. Munoz-Culla, and D. Otaegui, "Models for studying myelination, demyelination and remyelination.", *Neuromolecular medicine*, vol. 19, no. 2-3, pp. 181–192, 2017, ISSN: 1559-1174 (Electronic). DOI: 10.1007/s12017-017-8442-1.

[98] P. E. Knapp, W. P. Bartlett, and R. P. Skoff, "Cultured oligodendrocytes mimic in vivo phenotypic characteristics: Cell shape, expression of myelin-specific antigens, and membrane production", *Dev Biol*, vol. 120, no. 2, pp. 356–65, 1987, ISSN: 0012-1606 (Print)0012-1606. [Online]. Available: http://dx.doi.org/.

[99] A. Kippert, D. Fitzner, J. Helenius, and M. Simons, "Actomyosin contractility controls cell surface area of oligodendrocytes", *BMC Cell Biology*, vol. 10, no. 1, p. 71, 2009, ISSN: 1471-2121. DOI: 10.1186/1471-2121-10-71.

[100] X. Li, X. Liu, L. Cui, C. Brunson, W. Zhao, N. R. Bhat, N. Zhang, and X. Wen, "Engineering an in situ crosslinkable hydrogel for enhanced remyelination.", *FASEB journal : official publication of the Federation of American Societies for Experimental Biology*, vol. 27, no. 3, pp. 1127–1136, 2013, ISSN: 1530-6860 (Electronic). DOI: 10.1096/fj.12-211151.

[101] M. M. Urbanski, L. Kingsbury, D. Moussouros, I. Kassim, S. Mehjabeen, N. Paknejad, and C. V. Melendez-Vasquez, "Myelinating glia differentiation is regulated by extracellular matrix elasticity", *Scientific Reports*, vol. 6, p. 33 751, 2016, ISSN: 2045-23222045-2322. DOI: doi:10.1038/srep33751.

[102] P. N. Bullock and L. H. Rome, "Glass micro-fibers: A model system for study of early events in myelination", *J Neurosci Res*, vol. 27, no. 3, pp. 383–93, 1990, ISSN: 0360-4012 (Print)0360-4012. DOI: 10.1002/jnr.490270317.

[103] C. L. Howe, "Coated glass and vicryl microfibers as artificial axons", *Cells Tissues Organs*, vol. 183, no. 4, pp. 180–94, 2006, ISSN: 1422-6405 (Print)1422-6405. DOI: 10.1159/000096509.

[104] S. Lee, M. K. Leach, S. A. Redmond, S. Y. C. Chong, S. H. Mellon, S. J. Tuck, Z.-Q. Q. Feng, J. M. Corey, and J. R. Chan, "A culture system to study oligodendrocyte myelination processes using engineered nanofibers.", *Nature methods*, vol. 9, no. 9, pp. 917–922, 2012, ISSN: 4155149818 1548-7105 (Electronic). DOI: 10.1038/nmeth.2105.

[105] F. Mei, S. P.J. J. Fancy, Y.-A.A. A. Shen, J. Niu, C. Zhao, B. Presley, E. Miao, S. Lee, S. R. Mayoral, S. A. Redmond, A. Etxeberria, L. Xiao, R. J.M. M. Franklin, A. Green, S. L. Hauser, and J. R. Chan, "Micropillar arrays as a high-throughput screening platform for therapeutics in multiple sclerosis.", *Nature medicine*, vol. 20, no. 8, pp. 954–960, 2014, ISSN: 1546-170X (Electronic)\r1078-8956 (Linking) 1546-170X (Electronic). DOI: 10.1038/nm.3618.

[106] D. Espinosa-Hoyos, A. Jagielska, K. A. Homan, H. Du, T. Busbee, D. G. Anderson, N. X. Fang, J. A. Lewis, and K. J. Van Vliet, "Engineered 3d-printed artificial axons", *Sci Rep*, vol. 8, no. 1, p. 478, 2018, ISSN: 2045-2322. DOI: 10.1038/s41598-017-18744-6.

[107] A. F. Christ, K. Franze, H. Gautier, P. Moshayedi, J. Fawcett, R. J. M. Franklin, R. T. Karadottir, and J. Guck, "Mechanical difference between white and gray matter in the rat cerebellum measured by scanning force microscopy", *Journal of Biomechanics*, vol. 43, no. 15, pp. 2986–2992, 2010, ISSN: 0021-9290. DOI: https://doi.org/10.1016/j.jbiomech.2010.07.002.

[108] N. Egawa, A. Shindo, A. C. Liang, Y. Du, C. Xing, E. K. Lo, K. Itoh, H. Kinoshita, T. Maki, R. Takahashi, R. Sudo, M. Spector, J. Lok, and K. Arai, "A novel three-dimensional culture system for oligodendrocyte precursor cells", *Stem Cells Dev*, vol. 26, no. 14, pp. 1078–1085, 2017, ISSN: 1547-3287. DOI: 10.1089/scd.2016.0306.

[109] K. M. Koss, M. A. Churchward, A. F. Jeffery, V. K. Mushahwar, A. L. Elias, and K. G. Todd, "Improved 3d hydrogel cultures of primary glial cells for in vitro modelling of neuroinflammation", *J Vis Exp*, no. 130, 2017, ISSN: 1940-087x. DOI: 10.3791/56615.

[110] E. J. Bradel and F. P. Prince, "Cultured neonatal rat oligodendrocytes elaborate myelin membrane in the absence of neurons", *J Neurosci Res*, vol. 9, no. 4, pp. 381–92, 1983, ISSN: 0360-4012 (Print)0360-4012. DOI: 10.1002/jnr.490090404.

[111] A. J. Treichel and J. H. Hines, "Development of an embryonic zebrafish oligodendrocyte-neuron mixed coculture system", *Zebrafish*, vol. 15, no. 6, pp. 586–596, 2018, ISSN: 1545-8547. DOI: 10.1089/zeb.2018.1625.

[112] Y. Pang, K. Simpson, J. J. Miguel-Hidalgo, and R. Savich, "Neuron/oligodendrocyte myelination coculture", *Methods Mol Biol*, vol. 1791, pp. 131–144, 2018, ISSN: 1064-3745. DOI: 10.1007/978-1-4939-7862-5_10.

[113] Z. Chen, Z. Ma, Y. Wang, Y. Li, H. Lu, S. Fu, Q. Hang, and P.-H. Lu, "Oligodendrocyte-spinal cord explant co-culture: An in vitro model for the study of myelination.", *Brain research*, vol. 1309, pp. 9–18, 2010, ISSN: 1872-6240 (Electronic). DOI: 10.1016/j.brainres.2009.10.060.

[114] H. Davis, M. Gonzalez, N. Bhargava, M. Stancescu, J. J. Hickman, and S. Lambert, "Rat cortical oligodendrocyte-embryonic motoneuron co-culture: An in vitro axon-oligodendrocyte interaction model.", *Journal of biomaterials and tissue engineering*, vol. 2, no. 3, pp. 206–214, 2012, ISSN: 2157-9083 (Print).

[115] S. S. Rosenberg, E. E. Kelland, E. Tokar, A. R. De la Torre, and J. R. Chan, "The geometric and spatial constraints of the microenvironment induce oligodendrocyte differentiation", *Proc Natl Acad Sci U S A*, vol. 105, no. 38, pp. 14 662–7, 2008, ISSN: 0027-8424. DOI: 10.1073/pnas.0805640105.

[116] S. Javid, A. Rezaei, and G. Karami, "A micromechanical procedure for viscoelastic characterization of the axons and ecm of the brainstem", *J Mech Behav Biomed Mater*, vol. 30, pp. 290–9, 2014, ISSN: 1878-0180. DOI: 10.1016/j.jmbbm.2013.11.010.

[117] S. A. Redmond, F. Mei, Y. Eshed-Eisenbach, L. A. Osso, D. Leshkowitz, Y.-A. A. Shen, J. N. Kay, M. Aurrand-Lions, D. A. Lyons, E. Peles, and J. R. Chan, "Somatodendritic expression of jamx2 inhibits oligodendrocyte myelination", *Neuron*, vol. 91, no. 4, pp. 824–836, 2016, ISSN: 0896-6273. DOI: https://doi.org/10.1016/j.neuron.2016.07.021.

[118] Y. B. Lu, K. Franze, G. Seifert, C. Steinhäuser, F. Kirchhoff, H. Wolburg, J. Guck, P. Janmey, E. Q. Wei, J. Käs, and A. Reichenbach, "Viscoelastic properties of individual glial cells and neurons in the cns", in *Proc Natl Acad Sci U S A*. 2006, vol. 103, pp. 17 759–64, ISBN: 0027-8424 (Print)1091-6490 (Electronic). DOI: 10.1073/pnas.0606150103.

[119] M. L. Fanarraga, I. R. Griffiths, M. Zhao, and I. D. Duncan, "Oligodendrocytes are not inherently programmed to myelinate a specific size of axon", *J Comp Neurol*, vol. 399, no. 1, pp. 94–100, 1998, ISSN: 0021-9967 (Print) 0021-9967.

[120] K. Susuki, "Myelin: A specialized membrane for cell communication.", *Nature Education*, vol. 3, no. 9, p. 59, 2010. [Online]. Available: https://www.nature.com/scitable/topicpage/myelin-a-specialized-membrane-for-cell-communication-14367205.

[121] D. Liewald, R. Miller, N. Logothetis, H.-J. Wagner, and A. Schüz, "Distribution of axon diameters in cortical white matter: An electron-microscopic study on three human brains and a macaque", *Biological cybernetics*, vol. 108, no. 5, pp. 541–557, 2014, ISSN: 1432-0770 0340-1200. DOI: 10.1007/s00422-014-0626-2.

[122] S. Torino, B. Corrado, M. Iodice, and G. Coppola, "Pdms-based microfluidic devices for cell culture", *Inventions*, vol. 3, no. 3, p. 65, 2018, ISSN: 2411-5134. [Online]. Available: https://www.mdpi.com/2411-5134/3/3/65.

[123] M. J. Owen, "Elastomers: Siloxane", in *Encyclopedia of Materials: Science and Technology*, K. H. J. Buschow, R. W. Cahn, M. C. Flemings, B. Ilschner, E. J. Kramer, S. Mahajan, and P. Veyssière, Eds. Oxford: Elsevier, 2001, pp. 2480–2482, ISBN: 978-0-08-043152-9. DOI: https://doi.org/10.1016/B0-08-043152-6/00448-4.

[124] I. D. Johnston, D. K. McCluskey, C. K. L. Tan, and M. C. Tracey, "Mechanical characterization of bulk sylgard 184 for microfluidics and microengineering", *Journal of Micromechanics and Microengineering*, vol. 24, no. 3, p. 035 017, 2014, ISSN: 0960-1317 1361-6439. DOI: 10.1088/0960-1317/24/3/035017.

[125] M. Buntinx, J. Vanderlocht, N. Hellings, F. Vandenabeele, I. Lambrichts, J. Raus, M. Ameloot, P. Stinissen, and P. Steels, "Characterization of three human oligodendroglial cell lines as a model to study oligodendrocyte injury: Morphology and oligodendrocyte-specific gene expression", *Journal of Neurocytology*, vol. 32, no. 1, pp. 25–38, 2003, ISSN: 1573-7381. DOI: 10.1023/a:1027324230923.

[126] Y. Chen, V. Balasubramaniyan, J. Peng, E. C. Hurlock, M. Tallquist, J. Li, and Q. R. Lu, "Isolation and culture of rat and mouse oligodendrocyte precursor cells", *Nat Protoc*, vol. 2, no. 5, pp. 1044–51, 2007, ISSN: 1750-2799. DOI: 10.1038/nprot.2007.149.

[127] K. D. McCarthy and J. de Vellis, "Preparation of separate astroglial and oligodendroglial cell cultures from rat cerebral tissue", *J Cell Biol*, vol. 85, no. 3, pp. 890–902, 1980, ISSN: 0021-9525 (Print)0021-9525. [Online]. Available: http://dx.doi.org/.

[128] R. Pandithage, *Brief introduction to critical point - application booklet*, Web Page, 2012. [Online]. Available: https://www.leica-microsystems.com/science-lab/brief-introduction-to-critical-point-drying/.

[129] H. H. Barber and H. F. Scobie, "Lange's handbook of chemistry. norbert adolph lange, editor", *The Journal of Physical Chemistry*, vol. 48, no. 5, pp. 308–309, 1944, ISSN: 0092-7325. DOI: 10.1021/j150437a011.

[130] H. Plasma, *Plasma treated pdms for improved bonding performance of microfluidic devices - application note*, Web Page. [Online]. Available: https://plasmatreatment.co.uk/henniker-plasma-technology/plasma-treatments/plasma-surface-activation-to-improve-adhesion/plasma-treatment-of-pdms/.

[131] D. R. Askeland and P. P. Phulé, *The science and engineering of materials (5th edition)*. 2006, ISBN: 978-0-534-55396-8.

[132] D. Wieczorek, L. Delauriere, and T. Schagat, *Methods of rna quality assessment (promega)*. [Online]. Available: https://worldwide.promega.com/resources/pubhub/methods-of-rna-quality-assessment/#abstract.

[133] I. BioRad Laboratories, *Real-time pcr applications guide*, 2006.

[134] F. Boucanova, A. F. Maia, A. Cruz, V. Millar, I. Mendes Pinto, J. B. Relvas, and H. S. Domingues, "Collar occupancy: A new quantitative imaging tool for morphometric analysis of oligodendrocytes", *J Neurosci Methods*, vol. 294, pp. 122–135, 2018, ISSN: 0165-0270. DOI: 10.1016/j.jneumeth.2017.11.014.

[135] X. Zhao, L. Li, B. Li, J. Zhang, and A. Wang, "Durable superhydrophobic/superoleophilic pdms sponges and their applications in selective oil absorption and in plugging oil leakages", *Journal of Materials Chemistry A*, vol. 2, no. 43, pp. 18 281–18 287, 2014, ISSN: 2050-7488. DOI: 10.1039/C4TA04406A.

[136] D. Corning, *Dow corning 360 medical fluid product information*, 2015.

[137] E. Carvalho, *Astrocyte-Oligodendrocyte Crosstalk in the Context of Astrogliosis*, Faculdade de Engenharia da Universidade do Porto, 2016.

[138] M. V. Sofroniew and H. V. Vinters, "Astrocytes: Biology and pathology", *Acta neuropathologica*, vol. 119, no. 1, pp. 7–35, 2010, ISSN: 1432-0533 0001-6322. DOI: 10.1007/s00401-009-0619-8.

[139] D. E. Korzhevskii and O. V. Kirik, "Brain microglia and microglial markers", *Neuroscience and Behavioral Physiology*, vol. 46, no. 3, pp. 284–290, 2016, ISSN: 1573-899X. DOI: 10.1007/s11055-016-0231-z.

[140] C. D. Katsetos, A. Legido, E. Perentes, and S. J. Mork, "Class iii beta-tubulin isotype: A key cytoskeletal protein at the crossroads of developmental neurobiology and tumor neuropathology", *J Child Neurol*, vol. 18, no. 12, 851–66; discussion 867, 2003, ISSN: 0883-0738 (Print) 0883-0738. DOI: 10.1177/088307380301801205.

[141] M. Fumagalli, S. Daniele, D. Lecca, P. Lee, C. Parravicini, R. Douglas Fields, P. Rosa, F. Antonucci, C. Verderio, L. Trincavelli, P. Bramanti, C. Martini, and M. Abbracchio, "Phenotypic changes, signaling pathway, and functional correlates of gpr17-expressing neural precursor cells during oligodendrocyte differentiation", *The Journal of biological chemistry*, vol. 286, pp. 10 593–604, 2011. DOI: 10.1074/jbc.M110.162867.

[142] S. A. Bustin, V. Benes, J. A. Garson, J. Hellemans, J. Huggett, M. Kubista, R. Mueller, T. Nolan, M. W. Pfaffl, G. L. Shipley, J. Vandesompele, and C. T. Wittwer, "The miqe guidelines: Minimum information for publication of quantitative real-time pcr experiments", *Clinical Chemistry*, vol. 55, no. 4, pp. 611–622, 2009. DOI: 10.1373/clinchem.2008.112797.

[143] K. Nelissen, K. Smeets, M. Mulder, J. J. Hendriks, and M. Ameloot, "Selection of reference genes for gene expression studies in rat oligodendrocytes using quantitative real time pcr", *J Neurosci Methods*, vol. 187, no. 1, pp. 78–83, 2010, ISSN: 0165-0270. DOI: 10.1016/j.jneumeth.2009.12.018.

[144] M. Liu, J. Sun, Y. Sun, C. Bock, and Q. Chen, *Thickness-dependent mechanical properties of polydimethylsiloxane membranes*. 2009, vol. 19, p. 035 028. DOI: 10.1088/0960-1317/19/3/035028.

[145] T. W. Hsiao, P. A. Tresco, and V. Hlady, "Astrocyte spreading and migration on aggrecan-laminin dot gradients", *Biointerphases*, vol. 13, no. 1, 01A401–01A401, 2017, ISSN: 1559-4106 1934-8630. DOI: 10.1116/1.5001675.

[146] W. Ma, T. Tavakoli, E. Derby, Y. Serebryakova, M. S. Rao, and M. P. Mattson, "Cell-extracellular matrix interactions regulate neural differentiation of human embryonic stem cells", *BMC developmental biology*, vol. 8, pp. 90–90, 2008, ISSN: 1471-213X. DOI: 10.1186/1471-213X-8-90.

[147] R. Milner and I. L. Campbell, "The extracellular matrix and cytokines regulate microglial integrin expression and activation", *The Journal of Immunology*, vol. 170, no. 7, pp. 3850–3858, 2003. DOI: 10.4049/jimmunol.170.7.3850.

[148] W. Y. Tam, N. P. B. Au, and C. H. E. Ma, "The association between laminin and microglial morphology in vitro", *Scientific Reports*, vol. 6, p. 28 580, 2016. DOI: 10.1038/srep28580.

[149] M. M. Azevedo, H. S. Domingues, F. P. Cordelières, P. Sampaio, A. I. Seixas, and J. B. Relvas, "Jmy regulates oligodendrocyte differentiation via modulation of actin cytoskeleton dynamics", *Glia*, vol. 66, no. 9, pp. 1826–1844, 2018, ISSN: 0894-1491. DOI: 10.1002/glia.23342.

Appendix A

Introductory Course in Laboratory Animal Science

The next two pages include the certificate obtained in the Introductory Course in Laboratory Animal Science, which includes Functions (A) and (D) - Mice and Rats Species specific, according to Directive 2010/63/EU. This data complements information presented in Chapter 3.

Certificate

INTRODUCTORY COURSE

LABORATORY ANIMAL SCIENCE

This is to certificate that, **Helena Isabel Soares de Paiva Ferreira** has successfully completed the Introductory Course in Laboratory Animal Science, 23nd edition, held on October 2018- January 2019, at i3S - Instituto de Investigação e Inovação em Saúde. Functions (A) and (D) - Mice and Rats species specific, according to Directive 2010/63/EU, are covered through theoretical and practical course components.

Course Contents
30 hours course, including theoretical and practical classes, which cover the following topics:

- Basic Biology and Husbandry
- The Animal Facility
- Animal Welfare
- Signs of ill-health
- Handling, basic techniques and minor procedures
- Anesthesia, analgesia and basic principles of surgery
- Ethics, 3Rs and Legislation
- Data collection and scientific validity
- Occupational health and safety

10 hours experimental practice with tutor

Organized in collaboration between i3S Animal Facility and i3S Advanced Training Unit.

ADVANCED TRAINING UNIT
INSTITUTO DE INVESTIGAÇÃO E INOVAÇÃO EM SAÚDE
UNIVERSIDADE DO PORTO

Andreia Costa
i3S Advanced Training Unit

Sofia Lamas
i3S Animal Facility

INSTITUTO DE INVESTIGAÇÃO E INOVAÇÃO EM SAÚDE
UNIVERSIDADE DO PORTO

Rua Alfredo Allen, 208
4200-135 Porto
Portugal
+351 220 408 800
info@i3s.up.pt
www.i3s.up.pt

i3S ADVANCED TRAINING UNIT | R. Alfredo Allen, 4200-135 Porto

INTRODUCTORY COURSE LABORATORY ANIMAL SCIENCE

COMPLEMENTARY INFORMATION

Modular structure - Training requirements under EU directive 2010/63/EU (Article 23 and Annex V)

Article 23-1functions:

A = person carrying out procedures on animals

D = person killing animals

TRAINING MODULES

Core Modules - Functions A, B, C & D

1 National legislation

2 Ethics, animal welfare and the Three Rs (level 1)

3.1 Basic and appropriate biology – species specific (theory)

4 Animal care, health and management – species specific (theory)

5 Recognition of pain, suff ering and distress - species specific

6.1 Humane methods of killing (theory)

Function Specific (Prerequisite) Modules - Function A

3.2 Basic and appropriate biology – species specific (practical)

7 Minimally invasive procedures without anaesthesia – species specific (theory)

8 Minimally invasive procedures without anaesthesia – species specific (skills)

Function Specific (Prerequisite) Modules - Function D

3.2 Basic and appropriate biology – species specific (practical)

6.2 Humane methods of killing (skills)

INSTITUTO DE INVESTIGAÇÃO E INOVAÇÃO EM SAÚDE
UNIVERSIDADE DO PORTO

Rua Alfredo Allen, 208
4200-135 Porto
Portugal
+351 220 408 800
info@i3s.up.pt
www.i3s.up.pt

Appendix B

RT-qPCR - Supplementary Information

Fig.B.1 and B.2 present an example of an Experion^{TM} analysis, with the final results report, obtained electropherogram and virtual gel report. This data complements information presented in Chapter 3.

Well ID	Sample Name	RNA Area	RNA Concentration (ng/µl)	Ratio [28S:18S]	RQI	RQI Classification	RQI Alert
L	Ladder	409.88	160.00				
1	1 eva	912.55	356.22	1.47	9.8	■	
2	2	871.69	340.27	1.71	9.9	■	
3	3	834.11	325.60	1.52	9.8	■	
4	4	951.04	371.25	1.69	9.9	■	
5	5	691.35	269.87	1.33	9.7	■	
6	6	1,141.75	445.70	1.75	10.0	■	
7	7	266.15	103.89	1.19	9.1	■	
8	8	98.86	38.59	1.36	9.1	■	
9	9	234.10	91.38	1.48	8.9	■	
10	10	122.17	47.69	1.50	8.6	■	
11	11	131.09	51.17	1.35	9.2	■	
12	12	364.16	142.16	1.26	8.6	■	

FIGURE B.1: Example of an Experion^{TM} analysis for assessment of RNA integrity. RQI values vary between 1 (degraded RNA) and 10 (intact sample). Samples with a RQI higher than 7 have RNA of acceptable quality, and were used for analysis of gene expression.

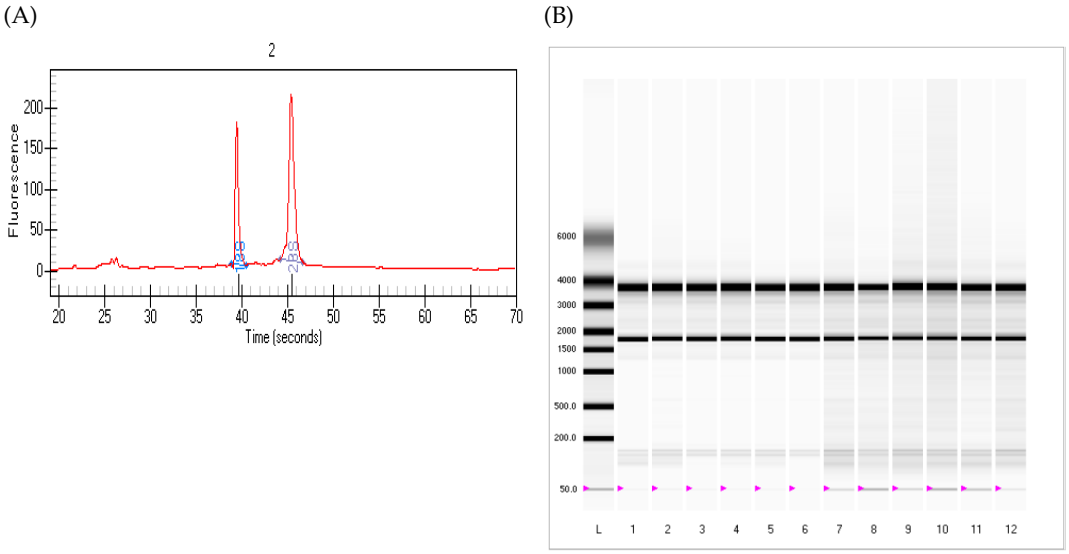


FIGURE B.2: Example of an (A) eletropherogram and (B) virtual gel report obtained from an Experion^{TM} analysis. The electropherogram shows the 18S and 28S rRNA bands - the 28S/18S intensity ratio is used as a measurement for RNA integrity.

Table B.1 presents sequences for all tested primers. Fig. B.3 correspond to amplification curves and standard curves for MBP, YWHAZ and 18S, and Table B.2 presents the information of amplification efficiency obtained from standard curves for each gene. 18S was later excluded from analysis due to great variations in expression between samples. This data complements information presented in Chapter 3.

TABLE B.1: MB, YWHAZ and 18S sense and anti-sense primers' sequences.

Gene	Primer	Sequence
MBP	Sense	5' TGT CAC AAT GTT CTT GAA GAA 3'
	Anti-sense	5' GCT CCC TGC CCC AGA AGT 3'
YWHAZ	Sense	5' ACG ACG TAC TGT CTC TTT TGG 3'
	Anti-sense	5' GTA TGC TTG CTG TGA CTG GT 3'
18S	Sense	5' GTA ACC GCT TGA ACC CCA TT 3'
	Anti-sense	5' CCA TCC AAT CGG TAG TAG CG 3'

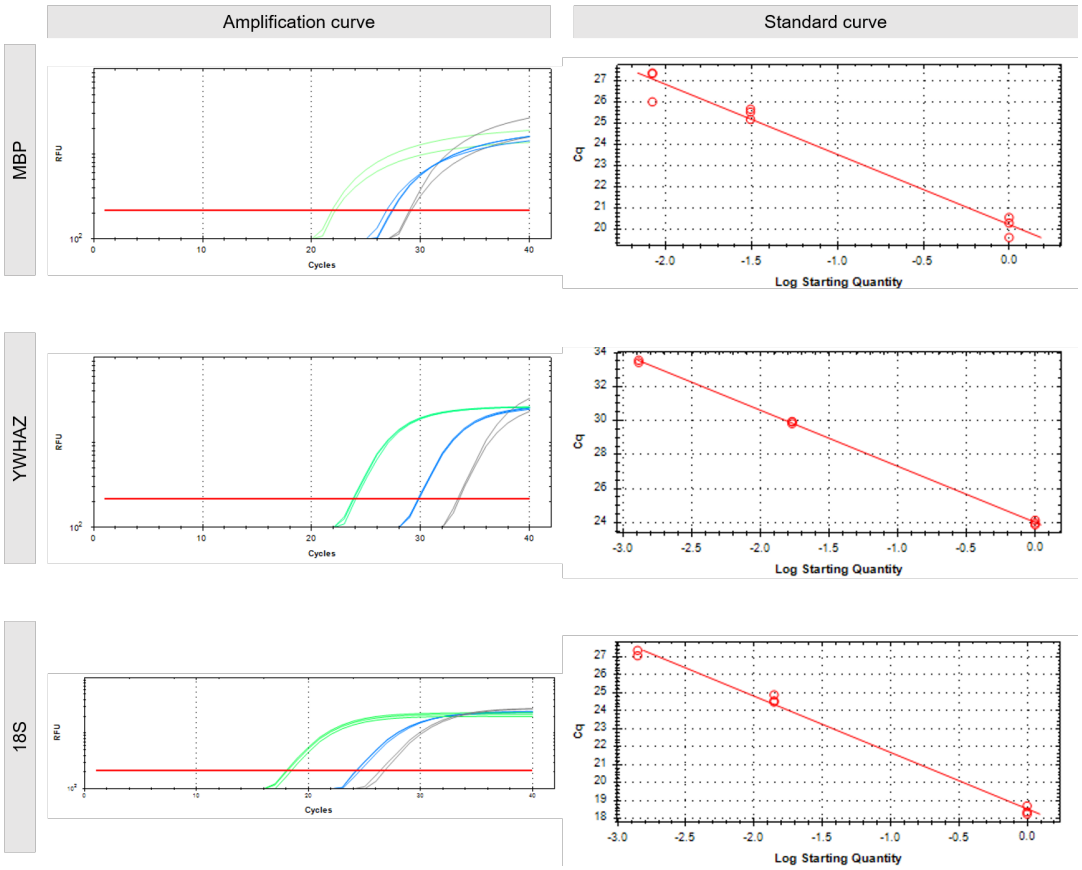


FIGURE B.3: Amplification curves and standard curves of tested primers (MBP, YWHAZ and 18S, as indicated) at 55ºC (annealing temperature). Amplification curves for non-template controls (red lines) and wells with cDNA from stock concentration (green lines), 1:10 dilution (blue lines) and 1:100 dilution (grey lines).

TABLE B.2: Amplificaiton efficiency, R^2, slope and y-intercept obtained from standard curves of tested primers (MBP, YWHAZ and 18S).

Gene	Amplification Efficiency (%)	r^2	Slope	y-Intercept
MBP	101.0%	0.973	-3.298	20.245
YWHAZ	100.8%	0.999	-3.303	24.006
18S	108.4%	0.994	-3.136	18.544

Appendix C

Evaluation of the purity of OPC cultures – Image analysis process

In order to evaluate the purity of OPC cultures, the presence of astrocytes, microglia and neurons was determined, by means of quantification of GFAP$^+$, IBA-1$^+$ and βIII tubulin$^+$, respectively (as described in Section 4.3).

In the following section, the image analysis process for identification and quantification of GFAP$^+$ cells (a marker for reactive astrocytes) is explored and illustrated with a representative image (Fig. 4.9(B), Chapter 4). This process includes image analysis with CellProfiler and object classification using CellProfiler Analyst.

Similarly, a pipeline was also developed for identification and quantification of IBA-1$^+$ and βIII tubulin$^+$ cells (microglia and neuronal markers, respectively), as presented in the final section.

C.1 Identification and quantification of GFAP$^+$ cells using CellProfiler and CellProfiler Analyst

The CellProfiler pipeline developed for this goal is composed of various modules, namely:

1. Identify Primary Objects;
2. Identify Secondary Objects;
3. Overlay Outlines;
4. Measure Object Intensity.

Identify Primary Objects

The first module aims to identify nuclei as primary objects (i.e. regions of interest as points of reference). The DAPI channel images are used as the input images, and the objects to be identified are named "Nuc". Only objects with a diameter within the 7-40 pixel units range are considered. Objects outside this diameter range are discarded, which allows for the exclusion of fluorescent debris. The diameter range was determined by visual inspection. Objects touching the border of the image (i.e. fractions of nuclei) are discarded as well.

Next, it is necessary to determine the thresholding method, that defines which pixels are considered from the "DNA" images to compose the Nuc objects. In other words, the pipeline performs an image binarization, converting greyscale images into binary (black and white) images, only with foreground and background. Here, the Otsu's method was used, for a two-class thresholding. The objective of the Otsu's method is to find the intensity threshold value that minimizes intraclass intensity variance (or equivalently, maximizes interclass variance). In order to smoothen the

DNA image before the Otsu's threshold is applied, a threshold smoothing scale of 1.3488 is applied. Smoothing of the input image removes holes and irregular edges caused by noise, therefore improving the uniformity of the ouput image and Nuc objects.

In case the pipeline identifies multinuclear objects (when the images have cell aggregates), it is possible to distinguish between nuclei that are touching each other using a declumping method. In this case, declumping was performed based on object shape. Because nuclei are round, the area where they touch each other is "thinner" than the typical diameter. Therefore, multinuclear objects can be identified by the presence of indentations and separated in this region. The pipeline automatically calculates a smoothing filter for the declumping (applied after Otsu's thresholding, and, therefore, different from the aforementioned thresholding smoothing scale). The minimum allowed distance between local intensity maxima to assist in declumping is also automatically determined – local intensity maxima that are closed than the minimum distance are suppressed and considered part of the same object. Finally, holes present in the image (i.e. regions of background surrounded by one or more objects) are filled after both thresholding and declumping, generating more uniform Nuc objects.

Using the DNA image as an input, the result of this module is represented in Fig. C.1(B).

Identify Secondary Objects

The second module aims to identify secondary objects named "NucExp". DNA images are the input images, and these secondary objects are identified using the primary objects as a reference.

The selected method to identify the secondary objects from the Nuc objects was "Distance – N". In this method, the edges of the primary objects (Nuc) are simply expanded by 5 pixels to create the secondary objects (NucExp). Once again, the holes of the NucExp objects are filled. However, in this case, secondary objects touching the border of the image were maintained for analysis.

The output of this module are the NucExp objects, which represent the perinuclear cytoplasm, as represented in Fig. C.1(C).

Overlay Outlines

In order to visualize the relation between the Nuc and NucExp objects, this module creates an image by overlaying the outlines of both objects. Fig. C.1(D) shows the Nuc outlines in blue and NucExp outlines in green.

Measure Object Intensity

In order to classify a cell as positive or negative for the expression of GFAP, it is necessary to measure the intensity of this marker in the NucExp objects (since this is, in fact, a cytoplasmic protein). Therefore, the GFAP channel images are used as input grayscale images to measure the signal intensity in the NucExp objects' area.

Finally, an SQLite database file with all the metadata of interest is generated. Furthermore, a CellProfiler Analyst properties file is also created, which allows the user to open the database with CellProfiler Analyst for object classification. Namely, the NucExp objects are used as reference for locations of the properties file, so these are the objects that will be classified using CellProfiler Analyst in the next step.

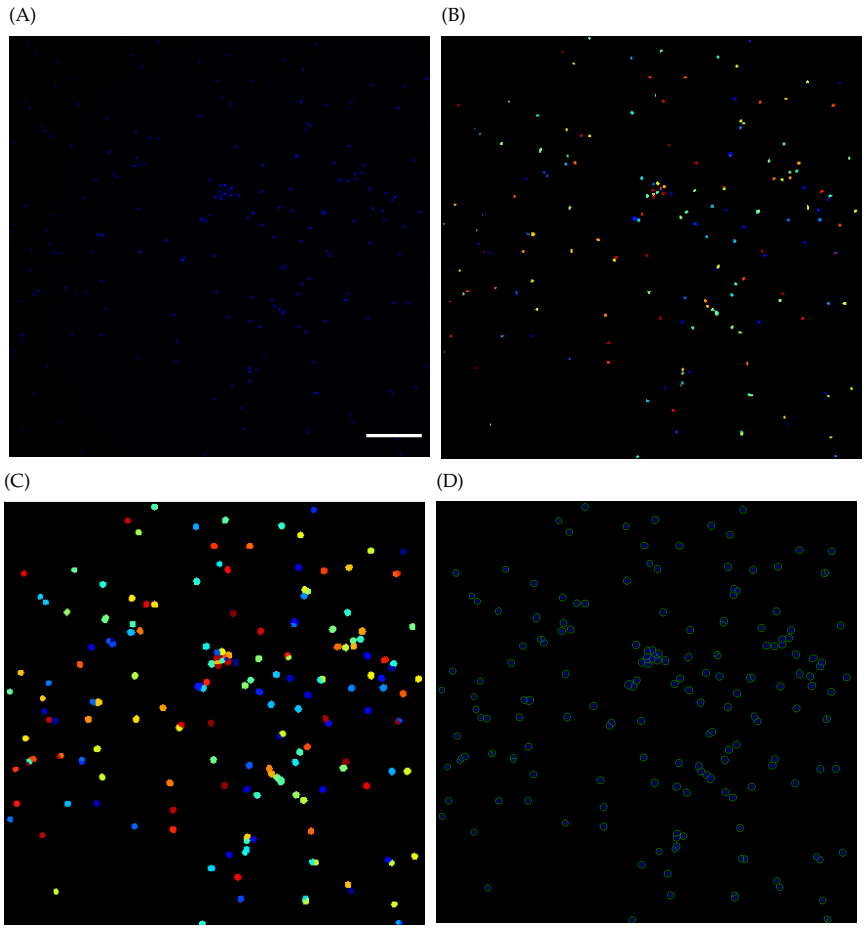


FIGURE C.1: Identification of Nuc and NucExp objects from original DAPI image. (A) Original DAPI channel image; (B) Nuc objects identified; (C) NucExp objects; (D) Overlay image of Nuc outlines (blue) and NucExp outlines (green). Scale bar: 100 µm.

Object classification with the Random Forest Classifier

In CellProfiler Analyst, the researcher classifies NucExp objects into one of various user-defined classes. In this case, the NucExp objects were classified into GFAP-positive or negative, based on a set of GFAP intensity features. The selected algorithm for object classification was the Random Forest Classifier. Random Forest is a supervised machine learning technique used for class prediction based on a multitude of decision trees.

A decision tree is a model that predicts the class/value of a target variable by learning a set of "if-then-else" decision rules inferred from input data features. However, single decision trees frequently overfit to their training set, increasing the variance of predictions. On the other hand, Random Forest models average multiple, uncorrelated decision trees to decrease variance and improve accuracy of predictions.

Fig. C.2 shows the confusion matrix and estimated accuracy of the obtained model, which are performance measurements.

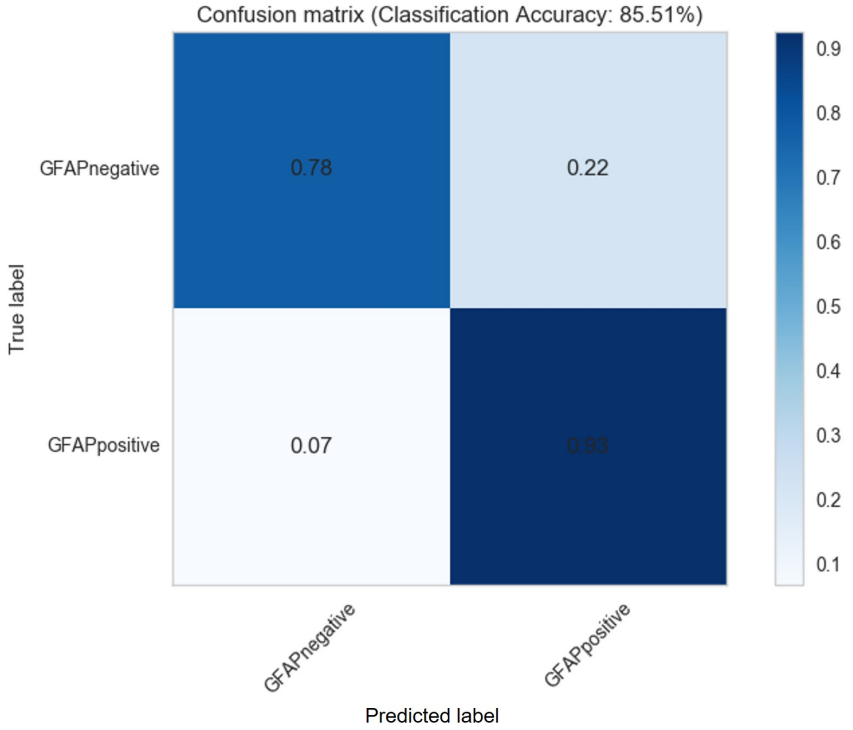


FIGURE C.2: Confusion matrix of the Random Forest algorithm trained for classification of objects into GFAP-positive and negative classes. Classification accuracy is estimated to be 85.51%.

C.2 Identification and quantification of IBA-1$^+$ and βIII tubulin$^+$ cells using CellProfiler and CellProfiler Analyst

The CellProfiler pipeline is similar to the one previously described, only with the exception that, in this case, both IBA1 and βIII tubulin channel images are used as input images to measure the signal intensity in the NucExp objects' area.

Concerning CellProfiler Analyst, the Random Forest Classifier was also used. However, three classes were defined for classification: NucExp objects could be classified as IBA1-positive, βIII tubulin-positive or double negative. Fig. C.3 shows the confusion matrix of the obtained model.

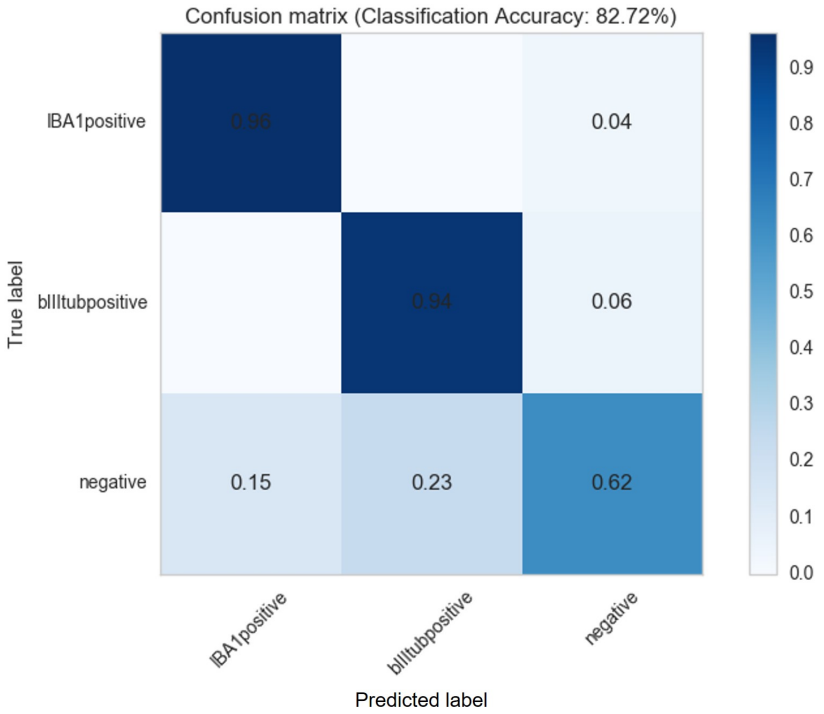


FIGURE C.3: Confusion matrix of the Random Forest algorithm trained for classification of objects into IBA1-positive, βIII tubulin-positive or double negative classes. Classification accuracy is estimated to be 82.72%.

Appendix D

Evaluation of OL differentiation stage – Image analysis process

In the following section, the image analysis process for classification of the differentiation stage of oligodendroglial cells will be explored and illustrated with an image (Fig. 4.15(A-C), Chapter 4). It includes pre-segmentation with ilastik, image analysis with CellProfiler and analysis of results with Microsoft Excel (as described in Section 4.4).

D.1 Image segmentation using ilastik

Before initiating the image analysis, images of the tubulin were segmented using ilastik. This pre-segmentation would create images with higher contrast, which would allow for easier identification of primary objects. The pixel classification workflow assigns labels to pixels based on pixel features and user annotations. Briefly, a set of features to be used in the classification is selected and the user paints the pixels in the images according to each label (class), creating a training set. A Random Forest classifier is then trained based on these user annotations. The output is an image with a probability map of each class, which can be transformed into individual objects afterwards using CellProfiler. In this case, the labels were positive or negative, so pixels could be classified as foreground or background. The output corresponded to grey scale images - the whiter the pixel, the higher the probability of being positive. Fig. D.1 shows the original tubulin channel image and segmented image.

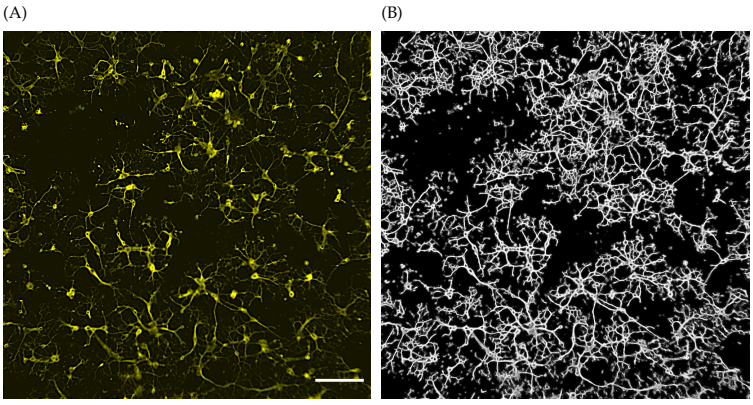


FIGURE D.1: Ilastik segmentation of tubulin channel images. (A) Original tubulin channel image; (B) Ilastik-segmented tubulin image. Scale bar: 100 µm.

D.2 Image analysis using CellProfiler

The CellProfiler pipeline developed for this goal is composed of various modules, namely:

1. Identify Primary Objects (Nuc);
2. Identify Secondary Objects (NucExp);
3. Identify Tertiary Objects (Collar);
4. Identify Primary Objects (Cell network);
5. Measure Object Size and Shape;
6. Filter Objects (Filtered Cell network);
7. Mask Objects (Collar mask);
8. Mask Objects (Protrusions in Collar);
9. Measure Object Size and Shape;
10. Measure Object Intensity;
11. Overlay Outlines.

Identify Primary Objects (Nuc) and Identify Secondary Objects (NucExp)

These modules aim to identify nuclei as primary objects (named "Nuc") using DAPI images and secondary objects (named "NucExp") by an expansion of Nuc objects. The process is the same as reported for similar modules on Appendix C, except that the expansion of Nuc objects to create the NucExp objects was by 12 pixels.

Identify Tertiary Objects (Collar)

The collar area corresponds to the peripherical area of the nucleus and, therefore, does not include the nucleus itself. The collar areas are created as tertiary objects, by "subtracting" the Nuc objects to the respective NucExp objects. The output objects are named "Collars" (Fig. D.2).

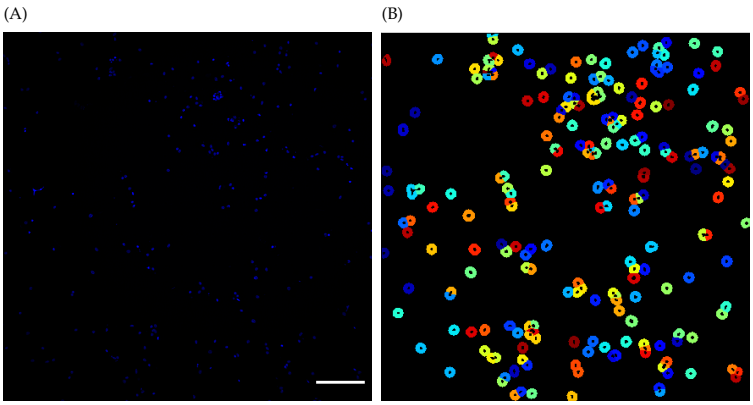


FIGURE D.2: Identification of Collar objects from Nuc and NucExp objects, which in turn are identified from DAPI channel images. (A) Original DAPI channel image; (B) Collar objects. Scale bar: 100 µm.

Identify Primary Objects (Cell network), Measure Object Size and Shape and Filter Objects (Filt

The aim of the first module is to identify the cellular network as primary objects. The input images are the ilastik-segmented tubulin channel images and the output objects are denominated “Cell network”. A manual thresholding method was adopted, and the thresholding intensity was set to 0.6. Importantly, in this case, the holes in the identified objects were not filled, so that cellular processes were well individualized (Fig. D.3(B)).

The area and form factor of the Cell network objects are measured and these objects are filtered according to an area threshold. This threshold had already been determined by the author. Cell network objects with an area below 10 probably correspond to cellular debris and are, therefore, excluded from analysis (Fig. D.3(C)).

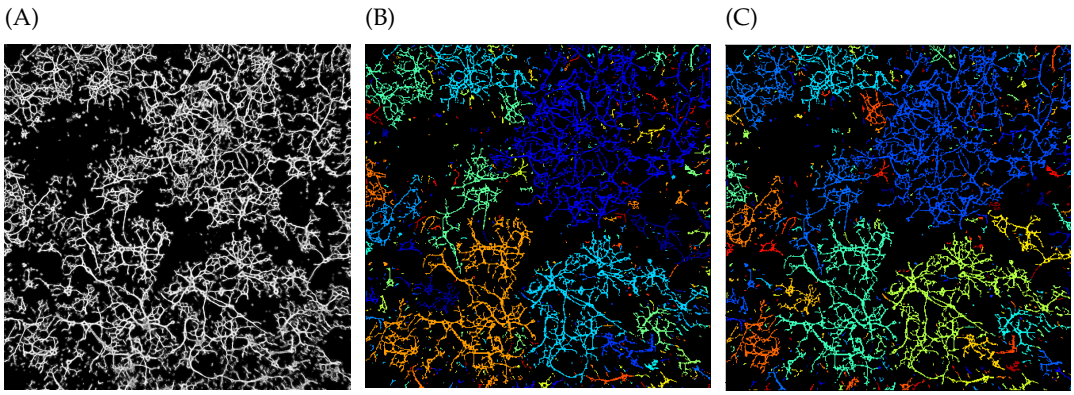


FIGURE D.3: Identification of Cell network objects from ilastik-segmented tubulin image. (A) Ilastik-segmented tubulin image; (B) Cell network objects; (C) Filtered cell network objects. Filtering using minimum area threshold (10). Scale bar: 100 µm.

Mask objects (Collar mask)

In order to consider only the tubulin processes inside the collar regions, it is necessary to mask the Filtered Cell network objects using the Collar objects as a mask. The output objects are denominated “Collar mask”. For objects that are only partially masked, the pipeline keeps the overlapping region (Fig. D.4(A)).

It is important to notice that two or more separate "Filtered Cell Network" objects that are included in the same collar are still considered two or more separate objects after this module.

Mask objects (Protrusions in Collar)

In order to calculate the total area occupied by protrusions inside a particular collar, those protrusions have to be labeled as the same object (which did not happen in the last module). To achieve that, it is necessary to mask the Collar objects using the Collar mask obtained in the previous module. The output objects are denominated “Protrusions in Collar”. For objects that are only partially masked, the pipeline keeps the overlapping region (Fig. D.4(B)).

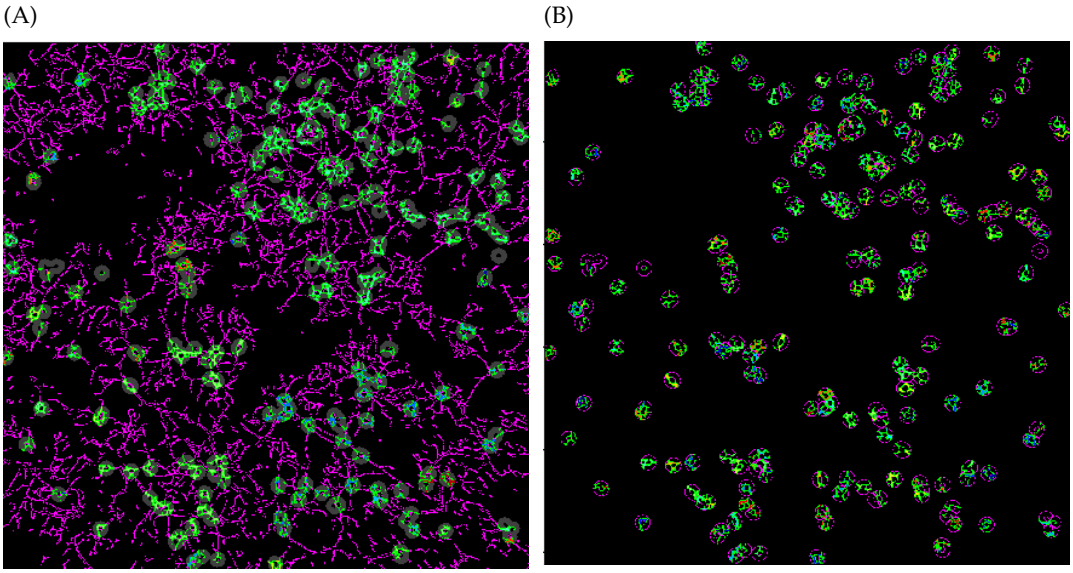


FIGURE D.4: Identification of Collar mask and Protrusions in Collar objects. (A) Collar mask objects, obtained by masking Filtered Cell network with Collar objects; (B) Protrusions in Collar objects, obtained by masking Collars with Collar mask. Green outlines indicate areas selected by the mask, while purple outlines indicate areas excluded by the mask.

Measure Object Size and Shape and Measure Object Intensity

In order to obtain more information about the Nuc, Collar and Protrusions in Collar objects - necessary to calculate collar occupancy for each cell - the area and form factor of each of these objects were measured.

So as to classify a cell as positive or negative for the expression of Olig2, it is necessary to measure the intensity of these markers in the Nuc and NucExp objects (since they are nuclear and cytoplasmic markers, respectively). Therefore, the Olig2 and MBP wix1 channel images are used as input grayscale images to measure the signal intensity in the Nuc and NucExp objects' area.

Overlay Outlines

In order to visualize the relation between the Nuc, Collar and Collar mask objects, this module creates an image by overlaying the outlines of these objects, using the ilastik-segmented tubulin image as background. Fig. D.5 shows Nuc, Collar and Collar mask objects' outlines in blue, yellow and green, respectively.

Finally, spreadsheets with all measurements of interest are created in the end of the pipeline. Results analysis proceeds in Microsoft Excel.

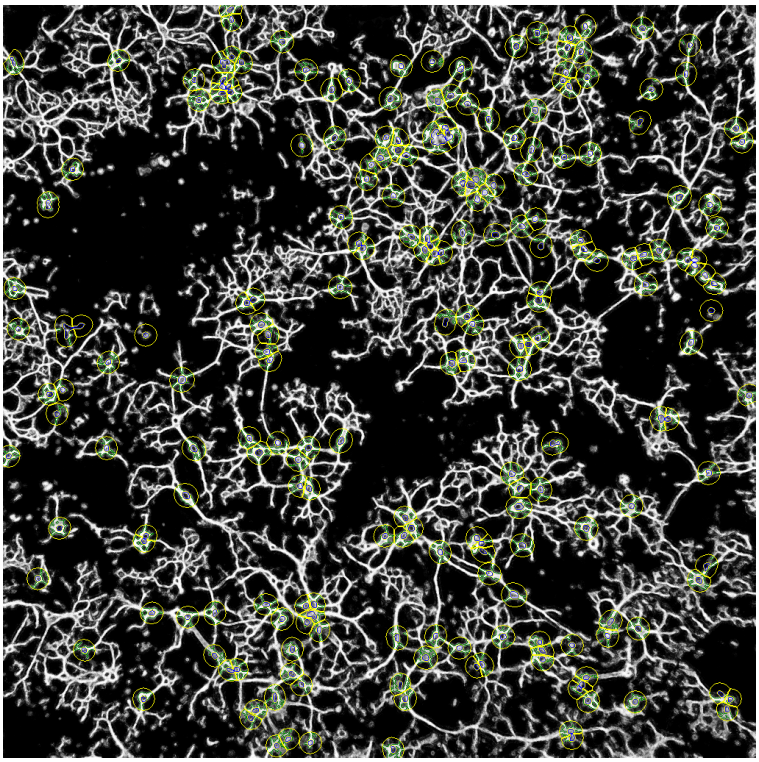


FIGURE D.5: Final overlay of Nuc (blue), Collar (yellow) and Collar mask (green) objects' outlines, using ilastik-segmented tubulin image as background.

D.3 Analysis of results using Microsoft Excel

Final analysis of results was performed following the same procedure as described in the original paper [134]. However, it was not possible to use the parameters provided in the paper (because those corresponded to the INCell Investigator software). Samples of one biological replicate were analyzed to determine these parameters, which were then applied to the remaining samples.

Firstly, it is necessary to select oligodendroglial cells. To do that, a threshold for the Olig2 mean intensity inside the Nuc objects was determined. Analyzing a histogram of Olig2 mean intensity values (Fig. D.6), it was possible to narrow down a range of values for the threshold. Indeed, it is possible to see two "populations" of objects: objects with an Olig2 mean intensity lower than 0.0028, which correspond to $Olig2^{-}$ nuclei, and a population with an apparently normal distribution. Analyzing this population, it was possible to establish, through visual inspection, a threshold intensity (0.003).

As suggested by Bouçanova and colleagues, not all cell can be considered for analysis of collar occupancy - it is necessary to select "well segmented" cells. In order to classify the differentiation stage of an oligodendrocyte based on the concept of collar occupancy, it is important to guarantee that the collar area is proportional to the nucleus area - in other words, that area in all directions of the nuclear peripheric region is considered. It is necessary to exclude binuclear objects, as well as cells in highly confluent areas, whose collar area is constricted by neighbour cells. To achieve that, a plot of collar area vs. nucleus area was analyzed (Fig. D.7). It is possible to observe a tendency line, corresponding to cells with a collar area proportional to the nucleus area. However, some cells out of this tendency line were

also considered. Through visual inspection, a range for both nuclear area and collar area was determined - cells inside these ranges (red rectangle in Fig. D.7) were considered well segmented and included in analysis.

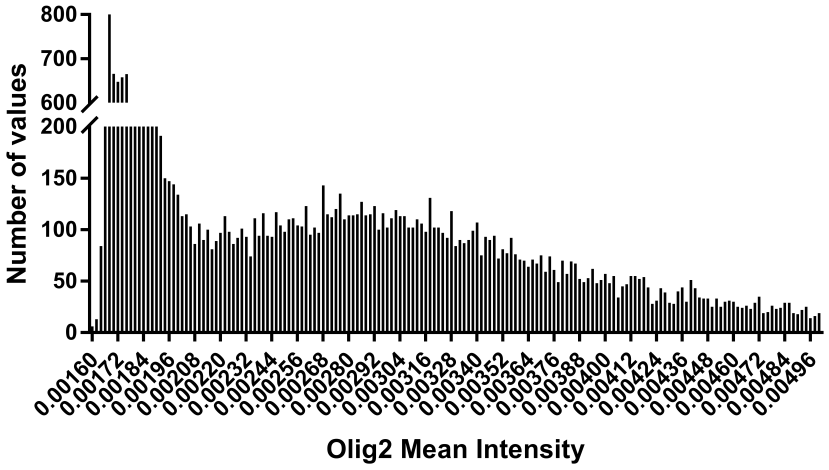


FIGURE D.6: Histogram of Olig2 mean intensity values (as detected in Nuc objects).

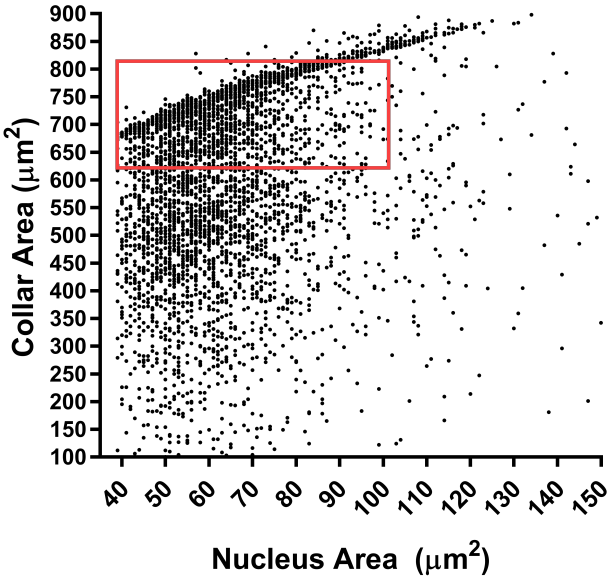


FIGURE D.7: Plot of collar area vs. nucleus area for each object. Values in μm^2. Rectangle includes well segmented cells, according to ranges determined for nucleus and collar areas. In the analyzed biological replicate, 4231 cells were considered well segmented, 64.6% from 6550 $Olig2^+$ cells.

Finally, it was necessary to establish new parameters of collar occupancy for classification of differentiation stages, which was done through visual inspection. Fig. 4.16 (in Chapter 4, Section 4.4) presents an example of each differentiation stage.

Table D.1 presents a summary of the analysis parameters used in this case.

TABLE D.1: Parameters used for analysis of the Collar Occupancy pipeline results. All parameters determined through visual inspection.

Classification	**Parameter**	**Value**
Olig2^{+} cells	Olig2 mean intensity in Nuc objects	$\geq$0.003
Well segmented cells	Nucleus area	39-100 μm^2
	Collar area	620-815 μm^2
Differetiation stage	Collar occupancy	
	Stage I	17-24 %
	Stage II	24-32 %
	Stage III	32-42 %
	Stage IV	$\geq$42 %

Appendix E

Evaluation of micropillars' wrapping – Image analysis process

In the following section, the image analysis process for quantification of percentage of MBP^+ cells, MBP area per MBP^+ cell, percentage of myelinated micropillars and number of myelinated micropillars per MBP^+ cell will be explored and illustrated with a representative image (Fig. 4.15(A),(B),(D-F), Chapter 4). This process includes pre-segmentation with ilastik, image analysis with CellProfiler and analysis of results using Microsoft Excel (as described in Section 4.4).

E.1 Image segmentation using ilastik

Before initiating the image analysis process using CellProfiler, images of the brightfield, MBP wix1 and MBP wix2 channels were segmented using ilastik. The selected features, process and outcome are similar to the pixel classification workflow previously described in Appendix D. Fig. E.1 shows the original image and segmented image, for brightfield, MBP wix1 and MBP wix2 channels, respectively.

E.2 Image analysis using CellProfiler

The developed CellProfiler pipeline is composed of various modules, namely:

1. Identify Primary Objects (Nuc);
2. Identify Secondary Objects (NucExp);
3. Measure Object Intensity;
4. Identify Primary Objects (MBPinFocus);
5. Measure Image Area Occupied;
6. Identify Primary Objects (Pillars);
7. Identify Secondary Objects (PillarsExp);
8. Measure Objects Size and Shape (PillarsExp);
9. Filter Objects (Area);
10. Measure Objects Size and Shape (FilterPillars);
11. Filter Objects (Shape);
12. Identify Primary Objects (MBPpillars);
13. Mask objects;
14. Overlay Outlines;
15. Measure Object Size and Shape (FinalPillars);
16. Relate Objects.

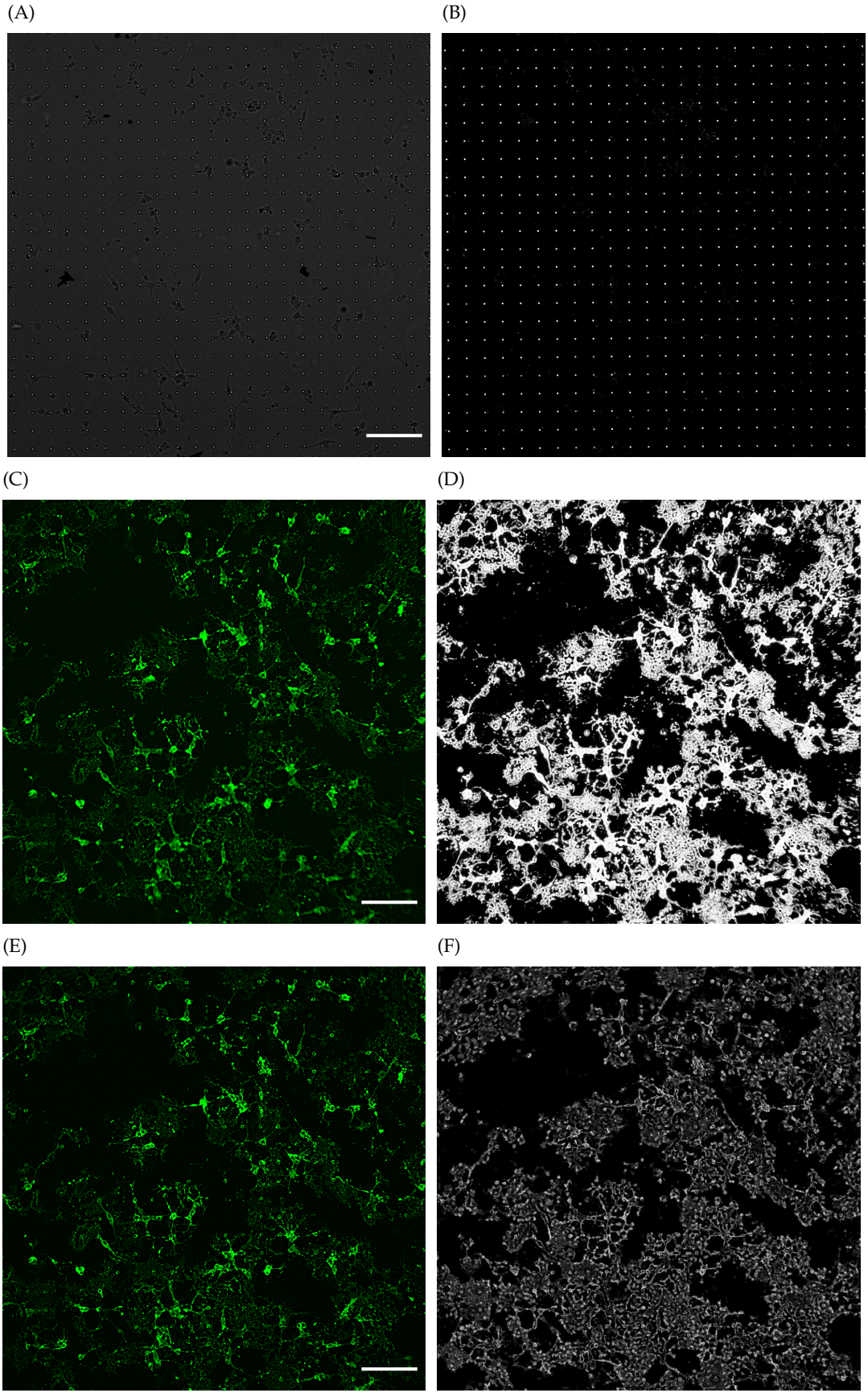


FIGURE E.1: Ilastik segmentation of (A) brightfield, (C) MBP wix1 and (E) MBP wix2 channel images. (A,C,E) Original images; (B,D,F) ilastik-segmented images. Scalebar: 100 µm.

Identify Primary Objects (Nucs) and Identify Secondary Objects (NucExp)

These modules aim to identify nuclei as primary objects (named “Nuc”) using DAPI images and secondary objects (named “NucExp”) by an expansion of Nuc objects. The process is the same as reported for similar modules on Appendix C.

Measure Object Intensity

In order to classify a cell as positive or negative for the expression of Olig2 and MBP, it is necessary to measure the intensity of these markers in the Nuc and NucExp objects (since they are nuclear and cytoplasmic markers, respectively). Therefore, the Olig2 and MBP wix1 channel images are used as input grayscale images to measure the signal intensity in the Nuc and NucExp objects’ area.

Identify Primary Objects (MBPinFocus) and Measure Image Area Occupied

This module aims to identify the MBP areas in focus as primary objects. The ilastik-segmented MBP wix1 images are used as input and the objects to be identified are named “MBPinFocus”. The program identifies objects that are typically in the 3-500 pixel units range, but objects outside this range are not excluded (because the maximum diameter is unknown). Objects touching the border of the image (i.e. fractions of cells) are also not discarded, since this would probably result in the loss of various cell areas important for quantification.

For image binarization, a manual threshold is applied, which guarantees that every image is treated identically. The manual threshold was defined as 0.5 through visual inspection. This threshold was set higher than the default value (0.2) because the ilastik-segmented input images already have a high contrast. No declumping was performed for this case. Fig. E.2 presents the identification of MBPinFocus objects from the ilastik-segmented MBP wix1 images.

After that, the total area occupied by the MBPinFocus objects in each image is determined. This information is later used to determine the MBP area per cell.

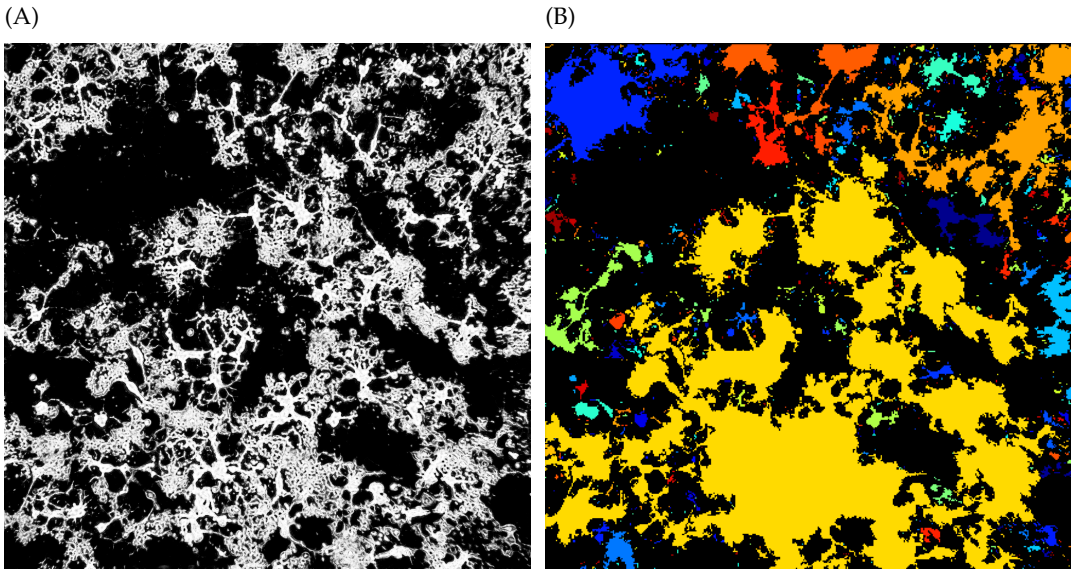


FIGURE E.2: Identification of MBPinFocus primary objects from ilastik-segmented MBP wix1 images. (A) Ilastik-segmented MBP wix1 image; (B) MBPinFocus primary objects. Image binarization was performed using a manual threshold of 0.5.

Identify Primary Objects (Pillars)

Similarly to the identification of Nuc objects, here micropillars are identified as primary objects. The ilastik-segmented brightfield images are used as input images, and the objects identified are named "Pillars". The program identifies objects that are typically in the 1-15 pixel units range. Objects outside this diameter range, as well as touching the border of the image, as excluded from analysis. Once again, a manual thresholding method is used, and the threshold was set for 0.4. Because micropillars are regularly interspaced, declumping was unnecessary. Fig. E.3(B) presents the identification of Pillars objects from the ilastik-segmented brightfield images.

Identify Secondary Objects (PillarsExp)

The identification of myelinated micropillars implies the establishment of a relationship between micropillars and myelin rings. This relationship could be of co-localization. For that, however, the micropillars need to be expanded in order to include the surrounding area where the myelin rings exist.

Therefore, secondary objects named "PillarsExp" are created. The Pillars objects are expanded by 2 pixels to create the secondary objects. Fig. E.3(C) presents the identification of PillarsExp objects from Pillars objects.

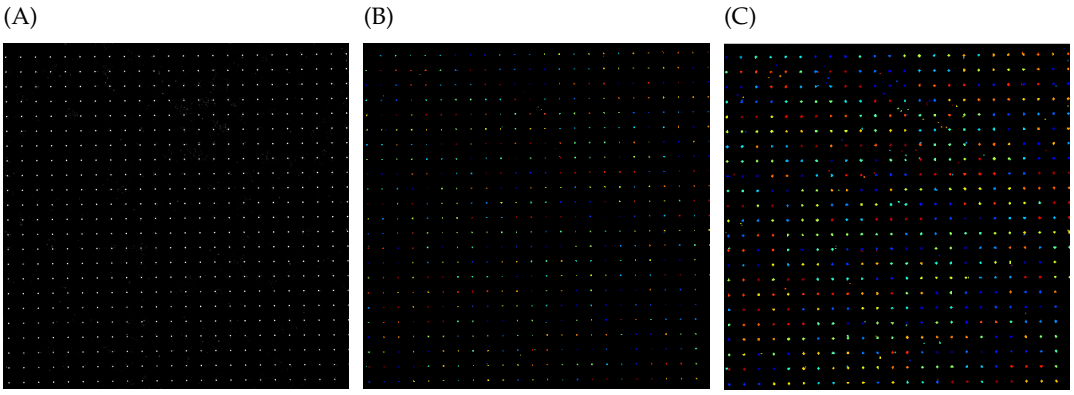


FIGURE E.3: Identification of Pillars primary objects from ilastik-segmented brightfield images and creation of PillarsExp secondary objects. (A) Ilastik-segmented brighfield images; (B) Pillars primary objects. Image binarization was performed using a manual threshold of 0.4; (C) PillarsExp secondary objects. Expansion by 2 pixels from the correspondent primary objects.

Measure Object Size and Shape (PillarsExp) and Filter Objects (Area)

In spite of the ilastik segmentation and manual thresholding, some debris are still erroneously identified as Pillars objects. In order to exclude debris, these pillars can be filtered according to different parameters.

The first filter to be applied is a filter concerning area. By visual inspection, the minimum area of a micropillar was determined (25). This value was carefully determined to avoid incorrect exclusion of 1 µm micropillars (whose area is closer to that of the debris).

Initially, the area of PillarsExp objects is determined. In the filtering module, PillarsExp objects are used as input and the output objects are named "FilterPillars". Objects with an area below 25 are excluded from analysis. It is important to mention

that this is applied to all diameters (from 1 to 5 µm micropillars), so the minimum value only excludes small debris. Fig. E.4(B) shows the FilterPillars objects.

Measure Object Size and Shape (FilterPillars) and Filter Objects (Shape)

The final filter to be applied is a filter concerning shape. By visual inspection, the minimum form factor of a micropillar was determined (0.7). Because micropillars are round, their form factor is close to 1. Therefore, objects below the established threshold correspond to "thinner" objects, with a more irregular shape, and are probably debris.

Initially, the form factor of FilterPillars objects is determined. In the filtering mode, the input objects are the FilterPillars objects, and the output objects are named "FinalPillars". Only objects with a form factor above 0.7 are considered for analysis. Fig. E.4(C) shows the FinalPillars objects.

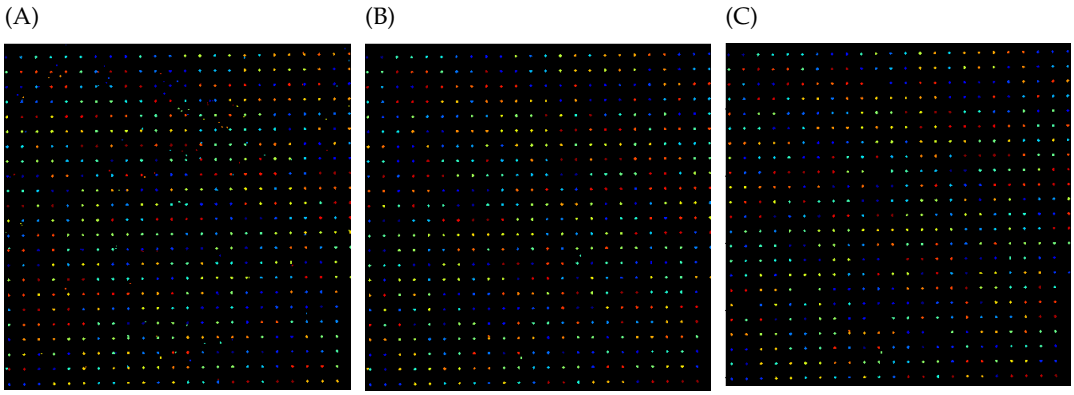


FIGURE E.4: Filtering of PillarsExp according to area and form factor and identification of FilterPillars and FinalPillars objects. (A) PillarsExp secondary objects; (B) FilterPillars objects. Filtering using area minimum threshold (25); (C) FinalPillars objects. Filtering using minimum form factor threshold (0.7).

Identify Primary Objects (MBPpillars)

The aim of this module is to identify the myelin rings as primary objects. The ilastik-segmented MBP wix2 images are used as the input images, and the objects identified are named "MBPpillars". The program identifies objects that are typically in the 3-300 pixel units range. Objects outside this diameter range are excluded from analysis.

Once again, a manual thresholding method is used, and the threshold was set for 0.3. This particular threshold was difficult to determine. The ilastik segmentation of MBP wix2 channel images revealed various uncertainty pixels due to the complexity of the images. This translated into more grey pixels in the ilastik-segmented image, therefore making the threshold harder to determine. It was eventually set at 0.3, a threshold that ensured that all myelin rings were included but left out most of the background signal. Fig. E.5 shows the identification of MBPpillars primary objects from the ilastik-segmented MBP wix2 image.

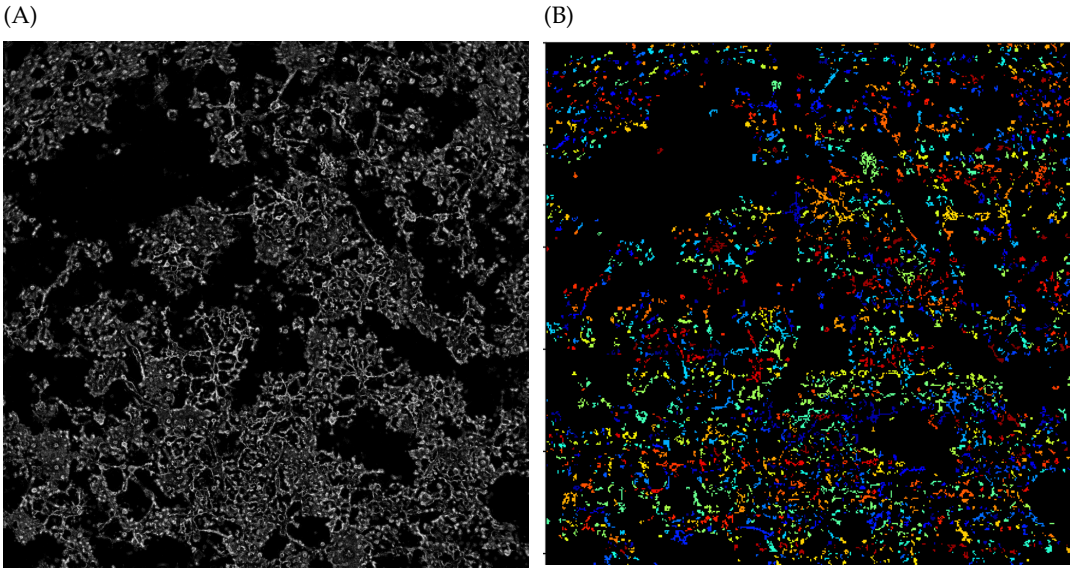


FIGURE E.5: Identification of MBPpillars primary objects from ilastik-segmented MBP wix2 channel images. (A) Ilastik-segmented MBP wix2 image; (B) MBPpillars primary objects. Image binarization was performed using a manual threshold of 0.3.

Mask Objects, Overlay Outlines and Measure Object Size and Shape

In order to consider only the MBP signal that corresponded to myelin rings, i.e. MBP signal around micropillars, it is necessary to mask these objects (MBPpillars) using the FinalPillars objects as a mask. The output objects are named "MBPinPillars". Importantly, for objects that are only partially masked, the pipeline keeps the overlapping region.

In order to visualize the relation between the FinalPillars and MBPinPillars objects, the following module creates an image by overlaying the outlines of both objects, using the ilastik-segmented MBP wix2 image as background. Fig. E.6 shows the FinalPillars outline in red and the MBPinPillars outline in green.

The last module is used to determine the area and form factor of FinalPillars and MBPinPillars objects, information used for further analysis.

Relate Objects

Lastly, it is still necessary to relate both the aforementioned objects. Here, the parent objects (i.e. the objects that encompass the child objects) are defined as the FinalPillars, while the child objects (i.e. the objects that are included inside the parent objects) are defined as the MBPinPillars. Therefore, each FinalPillar parent object has one or more MBPinPillar child objects. The output objects are denominated "PillarsWithMBP". Also, per-parent mean values of measurements made in the children objects were calculated and stored for the parent FinalPillar.

Finally, spreadsheets with all measurements of interest are created in the end of the pipeline. Results analysis proceeds in Microsoft Excel.

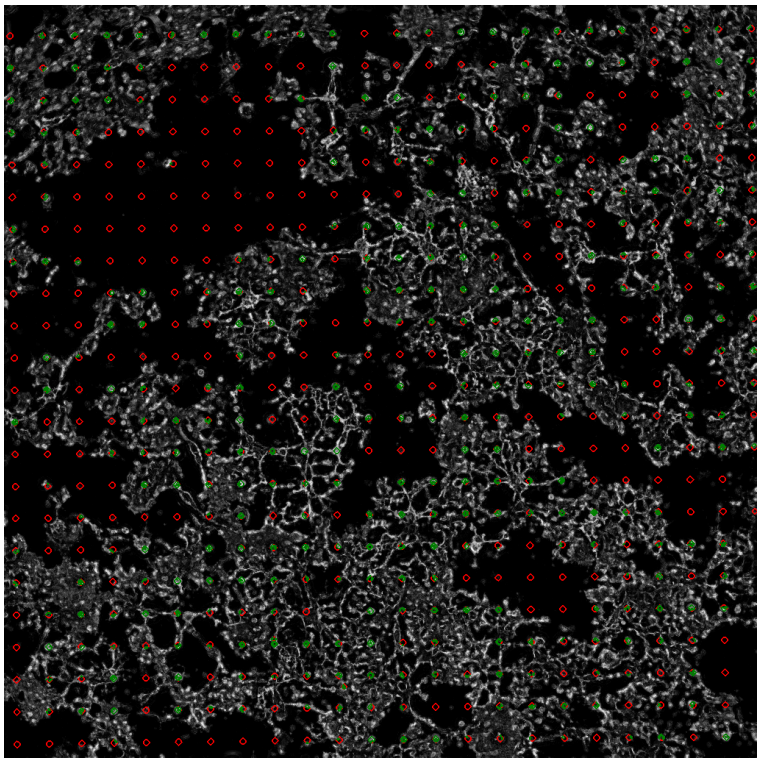


FIGURE E.6: Final overlay of MBPinPillars (green) and FinalPillars (red) objects' outlines, using the ilastik-segmented MBP wix2 image as background.

E.3 Analysis of results using Microsoft Excel

Firstly, it was necessary to determine the Olig2$^+$ cells, which was done using the same method as described in Appendix D. It was then necessary to determine the number of MBP$^+$ cells, which was done using a similar procedure. A histogram of MBP mean intensity inside NucExp objects was done and a threshold (0.002) was determined through visual inspection (Fig. E.7).

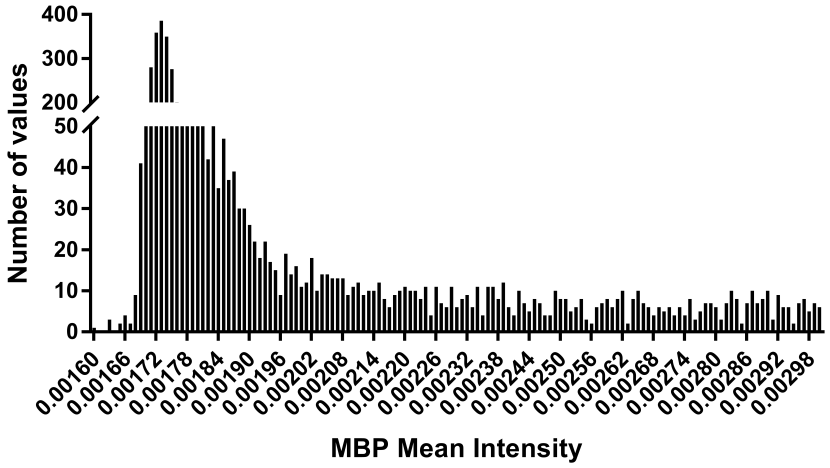


FIGURE E.7: Histogram of MBP mean intensity values (as detected in NucExp objects).

Afterwards, the counting of myelinated micropillars was performed using the

parent-child relation between FinalPillars and MBPinPillars. Because of the previously mentioned problem of possibly finding two or more MBPinPillars objects inside a single FinalPillar object, it was not possible to simply count the total number of MBPinPillars objects for each image. Instead, the number of myelinated micropillars was determined as the number of FinalPillars objects with an attributed child object (i.e. micropillars that had at least one object of MBPinPillars).

Table E.1 presents a summary of the analysis parameters used in this case.

TABLE E.1: Parameters used for analysis of the Myelinated Micropillars pipeline results. All parameters determined through visual inspection.

Classification	**Parameter**	**Value**
Olig2$^+$ cells	Olig2 mean intensity in Nuc objects	$\geq$0.003
MBP$^+$ cells	MBP mean intensity in NucExp objects	$\geq$0.002
Myelinated micropillars	FinalPillars objects	FinalPillars objects with $\geq$1 child MBPinPillars objects

Appendix F

Evaluation of the purity of OPC cultures – Quantitative data

Tables F.1 and F.2 present the average percentages of GFAP$^+$, IBA1$^+$ and βIII tubulin$^+$ cells and estimation of OPC purity in OPC cultures on control PDMS platforms, for days 1 and 5, respectively. This data complements information presented in Section 4.3.

TABLE F.1: Quantification of GFAP$^+$, IBA1$^+$ and βIII tubulin$^+$ cells and estimation of OPC purity in OPC cultures on control PDMS platforms, at diff. day 1. Percentage of oligodendroglial cells calculated as the difference between 100% and the sum of average values for GFAP$^+$, IBA1$^+$ and βIII tubulin$^+$ cells. Values correspond to percentage of cells, indicated as mean$\pm$SD. n=3 independent experiments, 2-4 technical replicates per diameter.

	Day 1			
Substrate	GFAP$^+$ cells	IBA1$^+$ cells	βIII tubulin$^+$ cells	OLs
1 µm	10.9$\pm$11.9	7.1$\pm$2.1	8.4$\pm$2.7	73.5
2 µm	4.9$\pm$1.5	7.9$\pm$2.3	8.5$\pm$3.8	78.7
3 µm	6.4$\pm$4.4	8.9$\pm$2.4	12.2$\pm$4.4	72.5
4 µm	5.4$\pm$1.7	10.8$\pm$4.0	10.9$\pm$4.3	72.8
5 µm	6.6$\pm$1.6	9.2$\pm$3.2	11.3$\pm$6.2	72.9
Flat surface	6.5$\pm$3.7	5.5$\pm$2.7	8.2$\pm$3.9	79.8
TCPS	1.8$\pm$0.8	0.0$\pm$0.0	0.0$\pm$0.0	98.2

TABLE F.2: Quantification of GFAP$^+$, IBA1$^+$ and βIII tubulin$^+$ cells and estimation of OPC purity in OPC cultures on control PDMS platforms, at diff. day 5. Percentage of oligodendroglial cells calculated as the difference between 100% and the sum of average values for GFAP$^+$, IBA1$^+$ and βIII tubulin$^+$ cells. Values correspond to percentage of cells, indicated as mean$\pm$SD. n=3 independent experiments, 2-4 technical replicates per diameter.

	Day 5			
Substrate	GFAP$^+$ cells	IBA1$^+$ cells	βIII tubulin$^+$ cells	OLs
1 µm	8.0$\pm$4.4	11.1$\pm$8.3	4.6$\pm$3.2	76.3
2 µm	11.5$\pm$3.2	14.2$\pm$12.4	5.1$\pm$4.0	69.2
3 µm	11.4$\pm$4.6	7.0$\pm$2.5	5.2$\pm$3.3	76.4
4 µm	11.8$\pm$4.9	6.2$\pm$1.3	5.5$\pm$2.5	76.5
5 µm	10.2$\pm$2.4	6.5$\pm$5.6	11.2$\pm$0.3	72.2
Flat surface	10.3$\pm$4.0	22.3$\pm$19.0	6.1$\pm$5.3	61.3
TCPS	7.5$\pm$3.6	0.0$\pm$0.0	0.0$\pm$0.0	92.5

Appendix G

Effect of physical cues on OPC differentiation and myelination - Comparison between timepoints

Fig. G.1 and G.2 present results of all the outputs included for the assessment of the effect of micropillar presence and substrate stiffness on OPC differentiation and micropillars' wrapping, for control and soft PDMS, respectively. This data complements information presented in Section 4.4.

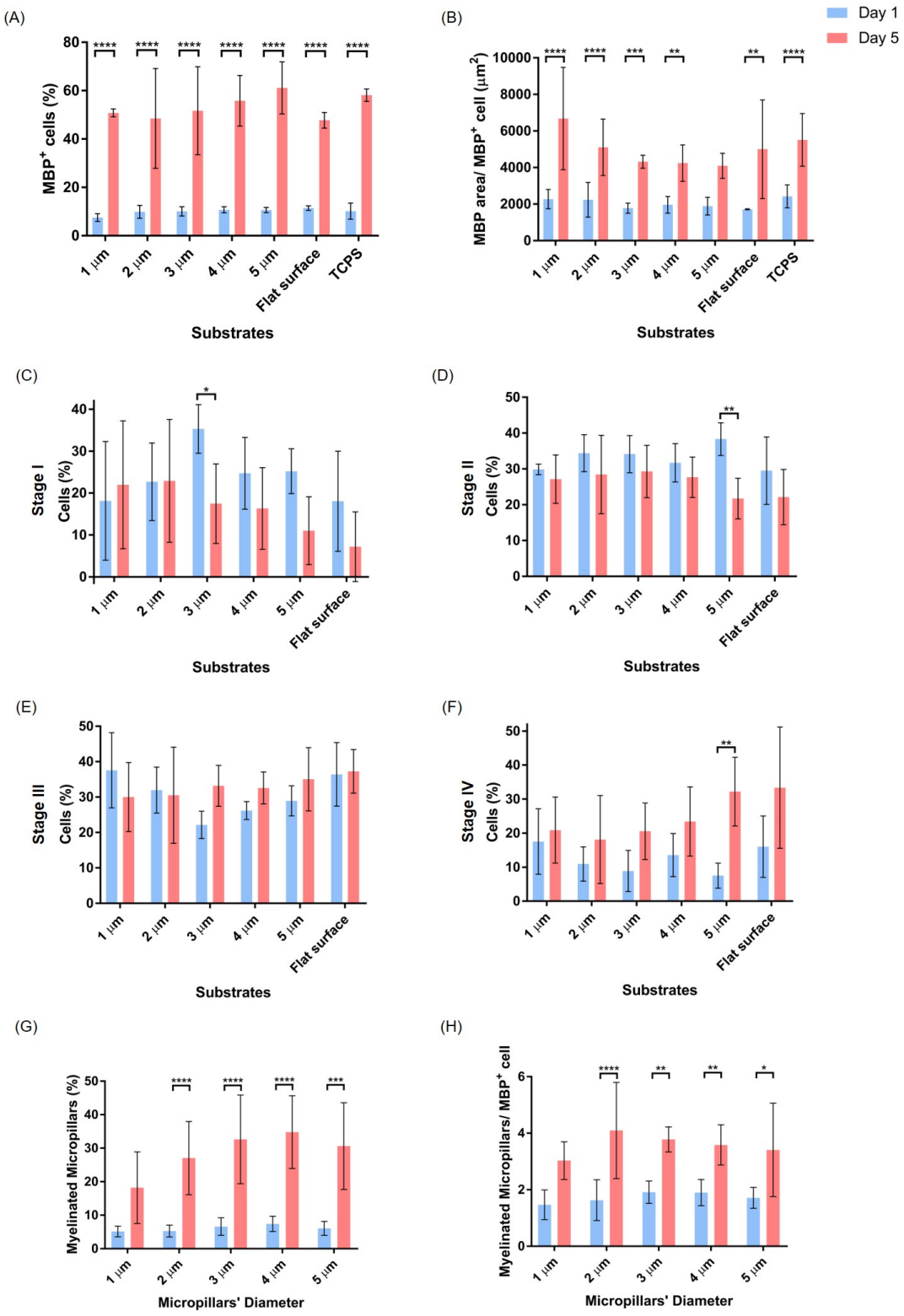


FIGURE G.1: Quantification of differentiation and micropillars' wrapping in OPC cultures on control PDMS platforms at diff. days 1 and 5. (A) Percentage of MBP$^+$ cells (calculated from Olig2$^+$ cells); (B) MBP area per MBP$^+$ cell (μm^2); (C-F) Percentage of cells at differentiation stages I-IV, respectively (calculated from Olig2$^+$ cells); (G) Percentage of myelinated micropillars; (H) Number of myelinated micropillars per MBP$^+$ cell. For all graphs, blue bars refer to day 1 and red bars refer to day 5. n=2 independent experiments, 2-4 technical replicates per diameter. Graphs present mean values with SD bars. Statistical analysis performed using Two-way ANOVA, * $p<0.05$, ** $p<0.01$, *** $p<0.001$, **** $p<0.0001$.

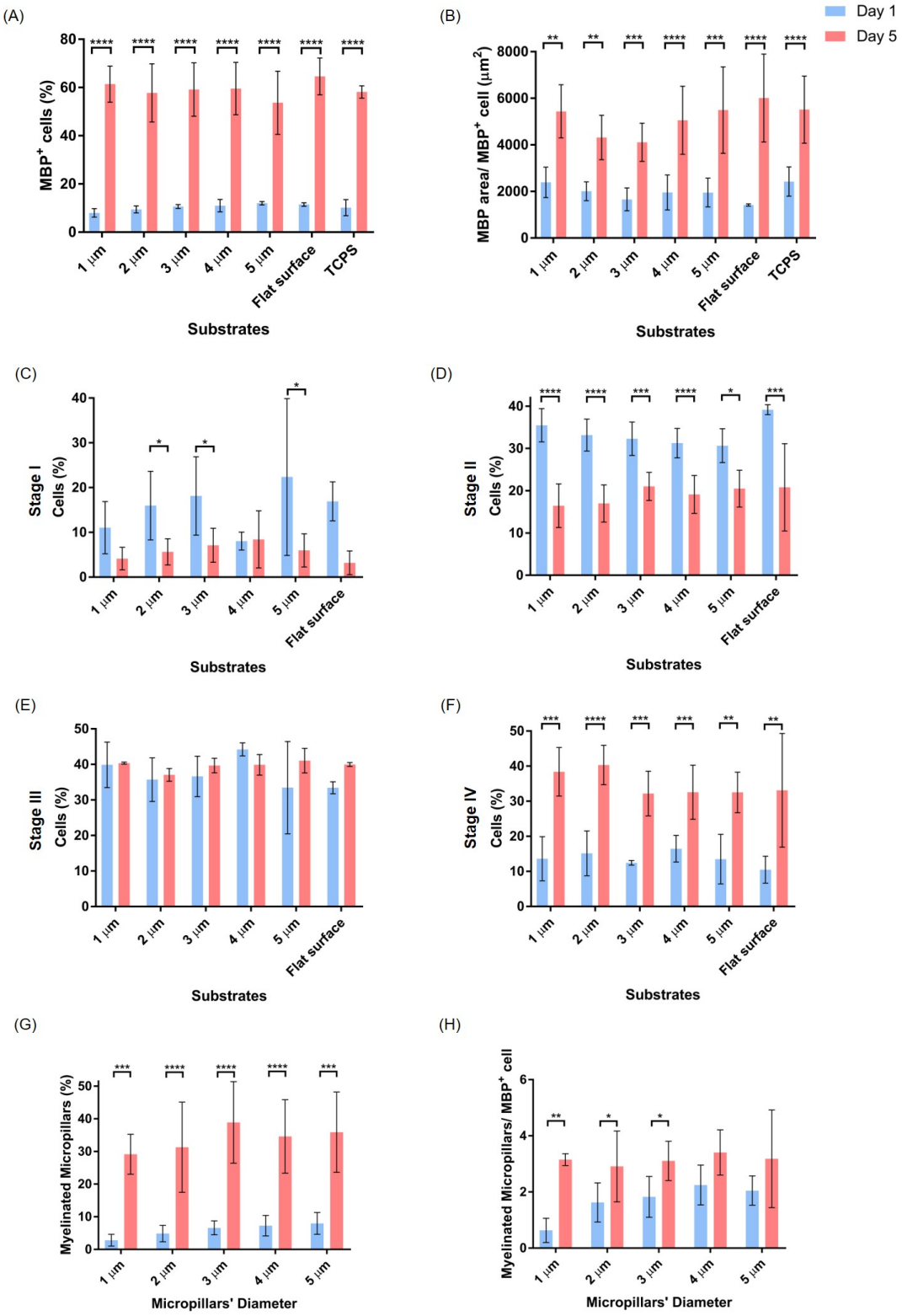


FIGURE G.2: Quantification of differentiation and micropillars' wrapping in OPC cultures on soft PDMS platforms at diff. days 1 and 5. (A) Percentage of MBP^+ cells (calculated from $Olig2^+$ cells); (B) MBP area per MBP^+ cell (μm^2); (C-F) Percentage of cells at differentiation stages I-IV, respectively (calculated from $Olig2^+$ cells); (G) Percentage of myelinated micropillars; (H) Number of myelinated micropillars per MBP^+ cell. For all graphs, blue bars refer to day 1 and red bars refer to day 5. n=2 independent experiments, 2-4 technical replicates per diameter. Graphs present mean values with SD bars. Statistical analysis performed using Two-way ANOVA, * $p<0.05$, ** $p<0.01$, *** $p<0.001$, **** $p<0.0001$